SPECTROSCOPIC INVESTIGATION OF THE QUANTUM DYNAMICS OF SMALL MOLECULES ENCAPSULATED INSIDE FULLERENE CAGES

KELVIN GOH, MPhys.

Thesis submitted to the University of Nottingham for the degree of Doctor of Philosophy

JULY 2015

Abstract

The encapsulation of a small molecule inside a fullerene cage through advances in synthetic chemistry have created a new platform to study the dynamics of a freely rotating and translating quantum rotors entrapped inside a symmetric cage potential. These endohedral fullerene complexes are of great interest because the fullerene cages are able to uniquely provide the entrapped molecules a high level of isolation, homogeneity, symmetry and stability. The endohedral fullerene complexes discussed in this thesis are the $H_2@C_{60}$, $H_2@C_{70}$ and $H_2O@C_{60}$.

Both variants of small molecules studied in this thesis, H_2 and H_2O, possess two strongly coupled protons. This would result in spin isomerism where the spins of both protons in the molecule are able to combine either symmetrically with total spin $I = 1$ (ortho) or anti-symmetrically with total spin $I = 0$ (para). This property has significant consequences for the quantum dynamics of the entrapped molecules. Due to the Pauli Exclusion principle, ortho states can only have odd rotational quantum number, while para states can only have even rotational quantum numbers.

This thesis features the inelastic neutron scattering (INS) study of the three aforementioned endohedral fullerenes and the nuclear magnetic resonance (NMR) study of the $H_2O@C_{60}$. INS spectroscopy probes the lower energy states of the sample to study the quantum dynamics of the molecules, while NMR probes the spin dynamics of the protons to study the magnetic interactions of the proton with its environment.

The $H_2@C_{60}$ is the union between the simplest molecule and the most symmetrical molecule in the universe. It is the first variant of small molecule endohedral fullerenes to be synthesised and is the most well studied of the three variants. This thesis discusses the temperature dependence of cold neutron scattering study in this complex to investigate the statistical distribution of the energy states. The $H_2@C_{70}$ is a less symmetric endohedral fullerene which has a prolate ellipsoidal symmetry cage. This thesis discusses the low temperature thermal neutron scattering and the temperature dependence of cold neutron scattering investigations in the complex

to study the effect of the ellipsoidal cage on the quantum dynamics of the molecules.

$H_2O@C_{60}$ is different to the dihydrogen variant of the small molecule endohedral fullerenes because H_2O possess a permanent electric dipole moment and is less symmetric than H_2. The $H_2O@C_{60}$ is predicted by theory to exhibit ferroelectricity at low temperatures. The ferroelectric alignment of the electric dipole moments of H_2O at low temperature is investigated using both INS and NMR. The quantum dynamics of the $H_2O@C_{60}$ is investigated with low temperature thermal neutron scattering and temperature dependence cold neutron scattering, while the spin dynamics of $H_2O@C_{60}$ is investigated with milli-Kelvin NMR. Furthermore, the $H_2O@C_{60}$ exhibits slow nuclear spin-isomer conversion at low temperatures unlike the $H_2@C_{60}$. This low temperature ortho-H_2O to para-H_2O conversion process is investigated with both INS and NMR to study the conversion mechanism.

Acknowledgements

Time flies and it has been 3 years since I have started my Ph.D. programme. My journey to the completion of my Ph.D. has been immensely valuable and enjoyable, it is a journey which I will never regret taking upon. This journey has not always been smooth sailing. Without the help of those around me, it would not have been possible for me to complete my Ph.D.. Hence, I would like to take this opportunity to acknowledge those who have help me with the completion of my Ph.D. and have made my Ph.D. experience invaluable and enjoyable.

I would first like to thank my supervisor Anthony J. Horsewill for giving me the opportunity to study and work on these wonderful small molecule endohedral fullerene complexes. It has been a pleasure working with him and being under his tutelage. I have learned many invaluable knowledge from him over the course of my Ph.D., from quantum theory to neutron and NMR spectroscopic techniques. I am immensely grateful to him for being such an attentive and understanding supervisor who cares deeply about the progress of my Ph.D.. Without him, I would not have completed my thesis a year ahead of the scheduled end of my funding. I would also like to thank David Peat and my second supervisor John Owers-Bradley for helping me with the running of my experiments on the dilution refrigerator.

The completion of my thesis would not be possible without the close collaboration with Malcolm H. Levitt's group at the University of Southampton. Therefore, I would like to thank Malcolm and Salvatore Mamone for the discussions, exchange of ideas and providing guidance on the study of endohedral fullerene complexes. I am also grateful to Malcolm for giving me the opportunity to visit and perform joint NMR experiments in his lab at the University of Southampton. I would like to give my special thanks to Salvatore for preparing the samples, share many of his experimental results with me and the wonderful hospitality he gave me in Southampton. I would also like to thank Richard Whitby's group at the University of Southampton, Nicholas Turro's group at Columbia University and Yasujiro Murata's group at Kyoto University for synthesising the small molecule endohedral

fullerene samples for my research.

I am also grateful to the Institut Laue-Langevin for the funding, support and the opportunity to perform neutron scattering experiments in Grenoble. I would like to thank Stéphane Rols, Jacques Ollivier and Mark Johnson at the ILL for helping with the running of the neutron experiments. Special thanks to Stéphane for the hospitality in Grenoble and for helping me with the analysis of the neutron scattering data.

I am also immensely grateful to my sponsor iMR CDT, as well as the academics in the CDT programme for providing me with the generous funding and support to make the completion of my Ph.D. possible. I would also like to thank Yasmin Kosar for the organisation of the CDT programs and for making the CDT courses enjoyable.

Special thanks to David Peat, Bo Zhang and Bryn Howells for the great company throughout my time in Nottingham. It has been a pleasure to have you three as friends and colleagues, and I hope we can continue to keep in touch in the future.

Finally, I would like to thank my parents and brothers for the moral support and encouragement to complete my Ph.D.. Lastly, I would like to dedicated this work to those who have been a special part of my life.

Kelvin Goh,
November 2014,
Nottingham

Contents

List of Figures

List of Tables

Part I

Introduction and spectroscopies

Chapter 1

Introduction

1.1 Small molecule endohedral fullerenes

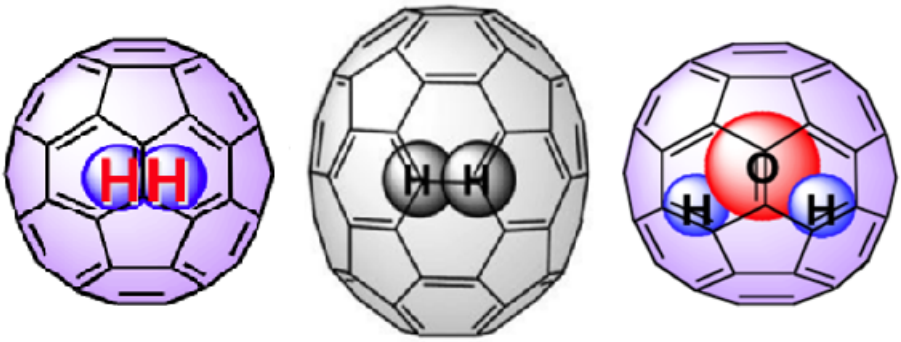

Figure 1.1.1: Variants of small molecule endohedral fullerenes: (from left to right) $H_2@C_{60}$, $H_2@C_{70}$ and $H_2O@C_{60}$.

The supramolecular complex of a small molecule encapsulated inside a fullerene cage (small molecule endohedral fullerenes) has provided an almost unique platform to study many important and fundamental quantum mechanical issues. This study is made possible after advancement in synthetic chemistry by Komatsu et al to encapsulate a hydrogen molecule inside a C_{60} cage ($H_2@C_{60}$) in large quantities via the "molecular surgery" technique [1, 2, 3]. The synthesis of small molecule endohedral fullerene was later extended to other variants such as a H_2 trapped in the rugby-ball shaped C_{70} cage ($H_2@C_{70}$) and a water molecule trapped in a C_{60} cage ($H_2O@C_{60}$) using the "molecular surgery" technique [4, 5, 6].

The entrapped molecule inside a fullerene cage does not form chemical bonding with the carbon atoms of the cage. The carbon atoms instead act as a spring force recalling the entrapped molecule to the centre of the cage, thus allowing it to translate and rotate freely within the cage

[7]. Furthermore, the entrapped molecule's confinement in the fullerene cage almost uniquely enables it to be studied in isolation, which results in minimal interactions with molecules outside the cage. This enables the study of small molecules in environments that cannot be achieved under normal circumstances.

The entrapped molecules of the three aforementioned endohedral fullerenes (H_2 and H_2O) are quantum rotors which have two strongly coupled protons. Therefore, these molecules exhibit nuclear spin isomerism with two distinct spin combinations, the symmetric and anti-symmetric nuclear spin combinations. Molecules with symmetric nuclear spin combinations are known as the ortho species, while molecules with anti-symmetric nuclear spin combinations are known as the para species. This has profound impact on the quantum dynamics of both ortho and para spin species. According to the Pauli Exclusion principle, ortho molecules can only have odd rotational quantum numbers, while para molecules can only have even rotational quantum numbers.

As the H_2O molecule possess a permanent electric dipole moment, there are strong interactions between each entrapped H_2O molecule in the $H_2O@C_{60}$ sample. This leads to many intriguing questions regarding the $H_2O@C_{60}$, such as: Do the electric dipole moments line up to form ferroelectricity? Does the electric dipole moment of an entrapped H_2O induces an electric dipole moment on its C_{60} cage? How does the couplings with neighbouring electric dipole moments affect the quantum dynamics of an entrapped H_2O? Furthermore, unlike the $H_2@C_{60}$ and $H_2@C_{70}$ samples, the $H_2O@C_{60}$ sample exhibits nuclear spin-isomer conversion at cryogenic temperatures in the absence of catalysts, where the meta stable ortho-H_2O converts to para-H_2O.

The investigation of the quantum dynamics of $H_2@C_{60}$, $H_2@C_{70}$ and $H_2O@C_{60}$ are discussed in this thesis.

1.2 Properties and structure of fullerene cages

1.2.1 C_{60}

The C_{60} fullerene is a highly symmetric molecule that contains 60 carbon atoms arranged in a truncated icosahedron structure. This structure contains 12 pentagonal faces and 20 hexagonal faces, with each pentagon sur-

rounded by 5 hexagons and each hexagon surrounded by alternating three pentagons and three hexagons [8, 9]. There are three types of rotational symmetry axes in the C_{60}: 6 C_5 symmetry axes connecting the centre of two opposing pentagonal faces, 10 C_3 symmetry axes connecting the centre of two opposing hexagonal faces and 15 C_2 symmetry axes connecting two opposing hexagon edges (see Figure 1.2.1). There is a total of 120 rotational symmetry operations with respect to the geometric centre of the C_{60} fullerene, thus making it the closest realisation of a spherical molecule with a symmetry point group of I_h. The diameter of the C_{60} fullerene is 7.1 Å, while the distance between two carbon atoms are 1.46 Å for the single bonds and the 1.40 Å for doublet bonds [8].

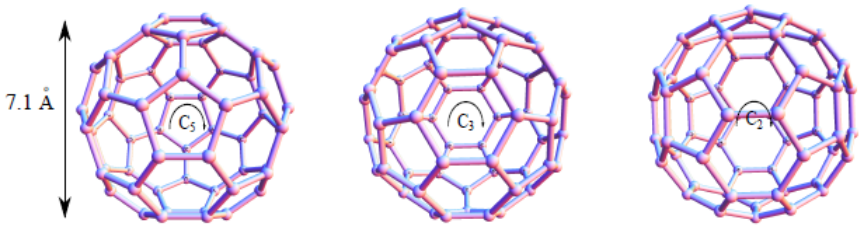

Figure 1.2.1: Illustration of the three symmetry axes of C_{60} fullerenes: (from left to right) C_5, C_3 and C_2 symmetry axes [9].

At normal pressure, the C_{60} molecules form a solid with a face centred cubic (FCC) lattice configuration that has a lattice constant of 14.17 Å and a nearest neighbour centre-to-centre distance of 10 Å [9, 10]. At $T >$ 260 K, the C_{60} lattice experiences molecular reorientation with the C_{60} molecules rotating freely about their positions while the lattice arrangement remains the same [10, 11, 12]. At $T <$ 260 K, the C_{60} molecules experience orientational order where the opposite faces orient in the same direction, forming a simple cubic lattice $Pa\bar{3}$ with four non equivalent C_{60} per unit cell [9, 12, 13]. At $T \lesssim 100$ K, the rotation of the C_{60} molecules freezes on the NMR timescale [14].

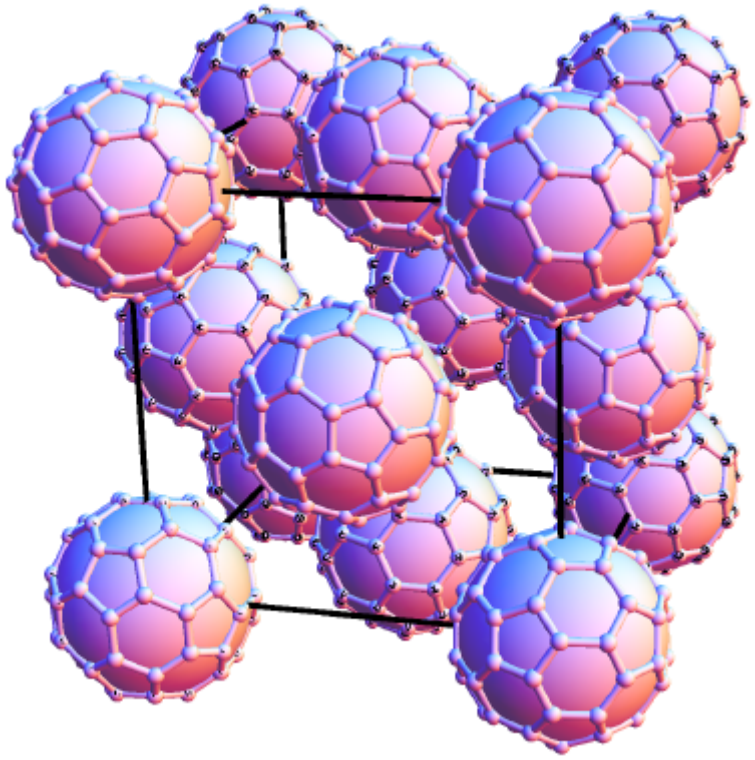

Figure 1.2.2: The face centred cubic lattice configuration of C_{60} molecules.

1.2.2 C_{70}

The C_{70} is an ellipsoidal fullerene that resembles an elongated C_{60} fullerene along the C_5 symmetry axis (see Figure 1.2.3). The C_{70} contains 12 pentagonal faces and 25 hexagonal faces. The C_{70} has a symmetry point group of D_{5h} and is less symmetric than the C_{60}. The length of the bonds between the carbon atoms of the C_{70} are identical to those of the C_{60}.

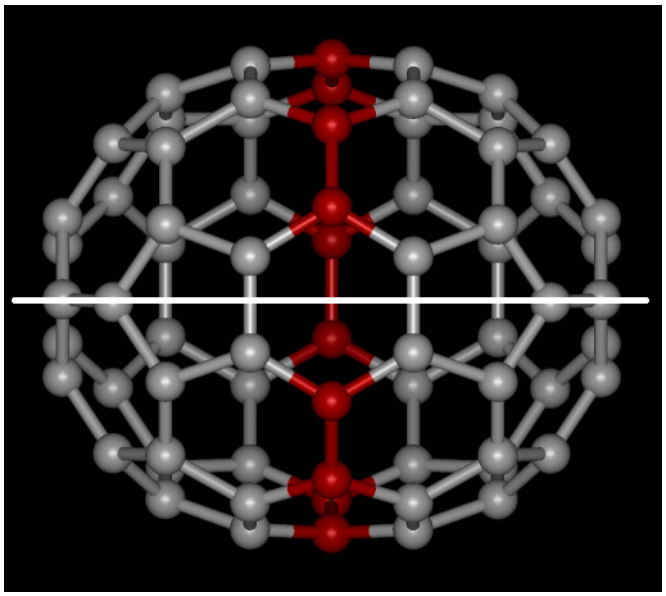

Figure 1.2.3: The structure of the C_{70} fullerene. The highlighted red atoms are the 10 carbon atoms which are in addition to the C_{60} fullerene. These additional carbon atoms partly form the additional 5 hexagonal faces located along the equatorial belt of C_{70} [15]. The white line symbolises the C_5 symmetry axis.

The C_{70} molecule is ellipsoidal unlike the C_{60}, hence there is an additional degree of freedom in its solid packing. Studies have shown that the lattice configuration and orientational ordering of C_{70} varies with temperature [16, 17, 18, 19, 20, 21]. It is shown that the lowest energy lattice configuration is the solid packing of the C_{70} in a FCC-like monoclinic lattice configuration with the long axis (C_5) of the C_{70} aligned along the c-axis (see Figure 1.2.4) [20, 21]. The C_{70} solid transforms into this monoclinic lattice configuration at $T < 275$ K [19, 20, 21]. The monoclinic lattice parameters are measured to be: $a = 10.04$ Å, $b = 9.90$ Å, $c = 27.77$ Å and $\gamma = 120°$ [19]. Furthermore, it is experimentally shown that the solid-packed C_{70} molecules gradually align towards any applied magnetic field with lowering of the temperature [74].

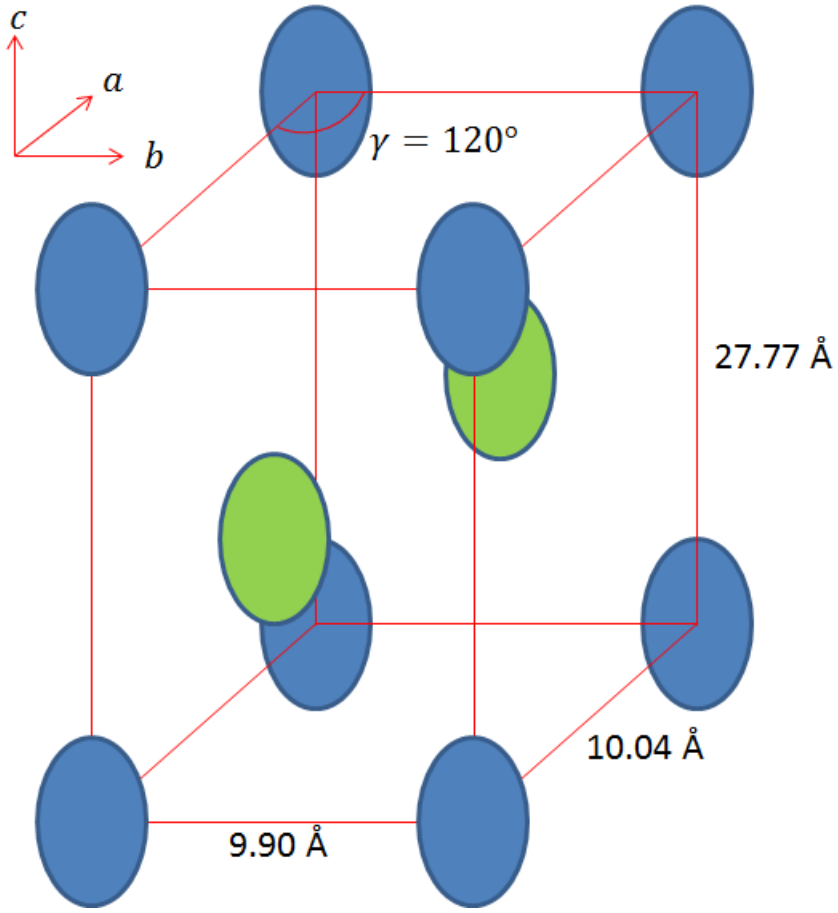

Figure 1.2.4: Schematic of the FCC-like monoclinic lattice configuration of the C_{70} solid at $T < 275$ K. The C_{70} molecules shown in green are molecules that are located at the centre of the two bc-planes of the unit cell. The lattice parameters are measured to be: $a = 10.04$ Å, $b = 9.90$ Å, $c = 27.77$ Å and $\gamma = 120°$ [19].

1.3 Synthesis of small molecule endohedral fullerenes

The first endohedral fullerene complexes were the metallo-endohedral fullerenes, which were synthesised via condensation of the carbon vapour doped with the respective metal [22, 23, 24]. This has since led to the synthesis of other endohedral fullerene complexes that contain reactive materials such as nitrogen atoms and trimetalnitride complexes [25, 26, 31]. The successful synthesis of these materials has allowed the direct study and application of these reactive materials which otherwise cannot be done under normal circumstances [27, 28, 29, 30, 31]. However, such methods of synthesis result in only a small fraction of the fullerene cages being filled.

A new method of synthesis known as the "molecular surgery" was developed by Komatsu et al to encapsulate a hydrogen molecule inside a C_{60} fullerene [1, 2, 3]. The "molecular surgery" technique is a multi-step procedure that involves: (1) Creating an orifice on the C_{60} cage using three step organic reaction to form the azacyclic-thiacyclic-open-cage-fullerene (ATOCF). (2) Applying high temperature and high pressure to insert the hydrogen molecule through the orifice [32]. (3) Closing the orifice using a four step organic reaction while the hydrogen remains inside the C_{60}. The schematic of the molecular surgery procedure used for the production of $H_2@C_{60}$ is illustrated in Figure 1.3.1 [9]. High performance liquid chromatography is subsequently used to remove all the residual empty C_{60} cages from the endohedral fullerenes [1, 2]. The sample is also rigorously sublimed to have the other impurities within the sample removed to ensure that only $H_2@C_{60}$ remained in the sample. The resulting endohedral fullerene sample has a high level of purity and are in the form of a black powder. This technique enables large amount of endohedral fullerenes to be synthesised for various spectroscopic investigations such as infrared (IR), nuclear magnetic resonance (NMR) and inelastic neutron scattering (INS).

Similar "molecular surgery" techniques were also used to insert up to two H_2 molecule inside a C_{70} fullerene and one H_2O molecule inside a C_{60} fullerene. The $H_2@C_{60}$ and $H_2@C_{70}$ samples studied in this thesis are synthesised by Komatsu et al at Kyoto University (Japan) and Turro et al at Columbia University (USA), whereas the $H_2O@C_{60}$ samples are synthesised by Murata et al at Kyoto University, Turro et al and Whitby et al at the University of Southampton (UK).

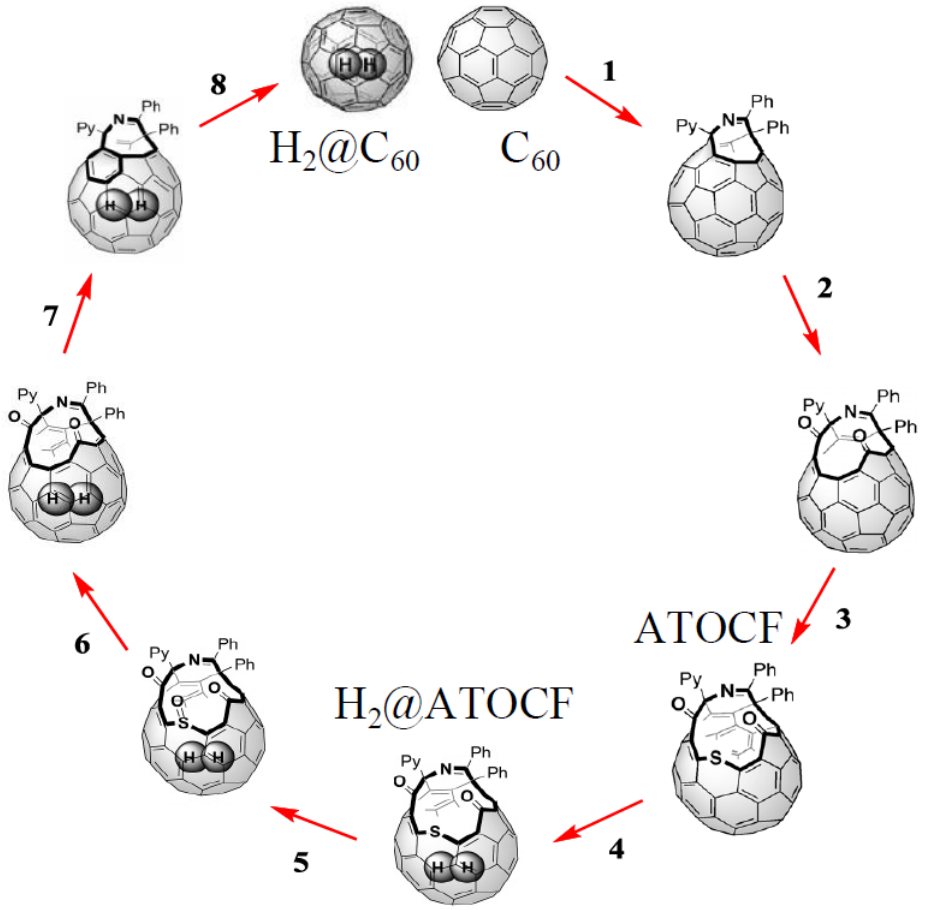

Figure 1.3.1: Molecular surgery multi-step procedure to synthesise the $H_2@C_{60}$. An orifice is created on the C_{60} cage to form the azacyclic-thiacyclic-open-cage-fullerene (ATOCF) before inserting the H_2 molecule through the orifice. This is then followed up with the closing of the orifice while the H_2 molecule is in the C_{60} cage to form the $H_2@C_{60}$ [9].

Chapter 2

Spectroscopic techniques

2.1 Inelastic neutron scattering (INS)

Inelastic neutron scattering is a spectroscopic technique that is commonly used in condensed matter research to investigate atomic and molecular motion as well as magnetic and crystal field excitations. This technique is particularly useful in the study of hydrogen based molecules as the incoherent scattering cross sections of protons is much larger than those of other nuclei [33] (see Figure 2.1), therefore the INS signal from the protons are usually much larger than those of other nuclei in the sample. This technique has also proven to be invaluable in the investigation of hydrogen based small molecule endohedral fullerenes where the strongly coupled pair of protons are indistinguishable quantum particles [55, 34]. Furthermore, INS has the ability to excite or de-excite a pair of proton to a different spin species, whereas other spectroscopic techniques such as infrared could not [34].

The INS spectra discussed in the thesis are recorded with one of the following INS spectrometers: IN4C, IN5, IN1-Lagrange and TOFTOF.

Nucleus	$\sigma_{coherent}$ ($10^{-24}cm^2$)	$\sigma_{incoherent}$ ($10^{-24}cm^2$)
^{1}H	1.8	80.2
^{2}H	5.6	2
^{12}C	5.6	0
^{16}O	4.2	0

Table 2.1: The neutron scattering cross sections of various nuclei [33].

2.1.1 Theory

The mechanics of neutron scattering is described using quantum scattering process. The state of the scattering system is represented by the differential cross-section $\frac{d^2\sigma}{d\Omega dE_f}$, which describes the number of neutron scattered per second into a solid angle $d\Omega$ with final energy between E_f and $E_f + dE_f$. The differential cross-section of a pair of strongly coupled protons can be expressed as:

$$(\frac{d^2\sigma}{d\Omega d\omega}) = \frac{k_f}{k_i}\sum_{i,f} n_i| < i|V|f > |^2\delta(\hbar\omega - E_i + E_f), \tag{2.1.1}$$

where k_i and k_f are the respective initial and final wavenumber of the neutron; n_i is the statistical weight of the initial state; $\hbar\omega$ is the difference in energy between the final and initial state of the nuclei; E_i and E_f are the respective initial and scattered neutron energies; $| < i|V|f > |^2$ is the matrix element, where

$$V = \sum_{\alpha=1,2} e^{i\kappa R_\alpha} b_{coh} + \frac{b_{incoh}}{2}\sigma . I_\alpha, \tag{2.1.2}$$

while b_{coh} and b_{incoh} are the coherent and incoherent scattering lengths of the nucleus; $\kappa = k_i - k_f$ is the momentum transfer, where k_i and k_f are the respective initial and scattered neutron wavenumbers; σ is the neutron spin; I_α and R_α are the respective spin and the position vector of the nucleus α; $R_\alpha = R_0 + ((-1)^\alpha\rho)/2$. R_0 is the vector defining the centre of mass of the molecule and ρ is the vector connecting the two nuclei. The initial state ($< i|$) is the product of the conjugated initial neutron spin wavefunction ($< \sigma_i|$) and the conjugated initial molecular wavefunction ($< \psi_i|$) , while the final state ($|f >$) is the product of $|\sigma_f >$ and $|\psi_f >$[34].

The sum of Equation 2.1.2 can then be expanded through the following steps:

$$
\begin{aligned}
V &= \sum_{\alpha=1,2} e^{i\kappa R_\alpha} b_{coh} + \frac{b_{incoh}}{2}\sigma_{\blacksquare} I_\alpha \\
&= \sum_{\alpha=1,2} e^{i\kappa(R_0+((-1)^\alpha\rho)/2)} b_{coh} + \frac{b_{incoh}}{2}\sigma_{\blacksquare} I_\alpha \\
&= e^{i\kappa(R_0-\rho/2)} b_{coh} + \frac{b_{incoh}}{2}\sigma_{\blacksquare} I_1 + e^{i\kappa(R_0+\rho/2)} b_{coh} + \frac{b_{incoh}}{2}\sigma_{\blacksquare} I_2 \\
&= e^{i\kappa R_0}[b_{coh}(e^{-i\kappa\cdot\rho/2} + e^{i\kappa\cdot\rho/2}) + \frac{b_{incoh}}{2}(e^{-i\kappa\cdot\rho/2}\sigma_{\blacksquare} I_1 + e^{i\kappa\cdot\rho/2}\sigma_{\blacksquare} I_2)] \\
&= e^{i\kappa R_0}[b_{coh}(2\cos(\kappa\cdot\rho/2)) + \frac{b_{incoh}}{2}(\{\cos(\kappa\cdot\rho/2) - i\sin(\kappa\cdot\rho/2)\}\sigma_{\blacksquare} I_1 \\
&\quad +\{\cos(\kappa\cdot\rho/2) + i\sin(\kappa\cdot\rho/2)\}\sigma_{\blacksquare} I_2)] \\
&= e^{i\kappa R_0}[b_{coh}(2\cos(\kappa\cdot\rho/2)) + \frac{b_{incoh}}{2}(\cos(\kappa\cdot\rho/2)\sigma_{\blacksquare}(I_1 + I_2) \\
&\quad +i\sin(\kappa\cdot\rho/2)\sigma_{\blacksquare}(I_1 - I_2))] \\
&= e^{i\kappa R_0}[2b_{coh}\cos(\frac{1}{2}\kappa\cdot\rho) + \frac{b_{incoh}}{2}\cos(\frac{1}{2}\kappa\cdot\rho)\sigma\cdot(I_1 + I_2) \\
&\quad +i\frac{b_{incoh}}{2}\sin(\frac{1}{2}\kappa\cdot\rho)\sigma\cdot(I_1 - I_2)]. \qquad (2.1.3)
\end{aligned}
$$

The real terms with cosine function in Equation 2.1.3 represents pure translational transition (ortho to ortho/para to para transition), while the sine function in the third term represents transitions that involve simultaneous rotational and translational transitions, which allows for interchange between ortho species and para species. It can be seen from the $(I_1 + I_2)$ part of the second term that only ortho species will give a non-zero term, whereas para species will result in the term being zero. Only the first term provides para species a possibility to undergo pure translational transition. However, as the b_{incoh} of a proton is much larger than their b_{coh}, pure translational transitions of para species are virtually absent in INS. Therefore, it can be concluded from Equation 2.1.3 that ortho species can undergo pure translational transitions as well as simultaneous rotational and translational transitions (inducing ortho-para conversion), whereas para species can only undergo simultaneous rotational and translational transitions [34].

The scattering law of a transition can be derived from Equation 2.1.1 and 2.1.2 by approximating the molecular wavefunction as a product of pure rotational and translational eigenfunctions, while the translational-rotational coupling is negligible [34, 35]. For example, the scattering law of the pure rotational transition from the ground state of para-H_2 to ground state of ortho-H_2 is written as

$$S(\kappa,\omega)^{p\to o}_{000\to 100} \propto \frac{k_f}{k_i} b^2_{incoh} p_{000} e^{-\frac{1}{3}\kappa^2 <u^2>} [j_1(\kappa r_{HH})]^2 \times \delta(\hbar\omega - E_{000} + E_{100}) \tag{2.1.4}$$

where $j_n(\kappa r_{HH})$ is the spherical Bessel function of order n; r_{HH} is the distance between the centre of mass of the molecule and the nuclei; $-\frac{1}{3}\kappa^2 < u^2 >$ is the Debye-Waller factor and $< u^2 >$ is the mean squared displacement of the hydrogen molecule [34].

In addition to the energy transfer spectra, the momentum transfer spectrum $S(\kappa)$ can also be analysed to obtain information on the spatial confinement and the physical dimension of the scattering object. The momentum transfer is defined as $\hbar\kappa$. The analysis of the momentum transfer spectrum of endohedral fullerenes will not be discussed in this thesis because it is done by my supervisor, Anthony J. Horsewill. All of the INS energy transfer spectra in this thesis are summed over all the scattering angles or momentum transfer spectra. Nevertheless, the momentum transfer spectrum can be shown to have the following relation [35, 36]:

$$S(\kappa) \propto exp(-\frac{1}{3}\kappa^2 < u^2 >) \sigma_{inc} [j_1(\kappa d_{HH}/2)]^2 \tag{2.1.5}$$

where $-\frac{1}{3}\kappa^2 < u^2 >$ is the Debye-Waller factor, $< u^2 >$ is the mean-squared displacement of H_2, σ_{inc} is the incoherent neutron scattering cross section and $j_1(\kappa d_{HH}/2)$ is the nth order spherical Bessel function [43]. The Debye-Waller factor is temperature dependent. Hence, it has to be considered in our temperature dependence INS analysis. This factor can be removed by normalising the spectral amplitudes with the elastic peak.

2.1.2 INS spectra

The INS spectra is normally plotted with the energy transfer value along the horizontal axis and the signal intensity along the vertical axis. An example of an INS spectra is shown in Figure 2.1.1. The figure shows the INS spectra of the $H_2@C_{60}$ sample recorded at 1.6 K using incident neutron wavelength λ_n =1.2 Å with the IN4C spectrometer. The energy transfer region of $\Delta E > 0$ is known as the neutron energy (NE) loss region, while energy transfer region of $\Delta E < 0$ is known as the NE gain region. Peaks in the NE loss region corresponds to upward transitions, where neutrons transfer ΔE energy to the scatterers to excite the scatterers to their respective higher energy state. Conversely the peaks in the NE gain region corresponds to downward transitions, where the neutrons absorb ΔE energy from the scatterers to de-excite the scatterers to their respective lower energy state. The intense peak centred at 0 meV is the elastic peak which corresponds to the elastic transitions, where there is no transfer of energy between the neutrons and the scatterers.

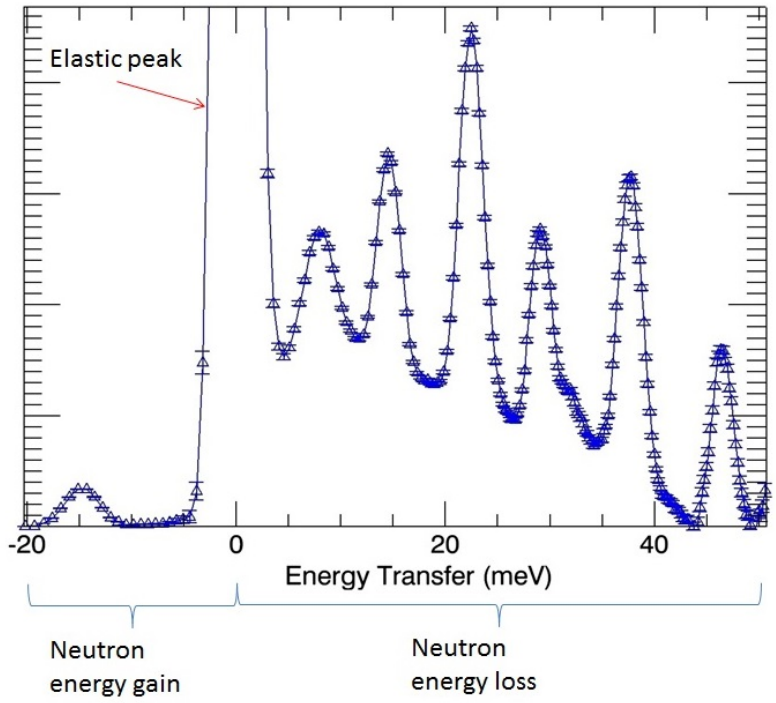

Figure 2.1.1: An example of an INS spectra. The spectra shown shown in this figure is the spectra of the $H_2@C_{60}$ sample recorded at 1.6 K using incident neutron wavelength λ_n =1.2 Å with the IN4C spectrometer.

2.1.3 IN4C

The IN4C is a time-of-flight INS spectrometer located at the Institut Laue-Langevin (ILL) in Grenoble, France. The IN4C operates on the high flux thermal neutron beam line to obtain medium resolution spectra [37]. The schematic of the IN4C spectrometer is shown Figure 2.1.2. The Fermi chopper converts the neutron beam into neutron pulses, which then pass through the monochromater to filter the unwanted neutrons to ensure that only neutrons with a specific wavelength are Bragg reflected to the sample. The time in which the Bragg reflected neutron pulse enters the flight chamber is recorded before being scattered by the sample onto the ^{3}He detectors that are situated across the 2 m flight chamber. The energy of the scattered neutron is determined from the time-of-flight of the neutron.

The IN4C is optimised for the INS study of the energy transfer range between (0-30 meV). However, NE gain peaks are still observable in the IN4C spectra albeit a lower signal-to-noise ratio.

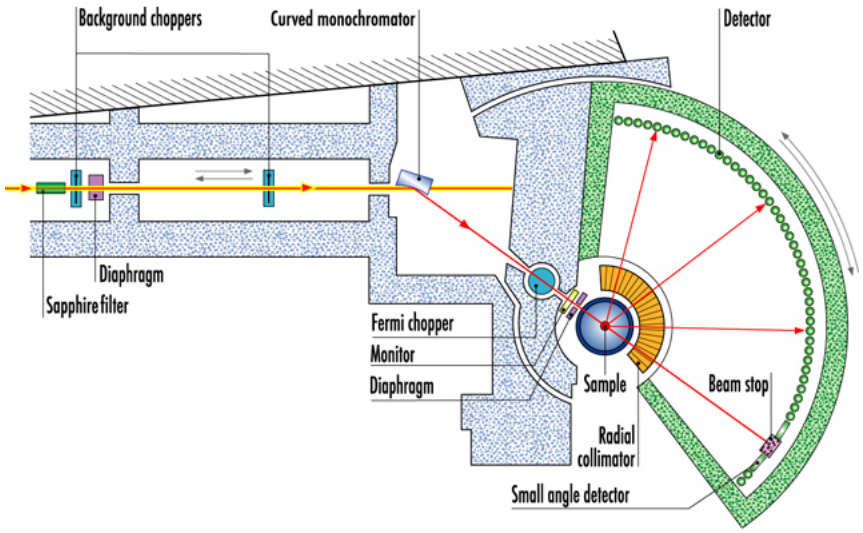

Figure 2.1.2: The schematic of the IN4C spectrometer [37].

2.1.4 IN5

The IN5 is a disk-chopper time-of-flight INS spectrometer located at the ILL. The IN5 operates on the cold neutron beam line to obtain high resolution spectra [38]. The schematic of the IN5 spectrometer is shown in Figure 2.1.3. The IN5 uses 6 pairs of counter-rotating disk choppers to create neutron pulses with the selected neutron wavelength. The time in which the Bragg reflected neutron pulse enters the flight chamber is recorded before being scattered by the sample onto the ^{3}He detectors that are situated across the 4 m flight chamber. The energy of the scattered neutron is determined from the time-of-flight of the neutron.

Only NE gain transitions can be observed in the IN5 spectra due to the use of low energy incident neutrons which are unable to excite the scatterers to a higher energy state. The schematic of TOFTOF spectrometer is similar to the IN5.

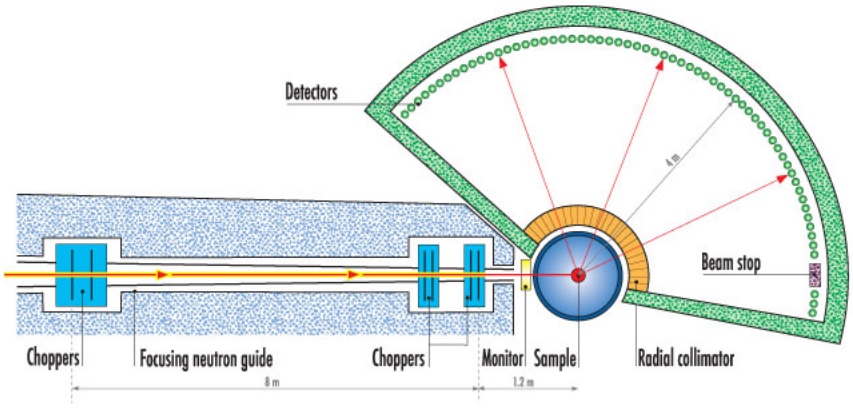

Figure 2.1.3: The schematic of the IN5 spectrometer [38].

2.1.5 IN1-Lagrange

The IN1-Lagrange spectrometer is a INS spectrometer which operates on the "hot source" moderator of the ILL reactor. The IN1-Lagrange is designed to study high energy excitations with high resolution [39]. The schematic of the IN1-Lagrange spectrometer is shown in Figure 2.1.4. The IN1-Lagrange uses a single crystal monochromater of either Si or Cu to select the incident neutron wavelength. The selected incident neutrons are then scattered by the sample onto the pyrolytic graphite analyser crystal which reflects the scattered neutrons onto the detector. The geometry of the graphite crystal is designed such that only neutrons of a fixed energy (4.5 meV) are reflected from the crystal onto the detector. For example, if the incident neutron energy is set to be 30 meV, then the detected neutrons correspond to the energy transfer value of 25.5 meV. The spectra are obtained by rotating the single crystal monochromater to alter the incident neutron energy to sweep across the energy transfer axis. The beryllium crystal is placed between the sample and the graphite crystal to filter out the higher-order harmonics.

The type of monochromater crystal used is dependent on the desired energy transfer value to obtain the optimal resolution. The Si(331) crystal is used to measure the energy transfer values of $12.7 < \Delta E \leq 22.5$ meV, while the Cu(220) crystal is used to measure the energy transfer values of $22.5 < \Delta E \leq 80$ meV. The NE gain transitions cannot be observed with the IN1-Lagrange due to the use of high energy incident neutrons.

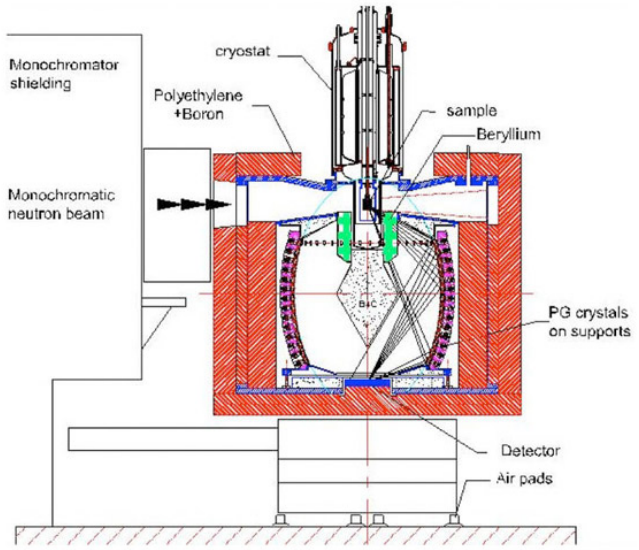

Figure 2.1.4: The schematic of the IN1-Lagrange spectrometer [39].

2.2 Nuclear magnetic resonance (NMR)

2.2.1 Basics of NMR

In NMR, an applied magnetic field (along the z-axis) is applied to align the magnetic moments of the nuclear spin within the sample along the direction of the magnetic field. The magnitude of the magnetisation is dependent on the strength of the applied field and the temperature of the sample, as described by the Curie Law. In the presence of an applied magnetic field, the magnetisation of the sample will precess around the magnetic field. The frequency of this precession is known as the Larmor frequency. The Larmor frequency $\omega = -\gamma \cdot B_0$ is the product between the gyromagnetic ratio γ and the applied magnetic field B_0. A radio frequency (RF) pulse of the same frequency as the Larmor frequency is then applied along the X-axis of the rotating frame by applying a current through the solenoid surrounding the sample, thus inducing a torque on the nuclear spins which rotates the nuclear spins around the X-axis. The radio frequency pulse width and amplitude is set such that it rotates the magnetisation of the sample by an angle of $\frac{\pi}{2}$. The magnetisation of the sample will then precess about the xy-plane and induce an electric current via the solenoid to produce the NMR signal. As the magnetic precession of the sample about the xy-plane is not an equilibrium state, the magnetisation eventually relaxes to its lowest energy state which is in the direction of the magnetic field (T_1 relaxation). The recorded NMR signal will be the strongest right after the $\frac{\pi}{2}$-pulse and decays quickly as a result of the decoherence of the magnetisation along the xy-plane (T_2 relaxation). This decay is also known as the free induction decay (FID). The NMR spectrum can then be extracted from the signal by Fourier transforming the FID.

2.2.2 NMR spin dynamics

NMR spectroscopy is a powerful method of probing the molecular properties of a sample by studying its spin dynamics. In the case of solid-state NMR, the spectrum is very broad because there is no random molecular tumbling to average out effects of the orientation-dependent (anisotropic) interactions. The lineshape of the broad NMR spectrum and the T_1 relaxation rate can be analysed to obtain information regarding the spin and molecular dynamics of a solid-state sample. The lineshape is sensitive to various anisotropic spin interactions such as the dipole-dipole interaction, chemical shift anisotropy (CSA) interaction and the interaction with

the crystal field, while both lineshape and T_1 relaxation are dependent on the molecular dynamics of the molecule [9, 40]. In this thesis, only the $H_2O@C_{60}$ samples are investigated with NMR.

2.2.2.1 Dipole-dipole coupling

The direct dipole-dipole coupling involves the interaction of one nuclear spin with the magnetic field generated by another nuclear spin and vice versa. The nuclear spin dynamics of small molecules containing a pair of strongly coupled protons such as H_2 and H_2O are dominated by the direct dipole-dipole interaction of the proton spins [40]. There are two types of dipole-dipole interactions, the homonuclear and heteronuclear dipole-dipole interaction. For the purpose of this thesis only the homonuclear dipole-dipole interaction will be discussed as only this is relevant to our NMR study of the $H_2O@C_{60}$.

The dipole-dipole coupling Hamiltonian of a pair of protons can be written as

$$\hat{H} = b_{jk}\frac{1}{2}(3\cos^2\theta - 1)(3(\hat{I}_j \cdot e_{jk})(\hat{I}_k \cdot e_{jk}) - \hat{I}_j \cdot \hat{I}_k) \tag{2.2.1}$$

where $b_{jk} = \frac{\mu_0 \gamma 2\hbar}{4\pi r_{jk}^3}$ is the dipolar constant of spins j and k; I_j and I_k are the nuclear spins of j and k protons; e_{jk} is the unit vector of the line connecting the two protons j and k; θ is the angle between the applied magnetic field B_0 and e_{jk} (molecular orientation). As the dipolar interaction tensor is symmetric and traceless, both protons experience the same dipolar interaction.

Solving Equation 2.2.1 then leads to

$$\nu = \nu_0 \pm \frac{3}{4}b_{jk}(3\cos^2\theta - 1) \tag{2.2.2}$$

where ν_0 is the Larmor frequency of the proton, ν is the effective Larmor frequency of the proton as a result of the dipolar interaction and the $\pm$ sign is dependent on the orientation of the nuclear spin. The NMR spectrum of proton pairs with molecular orientations θ =0°, 30°, 53.74°, 60° and 90° respectively are simulated using Equation 2.2.2 by assuming $\nu_0 = 0$ and $\frac{3}{4}b_{jk} = 10$ kHz (see Figure 2.2.1). The line labelled as α corresponds to the total spin $I = 1$, while the line labelled as β corresponds to $I = -1$. It can be seen that the frequency separation between α and β ($\Delta\nu_{\alpha\beta} = \nu_\alpha - \nu_\beta$) is largest when e_{jk} is parallel to B_0, is zero when e_{jk} is at a magic angle with respect to B_0 and has the greatest negative value when e_{jk} is perpendicular

to B_0.

In the case of powder samples, all molecules in a crystallite have the same molecular orientation. As the crystallites are randomly oriented with respect to B_0, powder averaging has to be performed to take into account all possible angles θ. Powder averaging requires appropriate weighting to be applied for each orientation to take into account the fact that there are more ways for a crystallite to orientate at $\theta = 90°$ than at $\theta = 0°$. Performing powder averaging on Equation 2.2.2 results in the powder spectrum shown in Figure 2.2.1. This powder spectrum is also known as the Pake doublet. As the peaks of the doublet correspond to signal from molecules which are oriented at $\theta = 90°$, the calculation for the frequency separation of the peaks are:

$$\begin{aligned}
\Delta\nu_{\alpha\beta} &= (\nu_0 - \frac{3}{4}b_{jk}(3\cos^2(\frac{\pi}{2}) - 1)) - (\nu_0 + \frac{3}{4}b_{jk}(3\cos^2(\frac{\pi}{2}) - 1)) \\
&= \frac{3}{4}b_{jk}(2) \\
&= \frac{3}{2}b_{jk}.
\end{aligned}$$

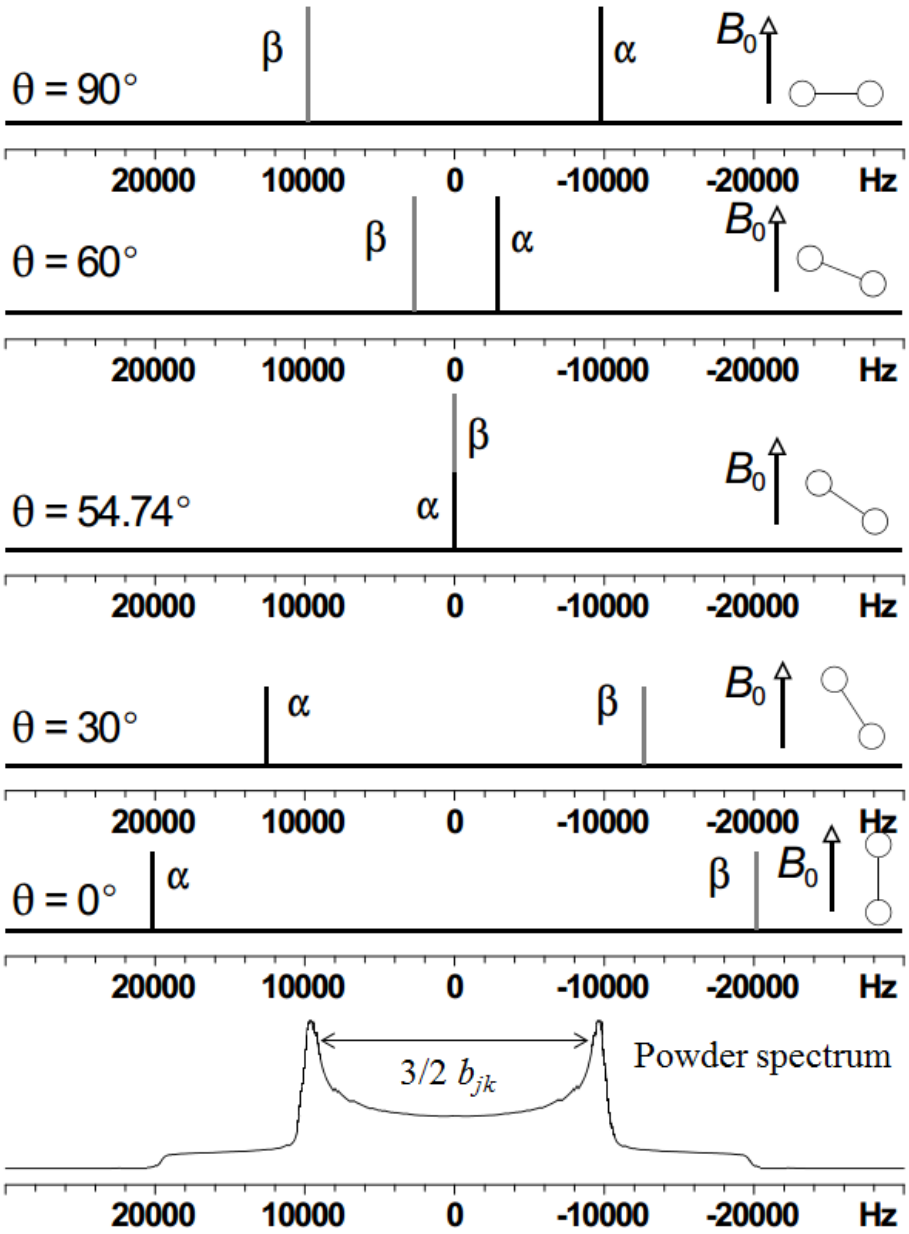

Figure 2.2.1: Simulated NMR spectra of H_2 molecules which are oriented at the respective angle θ shown next to the spectra. The frequency values are calculated using Equation 2.2.2 by assuming $\nu_0 = 0$ and $\frac{3}{4}b_{jk} = 10$ kHz. The line labelled as α corresponds to the total spin $I = 1$, while the line labelled as β corresponds to $I = -1$. The powder spectrum shown at the bottom of the figure is obtained from the powder averaging of all molecular orientations. The pattern of this spectrum is also known as the Pake doublet [41].

2.2.3 NMR instruments

Most of the NMR spectra discussed in the thesis are recorded using the dilution refrigerator with built-in NMR spectrometer at the University of Nottingham. The other NMR spectra discussed in the thesis are recorded using the field-cycling NMR spectrometer at the University of Nottingham and the Bruker AVANCE-II + NMR spectrometer during the joint experiment performed at the University of Southampton.

The dilution refrigerator enables the cooling of the sample to temperatures as low as 2 mK. The dilution refrigerator with built-in NMR spectrometer is a top loading system which cools the sample via a three steps cooling process. The initial cooling of the sample from room temperature is done with the liquid helium bath (4.2 K) before cooling the sample further to 1.5 K using the 1 K pot. The sample is then cooled to milli-Kelvin temperatures using the mixing chamber containing ^{3}He/^{4}He mixture. The superconducting magnet in the dilution refrigerator is a variable field magnet with a maximum field of 15.5 T. The NMR probe has a fixed frequency of 104.5 MHz, therefore the background magnetic field is set to 2.45 T to achieve proton resonance.

The field-cycling NMR spectrometer has an in-built liquid helium cryostat to cool the sample down to 4.2 K. The field-cycling superconducting magnet in the instrument has a maximum field of 2.5 T. The spectra recorded with the field-cycling NMR spectrometer are done using a fix frequency probe of 36.6 MHz. Therefore, the background magnetic field is set to 0.86 T to achieve proton resonance. The NMR experiment performed using the field-cycling NMR spectrometer is done with a fixed background magnetic field of 0.86 T. Hence, the field-cycling ability of the instrument is not utilised. The Bruker AVANCE-II + NMR spectrometer has a fixed background magnetic field of 14.1 T. The NMR probe is mounted to a continuous-flow cryostat to cool the sample with liquid helium [88].

Part II

$H_2@C_{60}$

Chapter 3

Theory and properties of $H_2@C_{60}$

Figure 3.0.1: Schematic of $H_2@C_{60}$ supramolecular complex.

The union of the simplest molecule (H_2) and the most symmetric molecule (C_{60}) has enabled the observation of the most basic quantum mechanical problem, the particle in a box problem, at a molecular level. This is because the entrapped H_2 does not form hydrogen bond with the carbon atoms of the cage. Hence, the H_2 is free to rotate and translate within the nearly spherical cage.

Other similar but less symmetric variants of $H_2@C_{60}$ such as H_2 trapped in ice clathrate [42] and H_2 trapped in open-caged fullerene [43] have been studied with INS. These systems have shown a combination of ortho to para scattering and molecular rattling energy levels which are similar to $H_2@C_{60}$.

The $H_2@C_{60}$ was the first of the small molecule endohedral fullerenes to be successfully synthesised using the "molecular surgery" method (see Section 1.3). Hence, it has been extensively studied over the years since it has been successfully synthesised. The $H_2@C_{60}$ is a very robust molecular complex that shares many similar properties as those of the empty C_{60}

cages. The pure $H_2@C_{60}$ samples are in a form of black powder and are stable up to a temperature of 500 °C under vacuum [3].

Due to the high symmetry of the $H_2@C_{60}$ as well as it being the most well understood small molecule endohedral fullerene, the molecular dynamics of $H_2@C_{60}$ is used as the theoretical framework for the development of other less symmetric small molecule endohedral fullerenes, such as the $H_2@C_{70}$ and $H_2O@C_{60}$.

3.1 Spin isomerism of H_2

The H_2 molecule, which is composed of four fermions (two protons and two electrons), is subjected to the Pauli exclusion principle. Therefore, its total nuclear wavefunction has to be anti-symmetric in the exchange of the two indistinguishable protons. The total nuclear wavefunction is expressed as the product between the spatial-rotational (ψ_{rot}) and nuclear spin wavefunctions ($\psi_{nuclear\,spin}$) (see Figure 3.1.1). There are two ways in which the proton spins can combine, namely the symmetric and antisymmetric combinations. The symmetric spin combination (ortho-H_2) has a total spin of 1, while the antisymmetric spin combination (para-H_2) have a total spin of 0. Therefore, in order to satisfy the Pauli exclusion principle, the para-H_2 have to have a symmetric spatial-rotational wavefunction, while the ortho-H_2 have to have an antisymmetric spatial-rotational wavefunction. Hence, para-H_2 can only have even rotational quantum numbers (J =0, 2, 4, 6,...), while ortho-H_2 can only have odd rotational quantum numbers (J =1, 3, 5, ...).

The rotational energy is expressed as $E = B(J(J+1))$, where $B = \hbar^2/2I_m$ is the rotational constant and I_m is the moment of inertia. The magnitude of the splitting between the ortho-H_2 ground state ($J = 1$) and the para-H_2 ground state ($J = 0$) is determined to be $\Delta E = 2B =$ 14.7 meV, where B is calculated to be 7.37 meV. As the lowest rotational quantum number for ortho-H_2 is $J = 1$, this means that the ortho-H_2 have a finite rotational energy even at the lowest temperature.

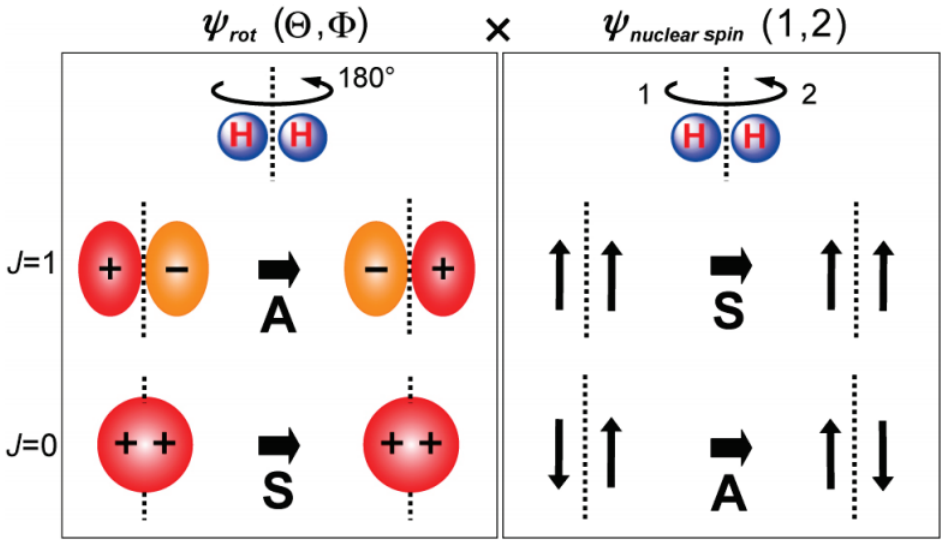

Figure 3.1.1: The total wave-function of H_2, which is the product of the spatial-rotational wavefunction ψ_{rot} and the nuclear spin wavefunction $\psi_{nuclear\ spin}$, has to be antisymmetric as a results of the Pauli exclusion principle. The $\psi_{nuclear\ spin}$ of para-H_2 ($I = 0$) is antisymmetric, therefore, its ψ_{rot} has to be symmetric. Conversely, the $\psi_{nuclear\ spin}$ of ortho-H_2 ($I = 1$) is symmetric, therefore, its ψ_{rot} has to be antisymmetric.

3.2 Molecular dynamics of H_2@C_{60}

The overall dynamics of the H_2 entrapped in the C_{60} cage can be described in terms of 5 quantum numbers ν, J, n, l and λ. ν is the molecular-stretch vibrational quantum number; J is the rotational quantum number; n is the principle quantum number that describes the displacement of the centre of mass of H_2 from the centre of the cage; l is the translational angular momentum quantum number that describes the orbiting of the H_2 molecule about the centre of the cage, where $l = n, n-2, ..., 1$ for odd n and $l = n, n-2, ..., 0$ for even n; and $\lambda = l + J, l + J - 1, ..., |l - J|$ is the translational-rotational (TR) quantum number that describes the total angular momentum of the H_2 molecule within the cage [55]. In the case of neutron scattering spectroscopy, only states within the ground vibrational state are probed. Hence, the vibrational quantum number ν is omitted from the label of the energy states probed with INS. The energy states are instead labelled with the $(J\, n\, l\ \lambda)$ expression.

The total energy of the entrapped molecules is described using the following expression:

$$E(\nu,\, j,\, n,\, l,\, \lambda) = \hbar((\nu + \frac{1}{2})\omega_\nu + (n + \frac{3}{2})\omega_n + B_\nu J(J+1) + c(l,\, j,\, \lambda)V_{T-R}) \tag{3.2.1}$$

where ω_ν is the molecular vibrational quantum of energy; ω_n is the molecular translational quantum of energy; $B_\nu = B_e - \alpha_e(\nu + 1/2)$ is the rotational constant at vibrational state ν while a_e is the vibration-rotation correction; and V_{T-R} is the translation-rotation coupling term with coefficient $c(l,\, j,\, \lambda)$. The translational rotational coupling term is responsible for the pattern of the TR sublevels. The degeneracy of each energy levels in Equation 3.2.1 is expressed as $g = 2\lambda + 1$.

Theoretical energy levels of $H_2@C_{60}$ have been computationally calculated by Xu et al by simulating the 5D potential energy surface (PES) for H_2 inside the C_{60} [44, 45, 46, 47]. The 5D PES is obtained by calculating the Lennard-Jones interactions of each proton in H_2 with the individual carbon atoms of the cage. The simulated 5D PES of H_2 along the C_2 axis of the C_{60} is illustrated in Figure 3.2.1 [46]. The solid and dashed lines are PES of H_2 which are perpendicular and parallel to the C_2 axis respectively. It can be seen that both PES resembles the potential energy of a harmonic oscillator. The calculated energy levels which are based on the 5D PES in Figure 3.2.1 are compiled into an energy level diagram shown in Figure 3.2.2. This energy level diagram is used as a reference for the assignments of the INS peaks in the next chapter.

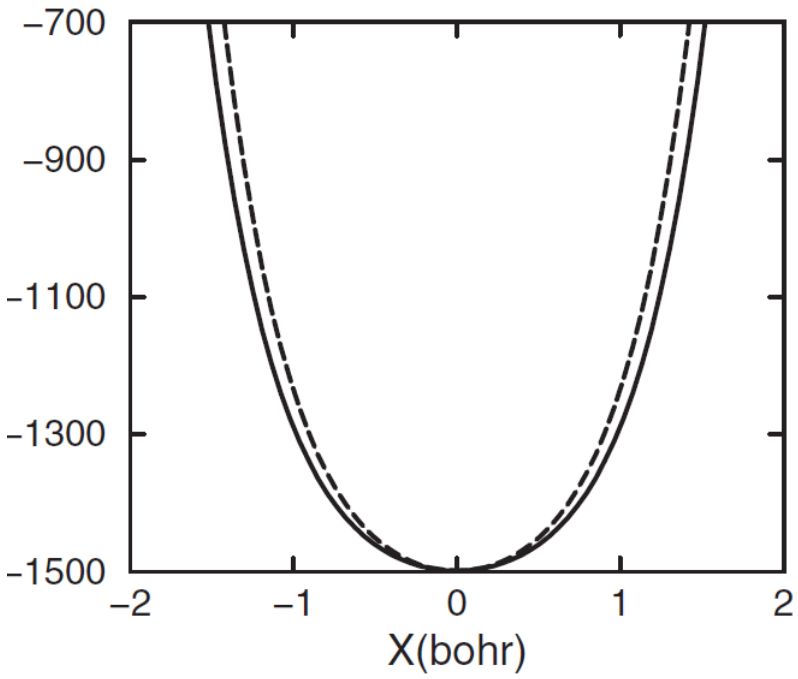

Figure 3.2.1: Simulated 5D PES of H_2@C_{60} for H_2 perpendicular (solid line) and parallel (dashed line) to the C_2 axis of the C_{60} [46].

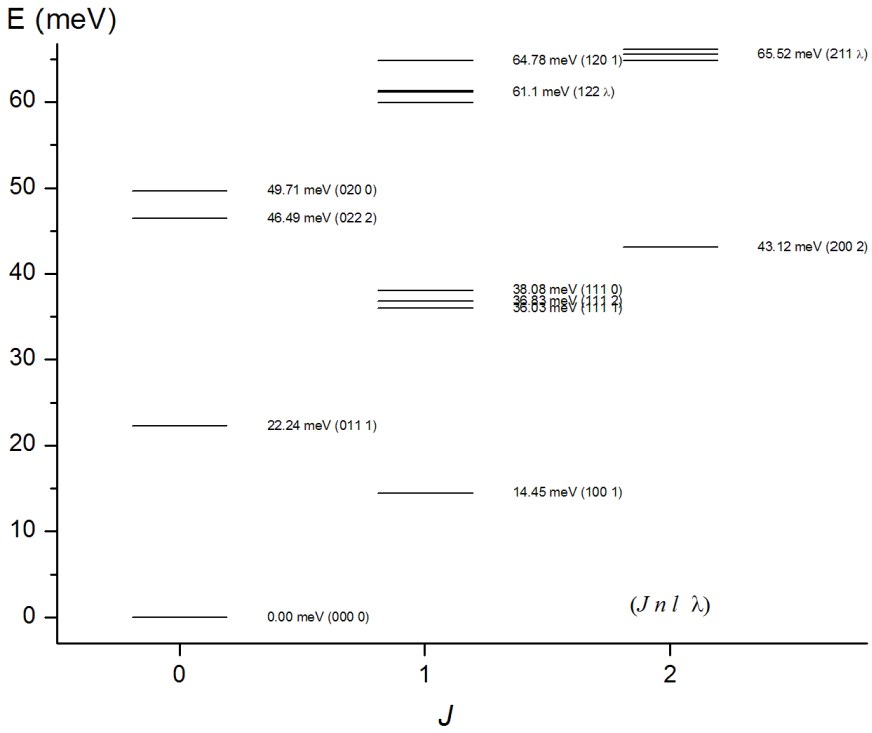

Figure 3.2.2: Energy level diagram of H_2@C_{60} as calculated by Xu et al [47].

3.3 Previous experiments

Collaborative experimental studies of the $H_2@C_{60}$ have been performed by groups in Southampton, Tallinn and Nottingham using various spectroscopic techniques such as NMR [49, 50, 51, 55], far infrared (FIR) [52, 53, 54, 55] and INS [55, 34]. Each of the three spectroscopic techniques used have their own unique advantage in studying the energy levels, spin isomerism and quantum dynamics of $H_2@C_{60}$.

A perfectly isolated homonuclear diatomic molecule such as H_2 generally does not display infrared activity [56]. However, this rule does not apply when there are intermolecular interactions between the H_2 and the environment, such as in the case of solids and liquids [57, 58]. Hence, the far-infrared (FIR) lines observed from the $H_2@C_{60}$ sample shows that there exists a symmetry breaking potential from the environment of the system. This potential could possibly arise from the deformation of the cages, crystal field, or carbon isotopomers in the cage [52, 53, 54]. FIR experiments involve the excitation of the vibrational states, however their transitions are constrained by the selection rules. It transpires that no pure rotational transition can be observed via FIR [52, 53, 54].

It has been shown by Xu et al through quantum calculations of the INS transition probabilities of $H_2@C_{60}$ that certain neutron interactions are subjected to selection rules [47], despite it being commonly stated that INS spectra have no selection rules [48]. Hence, pure rotational, pure translational or combination of translational and rotational (TR) transitions are allowed with neutrons (see Equation 2.1.3). INS also allow for the probing of the entrapped H_2 without exciting its vibrational state [34]. However, unlike the ortho-ortho and para-ortho transitions, transitions between two para states are only dependent on the coherent scattering cross section of protons, which is 46 times smaller than the incoherent scattering cross section (see Section 2.1.1). Hence, para to para transitions do not make measurable contribution to the INS spectra.

NMR spectroscopy is useful for studying magnetic interactions between the individual proton spins of the entrapped small molecules as well as interactions with the environment. However, the technique is unable to induce higher energy transitions to probe the translational, rotational and vibrational states.

In all cases, the high level of isolation experienced by the entrapped hydrogen molecules results in the observation of narrow and unambiguous ^1H spectral features. This level of isolation is attributed to the highly

symmetric and relatively isolated environment provided by the fullerene cages. Nuclear spin-isomer conversion between ortho and para species is not observed in any of the FIR, INS and NMR experiments of $H_2@C_{60}$.

Chapter 4

INS spectral analysis of $H_2@C_{60}$

All of the INS experiments on $H_2@C_{60}$ described in this chapter were performed by A. J. Horsewill, S. Rols and M. R. Johnson at the ILL, Grenoble. The analysis of the temperature dependence IN5 spectra of $H_2@C_{60}$ were undertaken by myself and are discussed in detail in this chapter. However, it is necessary to discuss the earlier analysis of the low temperature IN4C spectra, as these results form an important foundation for my analysis of the IN5 spectra.

4.1 Low temperature thermal neutron scattering

The initial INS study on the $H_2@C_{60}$ was done using the IN4C spectrometer (see Section 2.1.3), which uses high flux thermal neutrons, at 1.6 K sample temperature (Figure 4.1.1) [34]. The IN4C spectra have been recorded using incident neutron wavelengths of 1.1, 1.2 and 1.6 Å respectively. The shorter incident neutron wavelengths are used to probe the higher energy states, albeit having a lower resolution. The aim of this experiment is to obtain the overview of the energy level structure of the system. IN4C provides a good overview of the system, as it probes both NE gain and loss regions of the spectrum; whereas IN5 only probes the NE gain region but provides significantly better resolution. The energy states of $H_2@C_{60}$ are labelled with the expression $(J\,n\,l\;\lambda)$, where J, n and l are the rotational, principle and translational quantum numbers respectively, while λ is the translation-rotation (TR) quantum number.

At 1.6 K, only the ground states of both spin species (ortho- and para-H_2) are populated. Hence, the peaks in the recorded spectra will have to originate from either the ortho ground state (101 1) or the para ground

state (000 0). The nature of the transitions associated with each peak can also be determined by referring to the momentum transfer data of each peak [34]. The momentum transfer analysis of the 1.1 Å $H_2@C_{60}$ spectrum has previously been done [34] by my supervisor, Anthony J. Horsewill. All of the energy transfer spectra discussed are summed over all scattering angles or momentum transfer spectra. The theoretical energy level diagram calculated by Xu et al (see Figure 3.2.2) can be used as a reference to estimate the energy value of each quantum state [46]. With the aforementioned knowledge and knowing that transitions between two para states are not observable, the energy level table (Table 4.2) can be constructed by fitting and assigning the peaks to their respective transitions. The notable peaks in the spectrum are those at -14.7 meV and 14.7 meV, as they represents the transitions between the ground states of the two species. The 8.08 meV and 29.2 meV peaks indicate TR transitions from the ortho ground state to the (011 1) and (200 2) para states respectively. The resolved 22.17 meV, 22.88 meV and 24.3 meV peaks indicate pure translational transition from the ortho ground state to the (111 λ) states. The structure between 26 meV and 34 meV consists of transitions from the the ortho ground state to the (200 2), (022 2) and (020 0) para states respectively. However, not all of the TR fine structures could be resolved with IN4C. The unresolved (122 λ) band is indicated by the peak centred at 46.6 meV. The energy level diagram of $H_2@C_{60}$ (Figure 4.1.2) can be constructed based on the energy transfer values in Table 4.2. The magnitude of the splitting of the (122 λ) band shown in the energy level diagram are obtained from the theoretical model calculated by Xu et al [46].

To explore the higher energy transitions, shorter incident neutron wavelength (λ_n) neutrons will have to be used. However, the structure of the higher energy states cannot be resolved due to the lower resolution limit of the higher energy neutrons. Cold neutrons are used instead to resolve the structure of the higher energy states by probing the NE gain region.

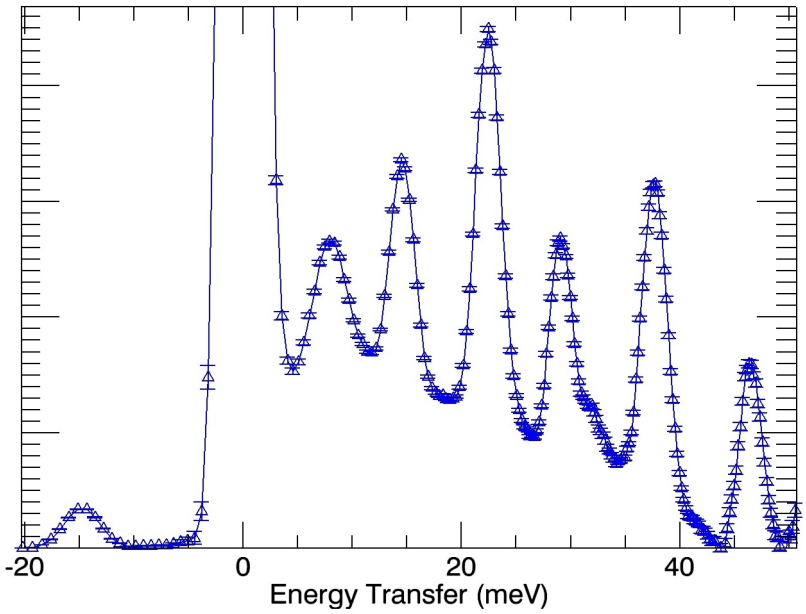

Figure 4.1.1: $H_2@C_{60}$ INS spectra recorded with IN4C using $\lambda_n = 1.2$Å at 1.6 K sample temperature. See text for the assignment of the peaks in the spectrum. The assigned initial and final states of the respective peaks are compiled into Table 4.1. The signal contribution from the empty C_{60} cages have been subtracted by performing a separate measurement on the "blank" C_{60} sample [34].

$H_2@C_{60}$ observed INS transitions.

Initial State (J n l λ)	Final state (J n l λ)	Energy Transfer (meV)
000 0	100 1	14.69 ± 0.05
100 1	011 1	8.08 ± 0.03
100 1	200 2	29.2 ± 0.2
100 1	111 1	22.17 ± 0.05
100 1	111 2	22.88 ± 0.05
100 1	111 0	24.3 ± 0.1
100 1	200 2	29.3 ± 0.1
100 1	022 2	32.4 ± 0.1
100 1	020 0	34.8 ± 0.1
000 0	111 0,1,2	37.8 ± 0.1 *
100 1	122 1,2,3	46.6 ± 0.1 *
100 1	000 0	-14.69 ± 0.05

*Indicates band centre of an unresolved multiplet

Table 4.1: Compilation of the $H_2@C_{60}$ INS transitions observed in the 1.2Å IN4C spectra shown in Figure 4.1.1 [34]. The (111 λ) triplet is resolved clearly from the transition originating from the ortho ground state (100 1) to the (111 λ) states. This splitting is also observed from the broader than resolution peak that represents the transition from the para ground state (000 0) to the (111 λ) states. The (122 λ) states are unable to be resolved from the spectrum.

J	n	l	λ	Energy (meV)
0	0	0	0	0.0
1	0	0	1	14.70 ± 0.03
0	1	1	1	22.78 ± 0.05
1	1	1	$\lambda^{(a)} = 1$[a]	36.87 ± 0.07
1	1	1	$\lambda^{(b)} = 2$[a]	37.58 ± 0.07
1	1	1	$\lambda^{(c)} = 0$[a]	39.0 ± 0.1
2	0	0	2	44.0 ± 0.1
0	2	2	2	47.1 ± 0.2
0	2	0	0	49.5 ± 0.2
1	2	2	3,2,1	61.3 ± 0.1[b]

Table 4.2: Table showing the energy values of the respective states based on the analysis of the IN4C spectrum (Figure 4.1.1). The states labelled with *a* are resolved from the IN4C spectrum [46]. The energy value labelled with *b* indicates the band centre of the (122 λ) states, which are unresolved in the spectrum [34]

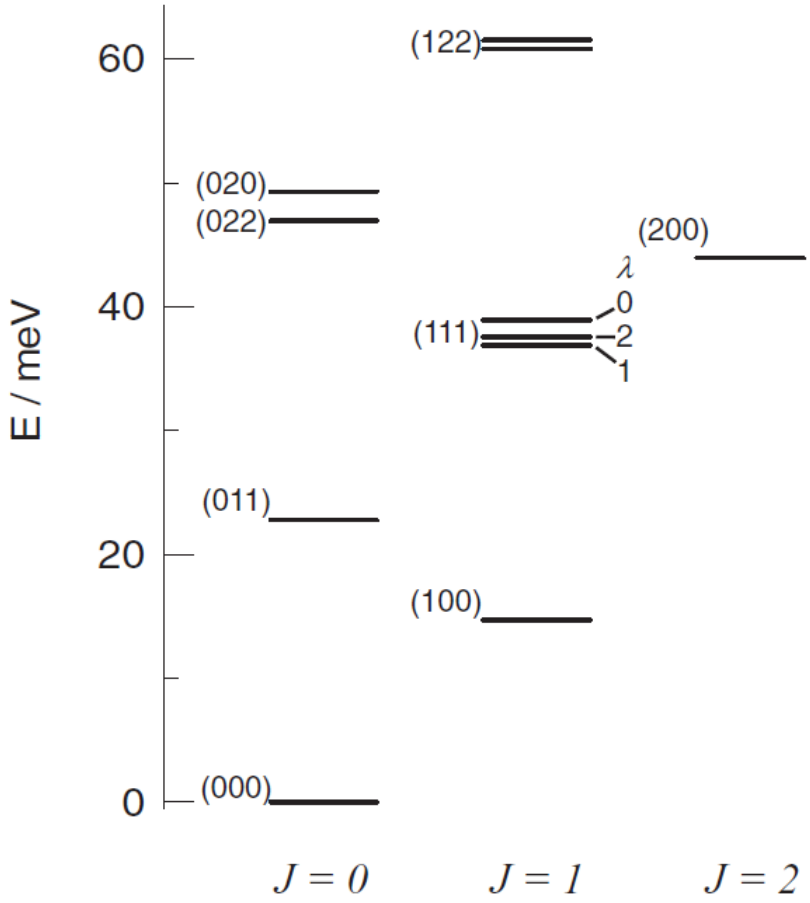

Figure 4.1.2: The energy level diagram of $H_2@C_{60}$ based on the energy values of Table 4.2. The illustrated TR fine structure of the (122) state in the diagram is based on the theoretical calculations by Xu et al [46].

4.2 Temperature dependence study using cold neutron scattering

The cold neutron experiments were performed using the high resolution IN5 spectrometer (see Section 2.1.4). IN5 is a disk-chopper time-of-flight spectrometer operating on a cold neutron beam line. Cold neutron scattering is mainly used to probe NE gain transitions as the incident neutrons do not have enough energy to excite the sample. The experiments are recorded using 8Å incident neutron wavelength and with sample temperatures ranging between 1.5 K and 240 K. The aim of this experiment is to obtain the temperature dependence of the amplitudes of the peaks to study the statistical distribution of the TR states. The study of the statistical distribution of a TR state allows us to extract information such as the degeneracy and the energy of the state. The intensity of the peak is dependent on the population of the initial state and the transition probability (as shown in Equation 4.2.1). Therefore, higher sample temperature is required to populate the higher energy states to record the de-excitation of the higher energy states to the lower energy states. As a result, new peaks will appear as temperature is increased.

Some of the peaks in the NE gain part of the spectra are "mirror counterparts" of the peaks in the NE loss side (as seen in the IN4C spectrum in Figure 4.1.1), with those NE gain peaks possessing identical but negative energy transfer values as their NE loss counterparts. Hence, as temperature is increased, we would expect to see the appearance of peaks at energy transfer values equal in magnitude but opposite in sign to the one seen in Figure 4.1.1. In addition to the peaks observed in Figure 4.1.1, a few other peaks are also expected to appear at the higher temperature IN5 spectra (see Figure 4.2.1). Such peaks represent transitions from higher energy states to the lower energy non-ground states, which is not observed in the IN4C spectrum due to it being recorded at temperatures where only ground states are populated. These new peaks may be used to refine our knowledge of the energies of the $H_2@C_{60}$ states [34].

One particularly striking feature that can be observed from the IN5 spectra (Figure 4.2.1) is that the peaks are remarkably clustered within a small energy transfer region even when higher energy states are populated. This is partly attributed to the almost spherically symmetric cage that results in an almost harmonic cage potential, where the translational energy is almost linearly proportional to the translational quantum number n, thus giving rise to a "translational cluster" of peaks. The difference in

energy between the translational ground state and its immediate translationally excited state is 22.5 meV. However, the size of this "translational energy step" increases gradually with n due to the slightly anharmonic cage potential [46]. Hence, at temperatures where only first translationally excited states are occupied, peaks are expected to appear around the -22.5 meV region. As temperature is further increased, more peaks are expected to appear around a slightly lower energy transfer region ($\Delta E < -22.5$ meV). Another prominent cluster of peaks is the "rotational cluster", which contains pure rotational transitions.

Hence, it is convenient that the analysis of the IN5 spectra of up to 280 K be divided into two regions, the "translational region" (-32 meV$\leq \Delta E \leq$-18 meV) and the "rotational region" (-16 meV$\leq \Delta E \leq$-13 meV).

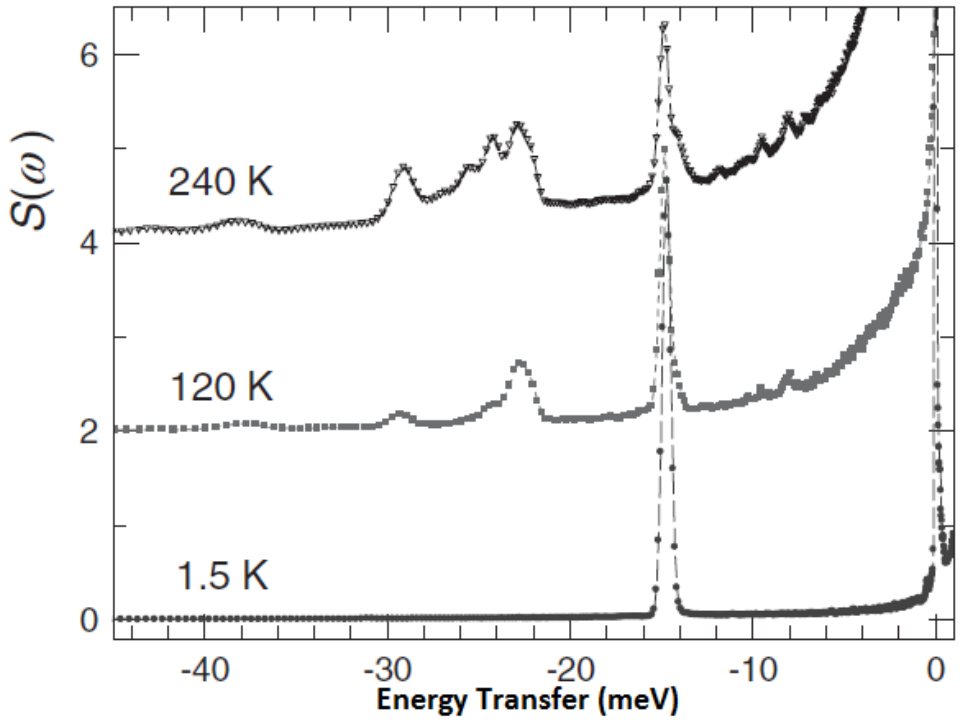

Figure 4.2.1: IN5 spectra $H_2@C_{60}$ recorded at 240 K, 120 K and 1.5 K respectively using λ_n= 8Å. The peak centred at -14.7 meV is the pure rotational transition between the ground state of ortho and para species. As temperature is increased, it can be seen that peaks in the region of -35 meV to -20 meV begin to appear. These peaks represents pure translational and translation-rotational (TR) transitions, as the translational excitation energy between each translational quantum states are ~25meV (see Table 4.1). The peaks that are located in the region between -35 meV and -20 meV are elaborated in Figure 4.2.2. High resolution peaks (FWHM≈ 0.5 meV) can be observed in the region between -13 meV and 0 meV. These peaks represent transitions between higher energy states. Details of the analysis of the peaks in this region can be found in the paper by Horsewill et al [34].

4.2.1 Translational region (-32 meV$\leq \Delta E \leq$-18 meV)

In the analysis of the peaks within the -32 meV$\leq \Delta E \leq$-18 meV energy transfer region, it is assumed that the highest occupied state is the (131 2) state. This assumption is valid for this analysis as our highest sample temperature spectrum is recorded at 280 K, whereas the peak Boltzmann population of the (131 2) state would be at 777 K. With this assumption, we can identify 43 different transitions with energy transfer values between -30 meV$\leq \Delta E \leq$-22 meV from the energy level diagram in Figure 4.1.2. These 43 transition peaks are combined into 7 different Gaussians to reduce the number of variables used for the fitting, as there are only 38 observable points in this region of the spectra. The breakdown of these 7 "combined Gaussians" are shown in Table 4.3. The combined Gaussian transition energy values are the average values of the respective transitions that they represent. The fitting and analysis of this region of the IN5 spectrum is published in Philosophical Transaction of the Royal Society in 2013 [59].

In the fitting model, all of the 7 Gaussians are set to have a fixed transition energy value and width. The width of each combined Gaussians are determined from the two effects: the resolution function of IN5, which increases systematically with increasing $|\Delta E|$; and the broadening due to multiple transitions represented by a single combined Gaussian (Table 4.3) covering a range of energy transfer. Taking the two effects into account: the -22.17 meV and -22.88 meV Gaussians are modelled with 0.9 meV FWHM; the -24.3 meV Gaussian is modelled with a 1.5 meV FWHM; the -25.5 meV, -26.4 meV and -27.5 meV Gaussians are modelled with widths of 1.0 meV; and the -29.2 meV Gaussian with width of 1.7 meV. An additional linear background is added accordingly to accompany the Gaussian fits. The amplitude of the Gaussian curves obtained as a result of the fitting are then recorded accordingly. This process is then repeated for spectra of different temperatures (see Figure 4.2.2). The collective Gaussian amplitudes of different temperatures are then plotted to form Figure 4.2.3.

It can be seen from the 65 K IN5 spectra in Figure 4.2.2 that only the (111 λ) state (first excited translational states) is occupied. This is evident from the -22.17 and -22.88 meV Gaussians appearing in the spectrum. Both peaks increases systematically with temperature until approximately 200 K, when they begin to slowly diminish. At 120 K, we begin to see the emergence of the -24.3 and -29.2 meV Gaussians, which originates from the (122 λ) and (120 0) states (both are second excited translational states) respectively. The -25.5, -26.4 and -27.5 meV Gaussians which originates

from the (133 λ) states (third excited translational state) begin to emerge in the 140 K spectrum and are seen to systematically grow in intensity with temperature up till 280 K. The growth in intensities of the -24.3 and -29.2 meV Gaussians with temperature up till 280 K is attributed to the contributions from the transitions originated from the (133 λ) states.

		$(J\,n\,l\,\lambda)$	$(J\,n\,l\,\lambda)$				$(J\,n\,l\,\lambda)$	$(J\,n\,l\,\lambda)$	
Combined Gaussian peak position (meV)		**Initial State**	**Final State**	**Energy Transfer (meV)**	**Combined Gaussian peak position (meV)**		**Initial State**	**Final State**	**Energy Transfer (meV)**
(0.66 meV)	**-14.7**	100 1	000 0	-14.69	(1.0 meV) (FWHM)	**-26.4**	133 3	122 2	-26.17
		111 2	011 1	-14.8			133 4	122 3	-26.5
(0.61 meV)	**14.09**	111 1	011 1	-14.09			133 4	122 1	-26.31
(0.9 meV) (FWHM)	**22.17**	111 1	100 1	-22.08			133 2	122 3	-26.78
		122 2	111 0	-22.32			133 2	122 1	-26.59
(0.9 meV)	**22.88**	111 2	100 1	-22.88			131 1	120 0	-26.5
		120 1	200 2	-22.82			131 1	211 2	-26.28
		133 2	211 2	-22.88	(1.0 meV)	**-27.5**	120 0	111 0	-27.24
		133 4	211 2	-22.6			133 4	122 2	-27.74
		133 2	120 0	-23.1			133 2	122 2	-28.02
(1.5 meV)	**-24.3**	111 0	100 1	-24.16			131 2	211 3	-27.07
		122 2	111 1	-24.4			131 2	211 1	-26.96
		122 3	111 2	-24.84			211 2	111 0	-27.46
		122 2	111 2	-23.6	(1.7 meV)	**-29.2**	120 0	111 2	-28.52
		122 1	111 0	-23.75			120 0	111 1	-29.32
		122 3	111 0	-23.56			131 1	122 1	-29.9
		133 3	122 1	-24.74			131 2	120 0	-28.57
		131 1	211 1	-24.89			131 2	211 2	-28.35
(1.0 meV)	**-25.5**	122 3	111 1	-25.64			200 2	100 1	-29.51
		122 1	111 1	-25.83			211 2	111 1	29.54
		122 1	111 2	-25.03			211 2	111 2	-28.74
		133 3	122 3	-24.93			211 3	111 0	-28.74
		131 1	211 3	-25			211 1	111 0	-28.85

Table 4.3: The breakdown of the 7 "combined Gaussians" that are used to fit the peaks in the -32 meV$\leq \Delta E \leq$-18 meV energy transfer region, as well as the 2 Gaussians that are used to fit the -17 meV to -13 meV energy transfer region. The breakdown of the 7 Gaussians show 43 different transitions falling within the -32 meV$\leq \Delta E \leq$-18 meV energy transfer region, assuming that highest occupied state being the (211) state. The energy value in the brackets next to the peak positions signifies the respective full width half maximum (FWHM) of the combined Gaussian.

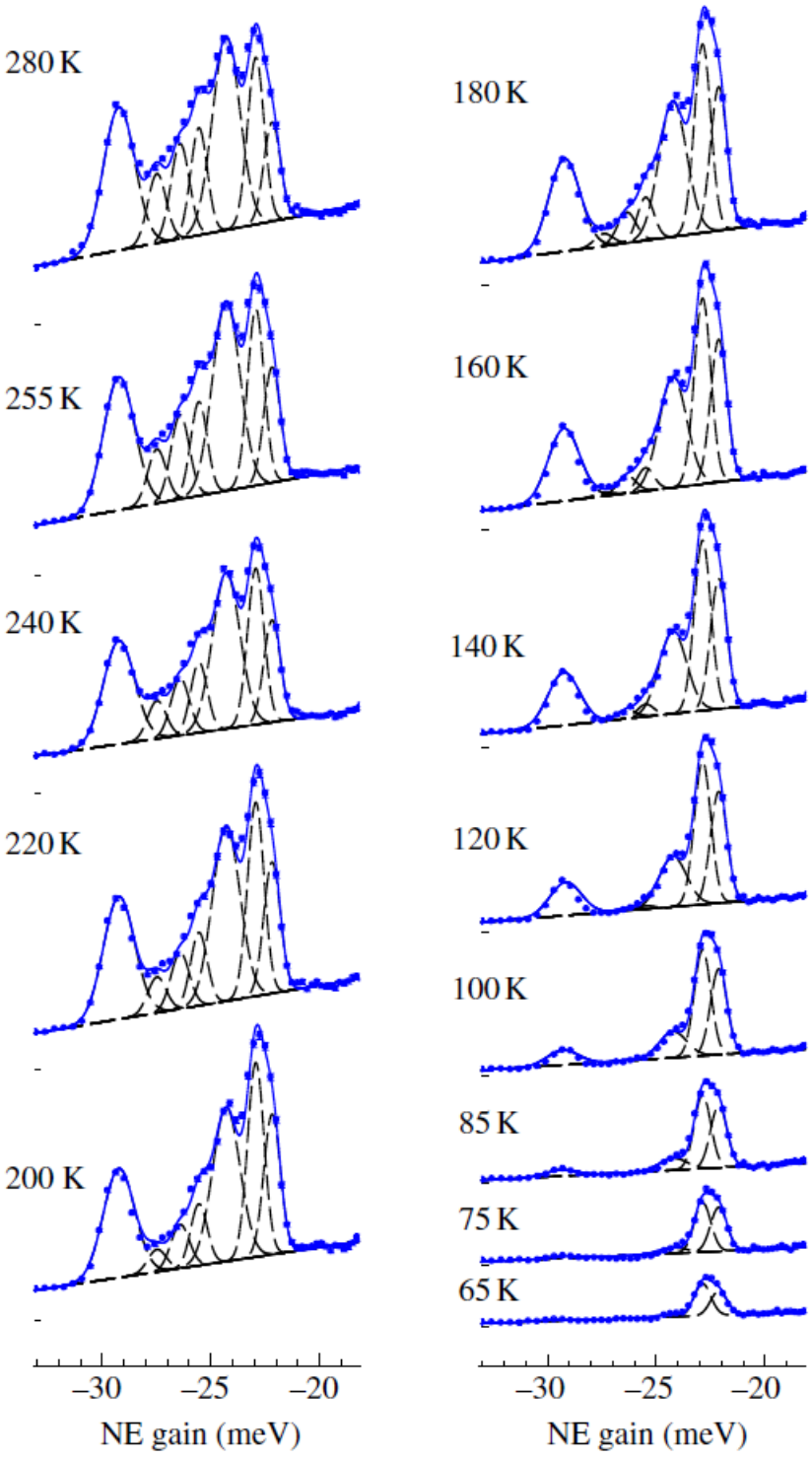

Figure 4.2.2: Fitting of the $H_2@C_{60}$ IN5 spectra recorded at sample temperatures ranging between 65 K and 280 K in the -32 meV> ΔE >-18 meV region using the 7 Gaussians in Table 4.3. See text for information on the fitting constraints and details of the spectra. [59].

Boltzmann equation: The temperature dependence plot of the combined Gaussian amplitude (Figure 4.2.3) can be described using a segment of Equation 2.1.1, with the exception that the range of the sum is limited to

transitions represented by a combined Gaussian. This segment of Equation 2.1.1 can then be rewritten as:

$$F_c = \sum_{i,f \in S_c} n_i | < i|V|f > |^2 = \sum_{i,f \in S_c} n_i^{o,p}(T)\, p_{if} \tag{4.2.1}$$

where p_i is the transition probability of a transition from initial state i to final state f, while S_c is the subset that contains all the transitions represented by the combined Gaussian, c. Equation 4.2.1 describes the sum of the $n_i\, p_{if}$ product of all the transitions that are represented by the combined Gaussian. $n_i^{o,p}$ is the Boltzmann equation of the initial state i, which is described by the following equation:

$$n_i^{o,p} = g_i^{o,p}\, \exp \frac{(-E_i^{o,p}/k_b\, T)}{Z^{o,p}} \tag{4.2.2}$$

where $g_i^{o,p}$ and $E_i^{o,p}$ are the degeneracy and energy of state i respectively, while k_b, $Z^{o,p}$ and T are the Boltzmann constant, partition function and sample temperature respectively. The superscript o, p signifies either ortho or para species, which have their own separate statistical distributions due to the absence of nuclear spin-isomer conversion between the ortho and para species at low temperatures. The general equation for the partition function, $Z_{gen}^{o,p}$, is written as:

$$Z_{gen}^{o,p} = \sum_{i=0}^{\infty} g_i^{o,p}\, \exp(-E_i^{o,p}/k_b\, T) \tag{4.2.3}$$

Theoretically, the transition probability can be determined by fixing the degeneracy and energy value of the initial state of the transition. However, due to the difficulty in separating the individual $n_i\, p_{if}$ term from the temperature dependence of the combined Gaussian amplitude data, the information on the transition probability of each individual transitions cannot be accurately extracted. This difficulty arises from the small difference in energy between some of the transitions within the combined Gaussian. Nevertheless, the magnitude of each transition probability can still be compared to determine the dominance of each transition.

The fitting of the temperature dependence plot of the combined Gaussian amplitudes in the -32 meV> ΔE >-18 meV energy transfer region is shown in Figure 4.2.3. Each fitting line is the the admixture of the Boltzmann equation (Equation 4.2.1) of their respective transitions shown in Table 4.3. Based on the temperatures in which the peaks appear, it can be concluded that: the -22.17 meV and -22.88 meV peaks originate from

the low energy states; -24.3 meV and -29.2 meV peaks originate from intermediate states; -25.5 meV and -26.4 meV peaks originate from the high energy states; and the -27.5 meV peak originates from even higher energy states.

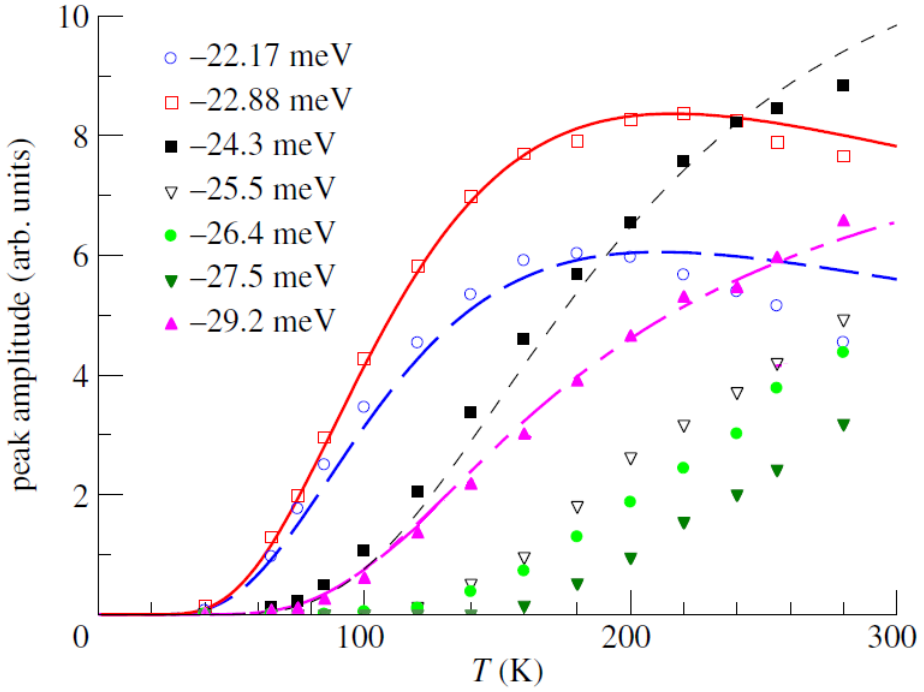

Figure 4.2.3: Temperature dependence plot of the amplitudes of the combined Gaussians obtained from the fit in Figure 4.2.2. The solid and dotted lines are the respective admixture of the Boltzmann equation (Equation 4.2.1) of the initial states shown in Table 4.3, using the general partition function (Equation 4.2.3). It can be seen that the -22.17 meV, -22.88 meV and -24.3 meV lines do not fit well to the data at higher temperatures.

However, it can be seen that the -22.88 meV, -22.17 meV and -24.3 meV lines in Figure 4.2.3 fit well to the data at low temperatures, but fit less well to the data at higher temperatures. This is attributed to the negligence of the nuclear spin-isomer conversion occurring at higher temperatures. The statistical contribution from the high temperature energy states of the opposite spin species can be taken into account by rewriting the partition function as:

$$Z^{o,p} = \sum_{i=0}^{\infty} g_i^{o,p} \exp(-E_i^{o,p}/k_b T) + \sum_{i=q_{p,o}}^{\infty} g_i^{p,o} \exp(-E_i^{p,o}/k_b T) \qquad (4.2.4)$$

where $q_{p,o}$ is the lowest energy state of the opposite spin species (either para or ortho) in which nuclear spin-isomer conversion occurs. This modified

partition function implies that the nuclear spin-isomer conversion occurs only at temperatures high enough to occupy the $q_{p,o}$ energy state. This modified partition function assumes that there are no nuclear spin-isomer conversions between energy states which are lower than $q_{p,o}$, even at high temperatures. It also assumes instantaneous nuclear spin-isomer conversion at high temperatures. In reality, the occurrence of the nuclear spin-isomer conversion is dependent on temperature instead of the occupation of certain energy state. However, this modified partition function remains valid, as the occupation of the $q_{p,o}$ state is also dependent on temperature, while the population of the opposite spin-species states with energy lower than the $q_{p,o}$ state is relatively small at higher temperatures.

A similar fit is performed on the same set of temperature dependence data, using the modified partition function (Equation 4.2.4) instead of the general partition function (Figure 4.2.3). The q_p and q_o states are chosen to be the (211 2) state (66.22 meV) and the (300 3) state (81.6 meV) respectively, as both states begin to populate at around the same temperature (60 K). It can be seen that the use of the modified partition function provides a better fit to the data at higher temperatures as compared to the use of the general partition function. The result of the fittings show different level of statistical weightings from each transition in each combined Gaussian. In the case of the fittings of the -22.17 meV, -22.88 meV and -24.3 meV plots, the statistical weightings of the (111 λ) states dominate; whereas the higher energy (131 λ) states dominate in the fittings of the -25.5 meV, -26.4 meV and -27.5 meV plots. The fitting of the -29.2 meV plot shows almost equally dominant weighting between the (120 0) and (131 λ) states.

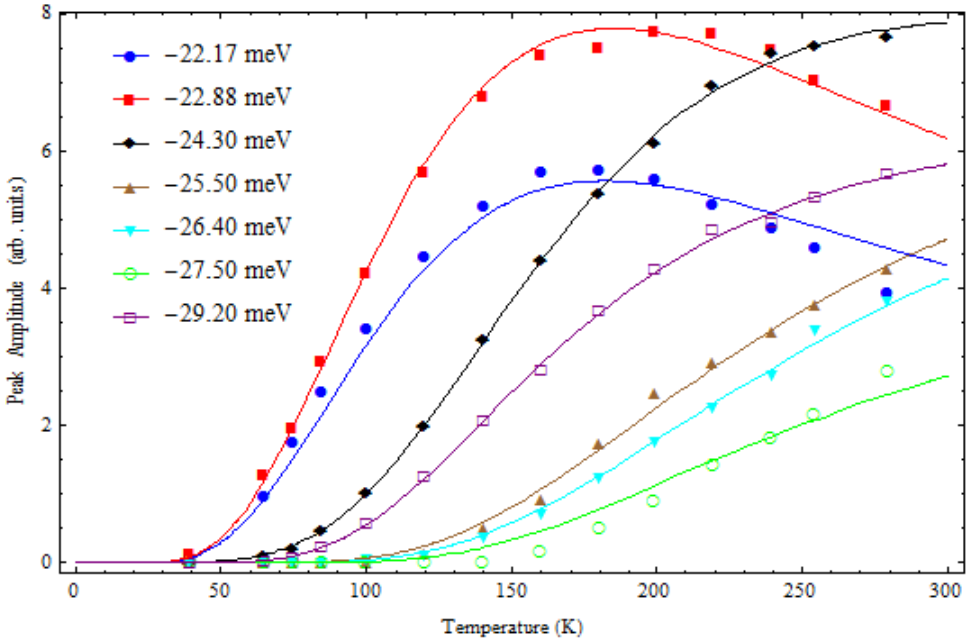

Figure 4.2.4: The fitting of the identical temperature dependence plots as the one seen in Figure 4.2.3 using the modified partition function (Equation 4.2.4) instead of the general partition function. These lines are the computational fits of the respective dots of the same colour. It can be seen that the use of the modified partition function provided a better fit to the data at higher temperatures as compared to the fit using the general partition function (Figure 4.2.3). The brown, cyan and green data points are transitions that originates from the (133) states. Hence, we only see a rise in the amplitude at higher energies.

4.2.2 Rotational region (-16 meV$\leq \Delta E \leq$-13 meV)

As for the -16 meV$\leq \Delta E \leq$-13 meV energy transfer region, three transitions are identified from the aforementioned energy level diagram (Figure 4.1.2). Two of the transitions, which includes the rotational ortho to para ground state transitions (-14.7meV), is merged into a single Gaussian (Table 4.3). A similar procedure as the one used for fitting the -32 meV$\leq \Delta E \leq$-18 meV region is applied, with the exception that the position of the -14.7 meV Gaussian is allowed to float due to the effect of the rotational fine structure shifting the position of the principal rotational transition at lower temperatures. Analysis of this rotational fine structure is discuss in the later part of this section. Spectra with sample temperatures between 1.5 K to 280 K are used for this analysis (Figure 4.2.5). The width of the -14.7 meV and the -14.09 meV Gaussians are set to 0.66 meV and 0.61 meV respectively due to the two aforementioned effects. At temperatures below 65K, the -14.09 meV Gaussian is negligible as the (111 λ) states are not populated. At higher sample temperatures, the -14.09meV Gaussian becomes more significant.

The temperature dependence plot of the two Gaussian amplitudes are shown in Figure 4.2.6. A similar fitting procedure to the one used in Figure 4.2.4 is applied onto the temperature dependence plot of the -14.69 meV and -14.09 meV combined Gaussian amplitude data (Figure 4.2.6). The -14.69 meV fit shows almost equal weightings between the (100 1) and (111 2) states; whereas there is only one transition within the -14.09 meV Gaussian, which is the transition originating from the (111 1) state.

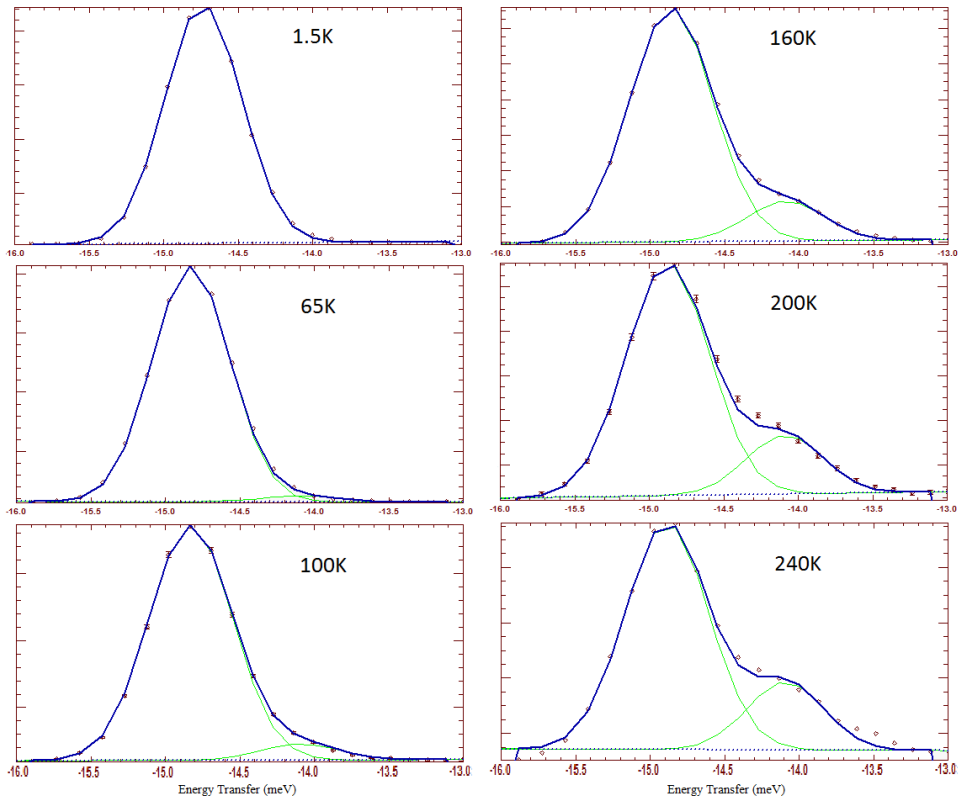

Figure 4.2.5: Fitting of the $H_2@C_{60}$ IN5 spectra recorded at sample temperatures of 1.5, 65, 100, 160, 200 and 240 K respectively in the -16 meV> ΔE >-13 meV region. The positions of the two Gaussians used to fit the spectra are -14.7 meV and -14.09 meV respectively.

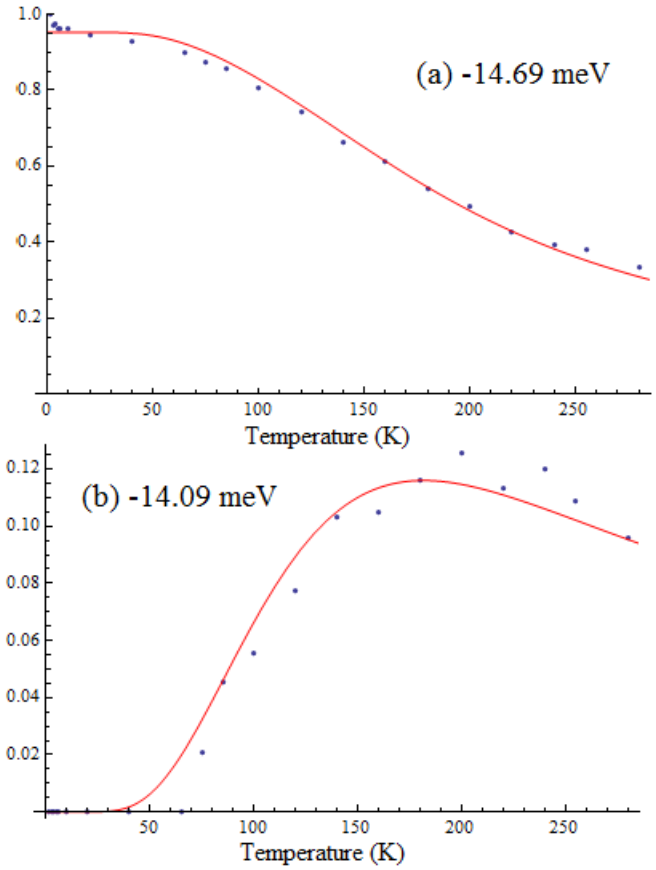

Figure 4.2.6: Temperature dependence plot of the amplitudes (blue dots) of the two combined Gaussians (-14.7 meV and -14.09 meV) obtained from the fit shown in Figure 4.2.5. The red line is the fit of the temperature dependence Gaussian amplitudes data using Equation 4.2.1. (a) The -14.69 meV fit shows almost equal weightings between the (100 1) and (111 2) states. (b) Fit of the Boltzmann equation of the (111 1) state to data. Both figures show good fit to data.

4.2.2.1 Splitting of the ortho-H_2 ground state

The shift in the position of the principal rotational peak with the lowering of the temperature is attributed to the lifting in the degeneracy of the ortho-H_2 ground state. This splitting of the ortho-H_2 ground state has been observed via specific heat measurements on this sample by Kohama et al to be in the order of 0.1-0.2 meV [60]. The shift in the principal rotational peak position as a function of temperature is recorded using high resolution ($\lambda_n = 8$Å) IN5 spectrometer and is plotted in Figure 4.2.7. It is shown that the position of the principal rotation peak begins to shift significantly at $T \leq 20$ K. The peak centres have been determined through Gaussian fitting. The principle rotation peak is the super position of the two peaks that originate from the split (100 1) states. The observed shift is the result of an increase in the intensity of the lower energy peak and a decrease in the intensity of the higher energy peak with lowering of the temperature.

One possible explanation to this splitting is that there may be two types of orientation of C_{60} and that these orientations can lead to two different crystal fields [60]. Analysis of the neutron diffraction data recorded with the IN5 has shown that the sample has a crystal symmetry that is lower than the cubic class adopted by pure forms of C_{60}. This lower crystal symmetry may be attributed to the impurities within the sample.

Another possible explanation to this symmetry breaking effect is the coupling between the electric quadrupole moment of ortho-H_2 and the crystal field. Recent INS experiment on the $H_2@C_{60}$ at milli-Kelvin temperatures have extended the data in Figure 4.2.7 to show that the size of the shift plateaus at -0.14 meV at milli-Kelvin temperatures. This suggests that the size of the splitting of the ortho-H_2 ground state is 0.14 meV and has a degeneracy distribution of 1:2 (lower:higher energy state) [61].

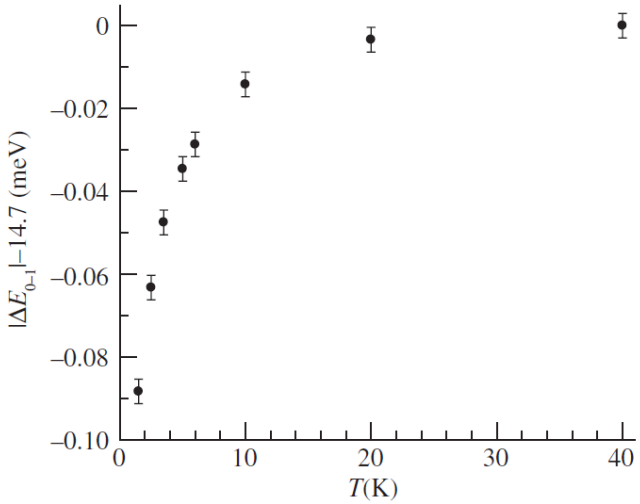

Figure 4.2.7: The temperature dependent shift in the position of the ortho ground state to para ground state transition peak ($|\Delta E_{0-1}| - 14.7$ meV). This data is recorded with IN5 using $\lambda_n = 8$Å.

4.3 Conclusions

The results from the temperature dependence study of the cold neutron scattering spectra have reinforced the view that the temperature dependence of the INS spectrum provides an effective tool for assigning spectral lines. These results have provided further insight on the energy states of $H_2@C_{60}$, as well as confirming the existence of the rotational fine structure which was previously observed by Komaha et al [60].

The study of the change in amplitude of the NE gain peak as a function of temperature allows for the "fine tuning" of the energy level diagram constructed from the NE loss spectra, as well as facilitating the peak assignments by determining the origin of the transitions. The downward transitions from different translational states can be identified by analysing the temperature at which the peak appears in the spectra. Besides determining the energy value of a state, information on its degeneracy can also be extracted. The high resolution that comes with cold neutron scattering allows for the study of the TR fine structure, as well as observing the temperature dependence shift in the spectral position of the principal rotation peak at low temperatures. This temperature dependent shift, which is in the order of 0.1 meV to 0.2 meV, could not be observed by lower resolution thermal neutron scattering.

The magnitude of this shift is consistent with the influence of the crystal field generated by the lattice ordering of the H_2 rotors onto the potential energy surface experienced by the encapsulated H_2. Hence, to a good approximation, the dynamics of the encapsulated hydrogen are dominated by the C_{60} cage potential. There is also a question on the impurity of the sample, which is shown to exist in this sample from the magic angle spectroscopy (MAS) NMR spectra recorded by S. Mamone in the University of Southampton [9]. Therefore, systematic assessment of this shift can only become viable once high volume of purified sample is available.

It is also shown that it is essential to take into account the nuclear spin-isomer conversion between the two spin species at higher temperatures by modifying the partition function to include the statistical contribution from the higher energy states of the opposite spin species. This is evident from the higher temperature fit ($T \geq 200$ K) of the temperature dependence of the combined Gaussian amplitude data using the modified partition function as compared to the non-modified version.

The overall study of the $H_2@C_{60}$ molecule has been essential in the study of the other two variants of small molecule endohedral fullerenes ($H_2@C_{70}$

and $H_2O@C_{60}$), which are discussed in the subsequent parts of the thesis.

Part III

$H_2@C_{70}$

Chapter 5

Theory and properties of $H_2@C_{70}$

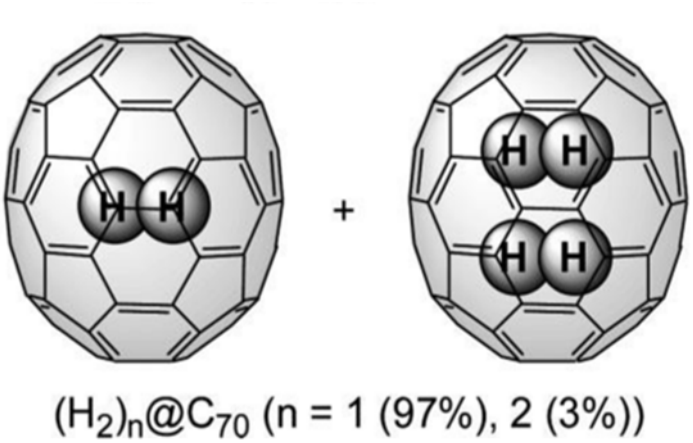

Figure 5.0.1: Schematic of the $H_2@C_{70}$ and $(H_2)_2@C_{70}$ supramolecular complex.

The encapsulation of the H_2 molecule inside a C_{70} cage allows the study of the effect of having an elongated prolate ellipsoidal cage on the dynamics of the entrapped molecule. Besides having a cage that has one axis (z-axis) that is longer than the other two (x and $y-$axes), the properties of $H_2@C_{70}$ are similar to those of $H_2@C_{60}$. The lower cage symmetry results in significant consequences on the molecular dynamics of the entrapped H_2. One would expect that the ellipsoidal rotations and translations about the larger $zx-$ or zy-planes have lower energies than those about the smaller xy-plane. Hence, one would expect twice the number of non-degenerate states due to the lower symmetry cage.

The $H_2@C_{70}$ molecule is synthesised using a similar molecular surgery method [4] as the $H_2@C_{60}$. The synthesis of the $H_2@C_{70}$ results in approximately 3% of the molecule having two H_2 molecules encapsulated inside a single cage. As the doubly occupied C_{70} cage ($(H_2)_2@C_{70}$) only forms a small fraction of the sample, it is largely neglected in our study of the

sample. The $H_2@C_{70}$ sample is in the form of black powder similar to the $H_2@C_{60}$ sample.

5.1 Molecular dynamics of $H_2@C_{70}$

$H_2@C_{70}$ has very similar properties to the $H_2@C_{60}$. However, due the change of cage symmetry, it is necessary to define the quantum numbers of the entrapped H_2 in a different way. The quantum numbers are the rotational quantum number J; translational angular momentum quantum number along the xy-plane ν_{xy}; the vibrational angular momentum quantum number along the xy-plane $|l| = -\nu_{xy}, -\nu_{xy}+2, ..., 0(1)$, for even (odd) ν_{xy}; and the translational angular momentum quantum number along the long axis of the C_{70} cage (z-axis) ν_z. States with rotational wavefunctions which are either wholly polarised along the z-axis or the circular xy-plane (ie: ortho-$(0,0,\nu_z)$ states) are denoted with $p = z$ or $p = xy$ respectively, where p is the direction of polarisation of the rotational wavefunction. States in which the rotational wavefunction is neither wholly polarised along the z-axis nor the xy-plane (ie: states other than the ortho-$(0,0,\nu_z)$ states) are not denoted with p. The simulated rotational wavefunctions of the two ortho-(0,0,0) states are illustrated in Figure 5.1.1 [74]. The degeneracy of each $(\nu_{xy}, |l|, \nu_z)$ state is described by $g = 2(J + \nu_{xy}) + 1$. The D_{5h} symmetry of the C_{70} cage results in the degeneracy of the $(\nu_{xy}, |l|, \nu_z)$ states to be lowered to $g = 2$ for the $(0,0,\nu_z,xy)$ states, and $g = 1$ for the $(0,0,\nu_z,z)$ states.

Theoretical energy levels of $H_2@C_{70}$ have been calculated by Xu et al [46] using a similar method to those used to calculate the energy levels of $H_2@C_{60}$. The simulated 5D PES along the z-, x- and y-axes of the C_{70} are illustrated in Figures 5.1.2(a), (b) and (c) respectively [46]. It can be seen that the PES along the z-axis resembles a square well potential, while the PES along the $x-$ and y-axes resembles the potential energy of a harmonic oscillator. The calculated energy levels which are based on this 5D PES are compiled into an energy level diagram shown in Figure 5.1.3. This energy level diagram is used as a reference for the assignments of the INS peaks in the next chapter.

Due to conservation of energy, the weighted mean energy of the ground state rotational energy of H_2 should be equal to the energy of ortho-$H_2@C_{60}$ ground state ($E_{J=1,\nu=0} = 2B_{\nu=0} \approx 14.6$ meV, see Section 3.2), as the rotational constant $B_{\nu=0}$ is a property of H_2 rather than $H_2@C_{60}$. The 13.7 meV weighted mean rotational ground state energy of ortho-$H_2@C_{70}$ in Xu's en-

ergy level diagram (Figure 5.1.3) is calculated using the rotational constant of the first vibrational excited state $B_{\nu=1}$ of H_2. Furthermore, the NMR experiments performed by Mamone et al at the University of Southampton [74] have suggested that the the ground ortho state should be the ortho-$(0,0,\nu_z,xy)$ state, rather than the ortho-$(0,0,\nu_z,z)$ state as calculated by Xu. Nevertheless, Xu's calculated energy levels can still be used as a reference for the analysis of the INS spectra, albeit swapping the energy values between the ortho-$(0,0,\nu_z,z)$ and the ortho-$(0,0,\nu_z,xy)$ states.

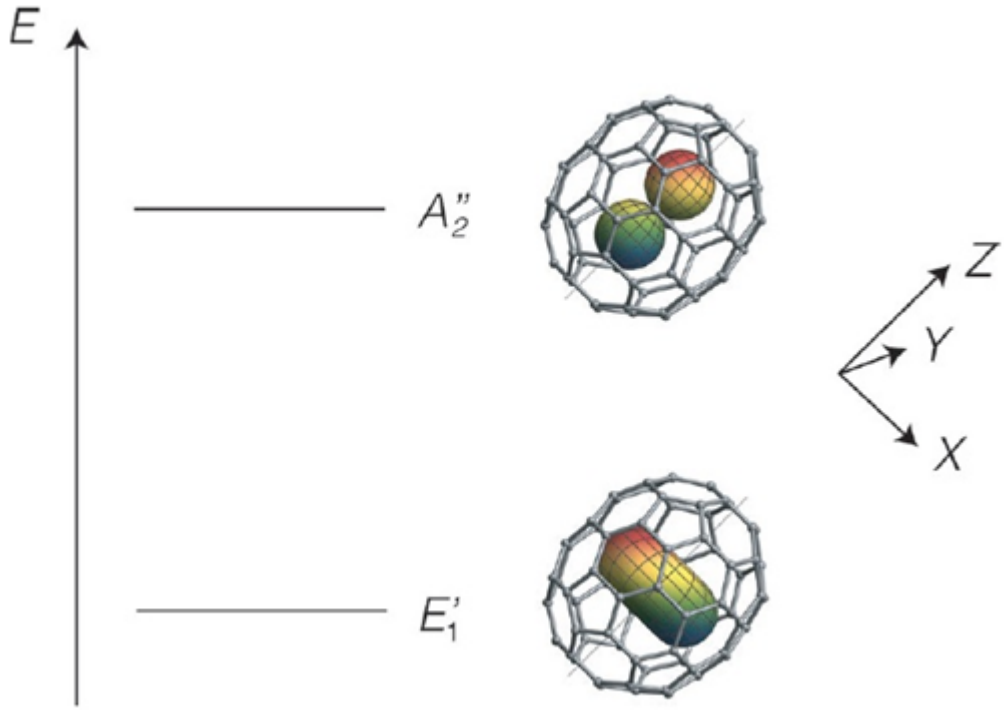

Figure 5.1.1: The wavefunctions of the two lowest ortho-(0,0,0) states as simulated by S. Mamone [74]. The rotational wavefunction that is polarised along the xy-plane is denoted by E'_1, whereas the rotational wavefunction that is polarised along the z-axis is denoted by $A"_2$.

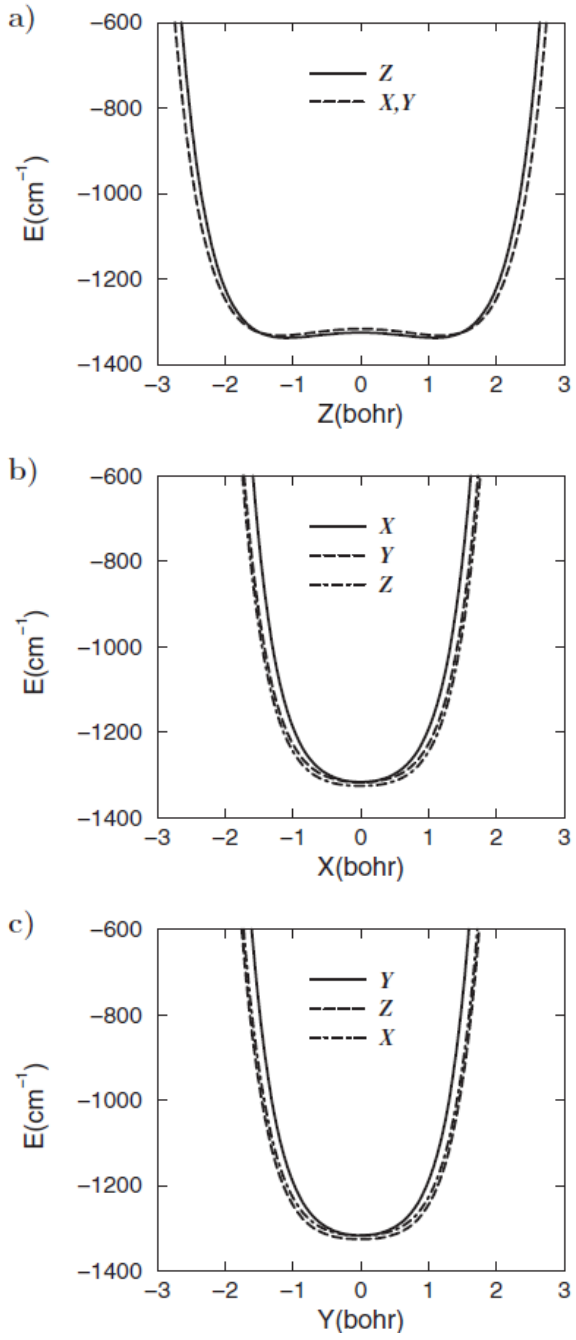

Figure 5.1.2: 5D PES of H_2@C_{70} along the: (a) z-axis, (b) x-axis and (c)y-axis, as simulated by Xu et al [46]. The solid lines are PES of H_2 oriented parallel to the axis, while the dashed and dotted lines are PES of H_2 oriented perpendicular to the axis (as indicated in the legends).

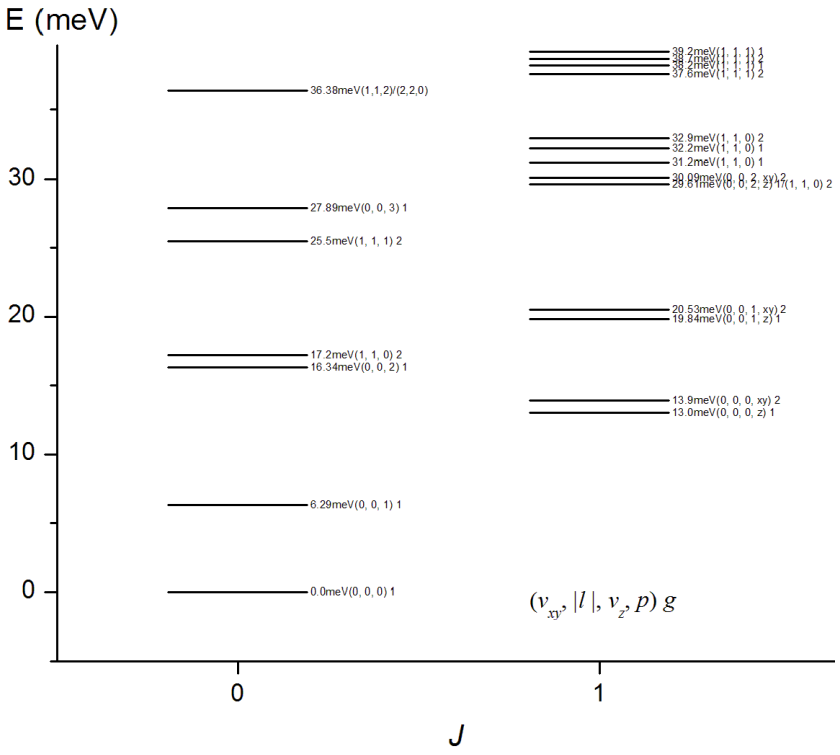

Figure 5.1.3: Energy level diagram of $H_2@C_{70}$ as described by Xu et al in his paper. The (0,0,2,z) state is calculated to be coincidently degenerate with the lowest (1,1,0) state. Only the ortho-(0,0,ν_z) states are denoted with the additional label p as only the rotational wavefunctions of those states are either wholly polarised along the z-axis or the xy-plane.

Chapter 6

INS spectral analysis of $H_2@C_{70}$

The aim of the INS study of the $H_2@C_{70}$ is to study the quantum dynamics of the entrapped H_2 in the ellipsoidal fullerene cage. The INS experiments are performed with the IN4C and IN5 spectrometers at the ILL, Grenoble, and TOFTOF spectrometer at the Heinz Maier-Leibnitz Zentrum, Munich. TOFTOF is a direct geometry multi-chopper time-of-flight spectrometer operated with incident neutrons from the under-moderated cold source of the reactor, which is similar to the IN5 spectrometer [62]. The experiments that were done with IN4C were conducted by my supervisor Anthony J. Horsewill, our collaborator and instrument scientist Stéphane Rols and myself. The experiments that were done with TOFTOF were conducted by our collaborator, Stéphane Rols, on behalf of our group in Nottingham. The IN4C spectrometer is mainly used for the low temperature study of the NE loss transitions, whereas the IN5 and TOFTOF spectrometers are used for the high resolution temperature dependence study of the NE gain transitions. The assignment of the peaks in the $H_2@C_{70}$ are informed by the theoretical energy level diagram of $H_2@C_{70}$ calculated by Xu et al as shown in Figure 5.1.3 [46].

6.1 Low temperature thermal neutron scattering

The aim of the IN4C experiment was to obtain an overview of the energy level structure of the $H_2@C_{70}$, as IN4C probes both NE gain and loss regions of the spectrum. By comparison, IN5 only probes the NE gain region but provides significantly better resolution. The IN4C spectra which were recorded using incident neutron wavelengths of 1.4, 1.6, 2.2 and 2.8 Å respectively at 1.5 K are illustrated in Figure 6.1.1. The shorter incident neutron wavelengths are used to probe the higher energy states, albeit having a lower resolution.

Unlike the IN4C spectra of the $H_2@C_{60}$ sample, there are two peaks in the NE gain part of the $H_2@C_{70}$ IN4C spectra. These two peaks, which are centred at -12.97 and -7.73 meV spectrum respectively correspond to the ortho-(0,0,0,xy) state de-exciting to the para-(0,0,0) and para-(0,0,1) states respectively. The appearance of the -7.73 meV peak conclusively establishes the translational energy associated with the long axis.

The 13.21 meV peak corresponds to the para-(0,0,0) exciting to the ortho-(0,0,0,xy) state, while the 5.47 meV peak corresponds to the ortho-(0,0,0,xy) state exciting to the ortho-(0,0,1,xy) state. The slight discrepancy between the magnitude of the upward and downward transitions of the main rotational line is due to the additional unresolved peak centred at -11.9 meV, which is detected with the high resolution IN5 spectra (see next section). The 5.47 meV peak is assigned to the ortho-(0,0,1,xy) state instead of the ortho-(0,0,0,z) state because the magnitude of the transition is consistent with the energy difference between the para-(0,0,0) and para-(0,0,1) states, which is 5.5 meV. Furthermore, if it were to be the transition to the ortho-(0,0,0,z) state, then it would contradict the expectation that the weighted mean energy of the ortho-(0,0,0) states is equal to the rotational constant (≈14.6 meV). Therefore, the 16.8 meV peak is assigned to the para-(0,0,0) to ortho-(0,0,0,z) transition in order to be consistent with this expectation. The 18.7 meV peak is assigned to the para-(0,0,0) to ortho-(0,0,1,xy) transition as it is consistent with the assignment of the 5.47 meV peak, while the 21.82 meV peak is assigned to the para-(0,0,0) to ortho-(0,0,1,z) as the magnitude of the splitting between the ortho-(0,0,1,xy) and ortho-(0,0,1,z) states is consistent with those of the ortho-(0,0,0) states. There is also a possibility that the 18.7 meV peak is the ortho-(0,0,0,xy) to the ortho-(1,1,0) transition as the energy difference between the two states is close to 18.7 meV. Using the same Gaussian

width as the 21.82 meV peak, three Gaussians (centred at 29.8 meV, 30.84 meV and 32.6 meV respectively) can be fitted to the broad peak that is centred on 31.7 meV. The position of these three Gaussians are consistent with the TR fine structure of the ortho-(1,1,0) states calculated by Xu [46].

The peaks at $\Delta E \leq 5$ meV are concluded to be artefacts as they are not present in the cold neutron scattering spectra recorded with IN5, while the 12 meV peak is later shown in the IN5 analysis to be the transition of the doubly occupied $(H_2)_2@C_{70}$ complexes. The assignment of the higher energy peaks which are centred at 14.52 meV, 25.29 meV and 28 meV respectively are not as straightforward as the lower energy transfer region, because the use of Xu's simulated energy levels as reference for peak assignments does not yield consistent results with the temperature dependence data obtained with IN5 and TOFTOF. As Xu's simulated energy levels do not have ortho states with energies between 21 meV and 29 meV, the straightforward assignment of the 25.29 meV and 28 meV peaks are the transitions from the ortho-(0,0,0,xy) to the higher energy states, as para-(0,0,0) to para-(1,1,1) and para-(0,0,3) transitions are forbidden, while it is possible that the 14.52 meV peak is the ortho-(0,0,0,xy) to para-(0,0,3) transition. However, it is later shown in the temperature dependence cold neutron scattering analysis that there are two ortho states with energies of 25.3 meV and 27.6 meV, which could be coincidentally degenerate with the para-(1,1,1) and para-(0,0,3) states respectively. It is also shown that the NE gain equivalent of the 14.52 meV peak originates from the 27.6 meV ortho-(0,0,2,z) state instead of the para-(0,0,3) state. Therefore, the 14.52 meV, 25.29 meV and 27.6 meV peaks in the IN4C spectra are likely the transitions to the ortho-(0,0,2,z) and ortho-(0,0,2,xy) states.

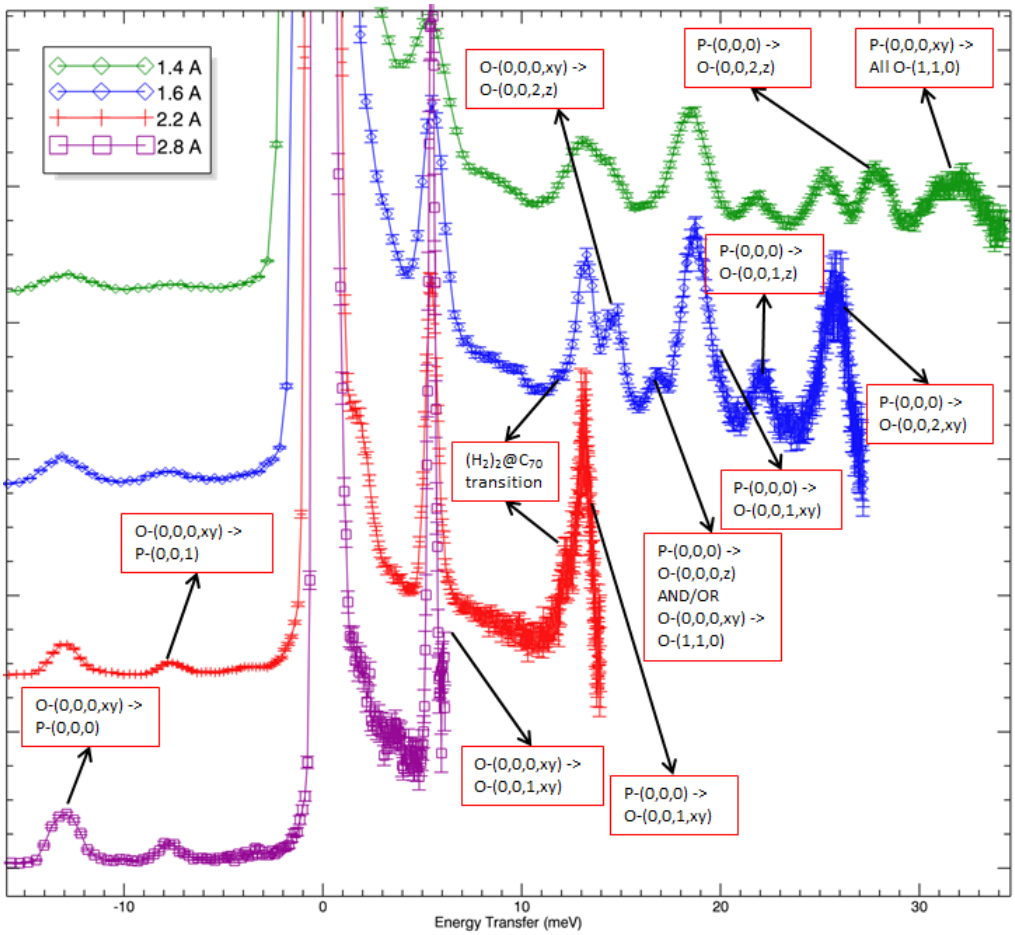

Figure 6.1.1: The INS spectra of $H_2@C_{70}$ recorded with different incident neutron wavelengths at 1.5 K using the IN4C spectrometer. The neutron wavelengths of the respective spectra are shown in the legend. All of the peak assignments apart from the two peaks centred on 25.3 meV and 27.6 meV respectively are solely based on Xu's simulated energy levels. The assignments of the 25.3 meV and 27.6 meV peaks are based on the temperature dependence cold neutron scattering spectra.

6.2 Temperature dependence study using cold neutron scattering

6.2.1 Temperature dependence spectra

The aim of the INS temperature dependence analysis is to determine the origin and degeneracy of the transition by studying the change of the peak amplitude with temperature. The IN5 spectra are recorded at temperatures of up to 200 K, with primary focus on the lower temperature dependence study ($1.5 \leq T \leq 10$ K). Therefore, the higher temperature spectra are recorded with larger temperature steps. All of the IN5 spectra are recorded using 5Å incident neutron wavelength. The -12.97 meV peak observed in the IN4C spectra can be observed with higher resolution in the 1.5 K IN5 spectrum shown in Figure 6.2.1. The -12.97 meV peak seen in the IN4C spectra is shown to consist of two peaks, a major -13.36 meV peak and a minor -11.9 meV peak. The amplitude of the -11.9 meV peak is measured to be $\approx$ 8.2% the size of the -13.36 meV peak and $\approx$ 7.5% of the sum of both peak amplitudes. As there are approximately 3% of the $H_2@C_{70}$ sample being the doubly occupied $(H_2)_2@C_{70}$ molecular complex [4], the amplitude of the peak that corresponds to the $(H_2)_2@C_{70}$ complexes should be $\approx$ 6% of the sum of the peaks that originate from both variants. This is because the doubly occupied molecule has twice the number of protons than its singly occupied counterpart. Hence, it can be concluded that the minor peak corresponds to the INS of the $(H_2)_2@C_{70}$ complexes. As the sample is recorded at 1.5 K where all of the molecules are expected to be in their ground state, it is likely that the minor peak corresponds to the ground state of ortho-H_2 or ortho-$(H_2)_2$ of the doubly occupied molecular complex de-exciting to the lower energy para ground state.

The IN5 spectra which are recorded using 5Å incident neutron wavelength at temperatures of 1.5 K, 10 K, 50 K, 100 K, 150 K and 200 K are illustrated in Figures 6.2.2. Unlike the $H_2@C_{60}$ spectra, there are no definite rotational or translational regions in the spectra due to having larger number of non-degenerate states which results in lower transition energies between states. This is evident from the cluster of peaks that appears in the $-5 < \Delta E < 0$ meV energy transfer region at higher temperatures which corresponds to the low energy transitions to the immediate lower energy states. It can be seen that the amplitude of the -5.5 meV peak increases rapidly as temperature is increased from 1.5 K to 50 K, while there is a large number of peaks that appear in the energy transfer region between the -5.5 meV peak

and the -18.6 meV peak at higher temperatures.

The TOFTOF spectra are recorded using 8 Å incident neutron wavelength at temperatures ranging between 1.5 K and 200 K. Figure 6.2.3 illustrates examples of a few TOFTOF spectra recorded at various temperatures. Besides having identical peaks as those seen in Figure 6.2.2, it can be seen that the TOFTOF spectra have lower signal-to-noise ratio (SNR) than the IN5 spectra due to having lower neutron flux. Despite using longer incident neutron wavelength, the resolution of the TOFTOF spectra isn't any better than the IN5 spectra. However, the background of the TOFTOF spectra at higher temperatures are observed to be lower than the IN5 counterpart. Furthermore, the TOFTOF spectra are recorded with smaller temperature steps than the IN5 spectra. Therefore, the TOFTOF spectra are more suitable for the temperature dependence analysis in the energy transfer region of $-20 < \Delta E < -5$ meV despite having lower signal SNR, because the IN5 spectra have high background gradient in this energy transfer region, which increases the ambiguity of the Gaussian fits. Additionally, the smaller temperature steps employed by the TOFTOF experiment at higher temperatures also result in better peak amplitudes as a function of temperature data.

The peaks in the $\Delta E \leq -17.5$ meV energy transfer region of the TOFTOF spectra have SNR which are too low for analysis. Hence, the temperature dependence analysis of the peaks in this energy transfer region are done with the IN5 spectra, as the SNR of the IN5 spectra is relatively high in this energy transfer region, while the background gradient in this energy transfer region is low enough to obtain good Gaussian fits. Additionally, the temperature dependence analysis of the minor peak centred at -11 meV is also done using the IN5 spectra, as the peak is unobservable in the TOFTOF spectra due to its lower SNR.

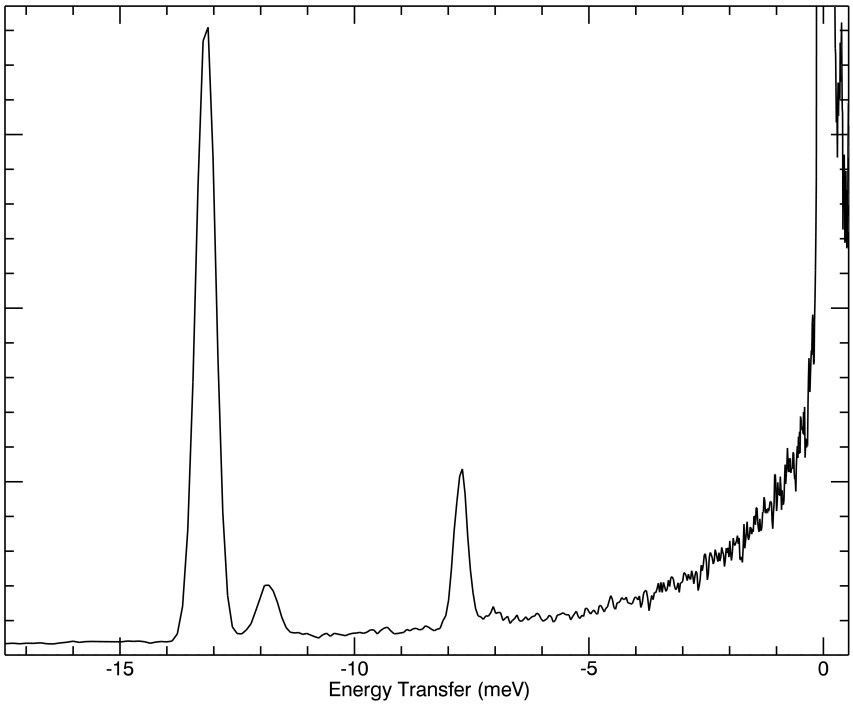

Figure 6.2.1: INS spectrum of the $H_2@C_{70}$ recorded with 5Å incident neutron wavelengths at temperatures of 1.5 K using the IN5 spectrometer. The major -13.36 meV peak corresponds to the ortho ground state to para ground state transition; minor -11.9 meV peak corresponds to INS of the doubly occupied $(H_2)_2@C_{70}$ molecular complex; and the -7.7 meV peak corresponds to the ortho ground state de-exciting to first excited para state.

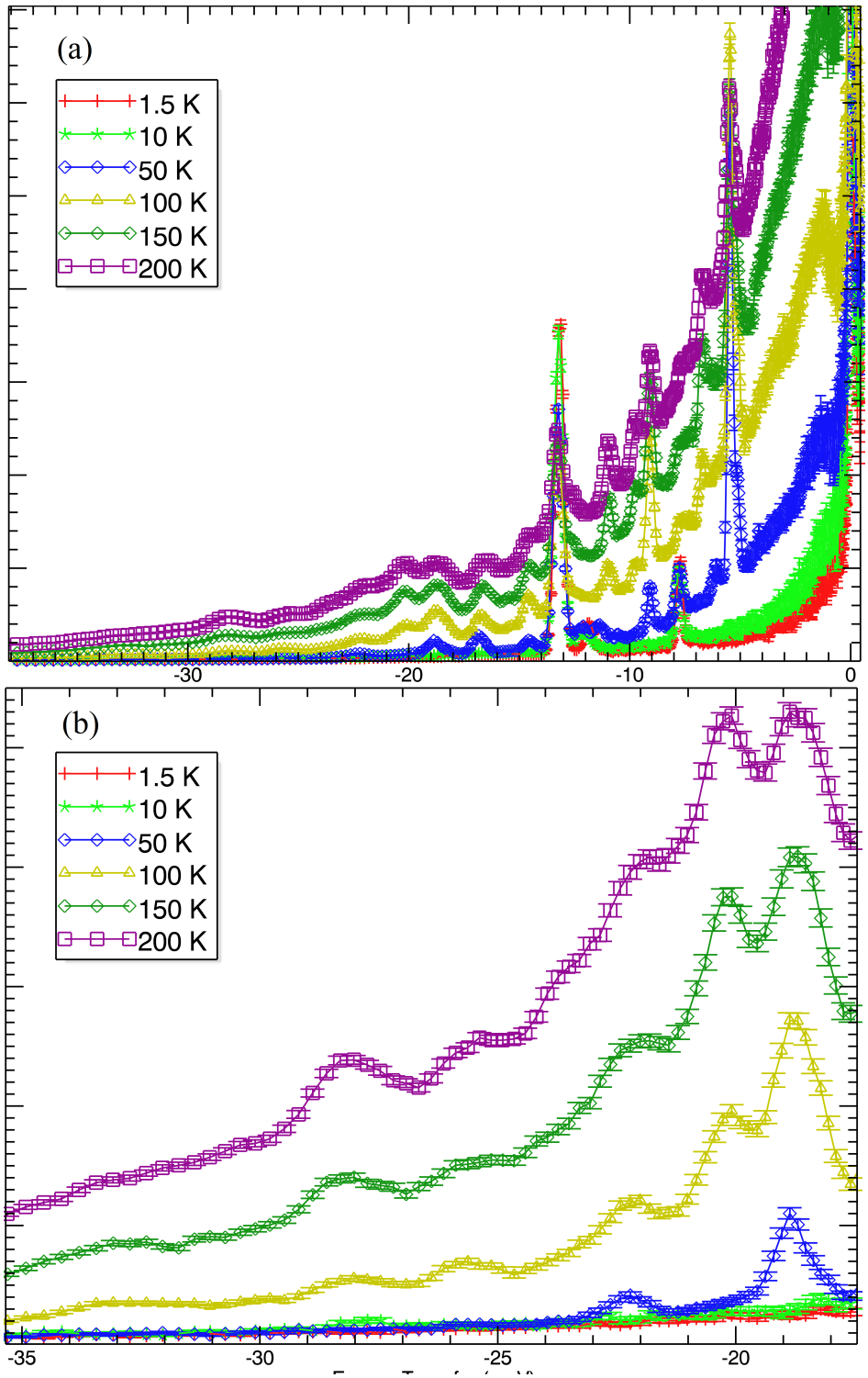

Figure 6.2.2: INS spectra of $H_2@C_{70}$ recorded with 5Å incident neutron wavelength using the IN5 spectrometer. The recorded temperatures are displayed in the legend. Figure (b) is the blown-up version of Figure (a) to illustrate the $-35 \leq \Delta E \leq -17.5$ meV energy transfer region of the spectra, which is used for the temperature dependence analysis.

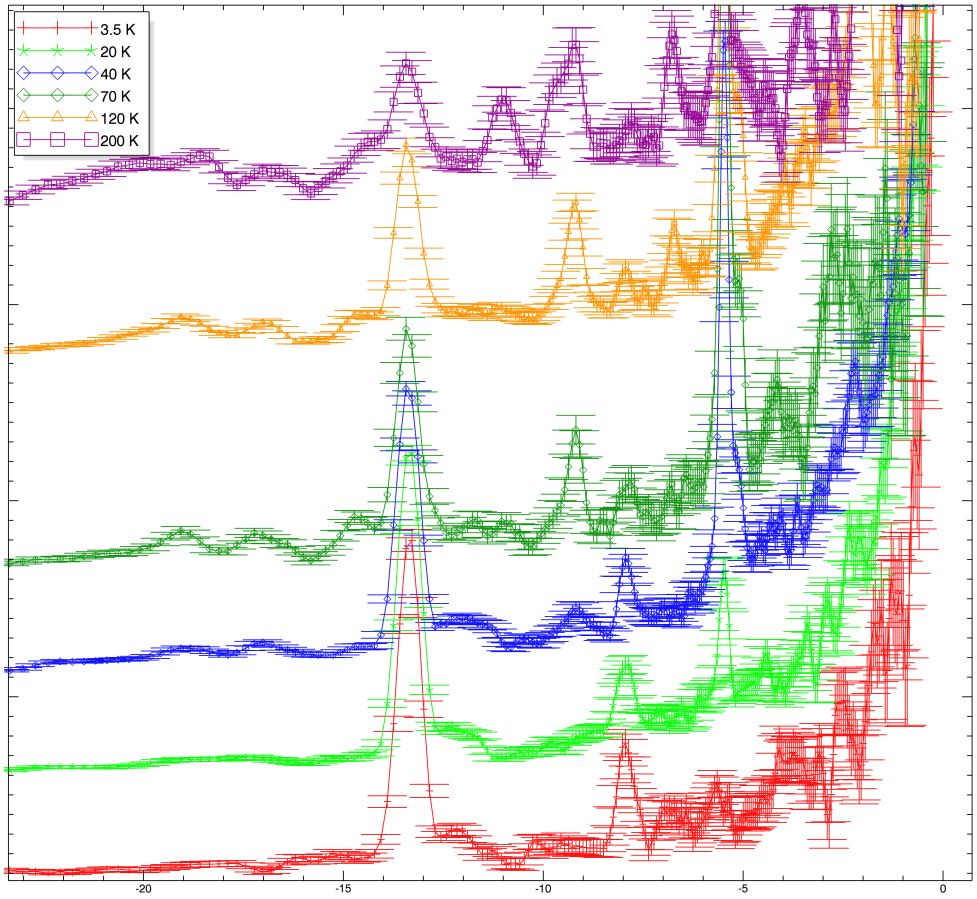

Figure 6.2.3: INS spectra of $H_2@C_{70}$ recorded with 8Å incident neutron wavelength using the TOFTOF spectrometer. The recorded temperatures are displayed in the legend. The peaks in these spectra are identical to those seen in the IN5 spectra (see Figure 6.2.2). The SNR and background of the TOFTOF spectra is lower than those of the IN5 spectra.

6.2.2 Gaussian fit

The INS peaks within the energy transfer region of $-35 \leq \Delta E \leq -5$ meV are fitted with individual Guassian peaks to determine their respective peak amplitudes. The fitting of this energy transfer region is divided into a 4 smaller fitting regions so that the background can be approximated as linear. The fitting regions are: $-35 \leq \Delta E \leq -27$ meV and $-27 \leq \Delta E \leq -17.5$ meV of the IN5 spectra; $-17.5 \leq \Delta E \leq -10$ meV and $-10 \leq \Delta E \leq -5$ meV of the TOFTOF spectra.

The fitting procedure is slightly different to the one used in the $H_2@C_{60}$ temperature dependence INS analysis because the peaks in the $H_2@C_{70}$ spectra are not as clustered as those in the $H_2@C_{60}$ spectra. Hence, there is hardly a need to combine multiple peaks into a single combined Gaussian. The position and width of the Gaussian peaks from the lower energy states are determined from the fit of the lower temperature spectra where there are lower number of peaks. The determined position and width of the Gaussian peaks are then fixed in the fit of the next higher temperature spectrum. A necessary number of Gaussians with widths which are consistent with the fixed Gaussians is also added to obtain the best fit of the spectra within the fitting region. If the position of the added Gaussians are too close to the fixed Gaussians, the width of the respective fixed Gaussians are widened instead to represent the additional transitions. The position and width of all the Gaussian peaks that are used in the fit are then "carried forward" to the fit of the next higher temperature spectrum to repeat the fitting process. This process is repeated until all of the higher temperature spectra are fitted. This fitting procedure is applied to the 4 aforementioned fitting regions of all the spectra. An example of the fit in the the $-27 \leq \Delta E \leq -17.5$ meV fitting region of the IN5 spectra is shown in Figure 6.2.4.

There is a total of 19 Gaussian peaks (excluding the doubly occupied peak at 11.9 meV) that are used to fit the $-35 \leq \Delta E \leq -5$ meV energy transfer region of the IN5 and TOFTOF spectra. The amplitude of the Gaussian peaks are recorded and compiled into their respective amplitude as a function of temperature plots shown in Figures 6.2.6 (TOFTOF) and 6.2.7 (IN5).

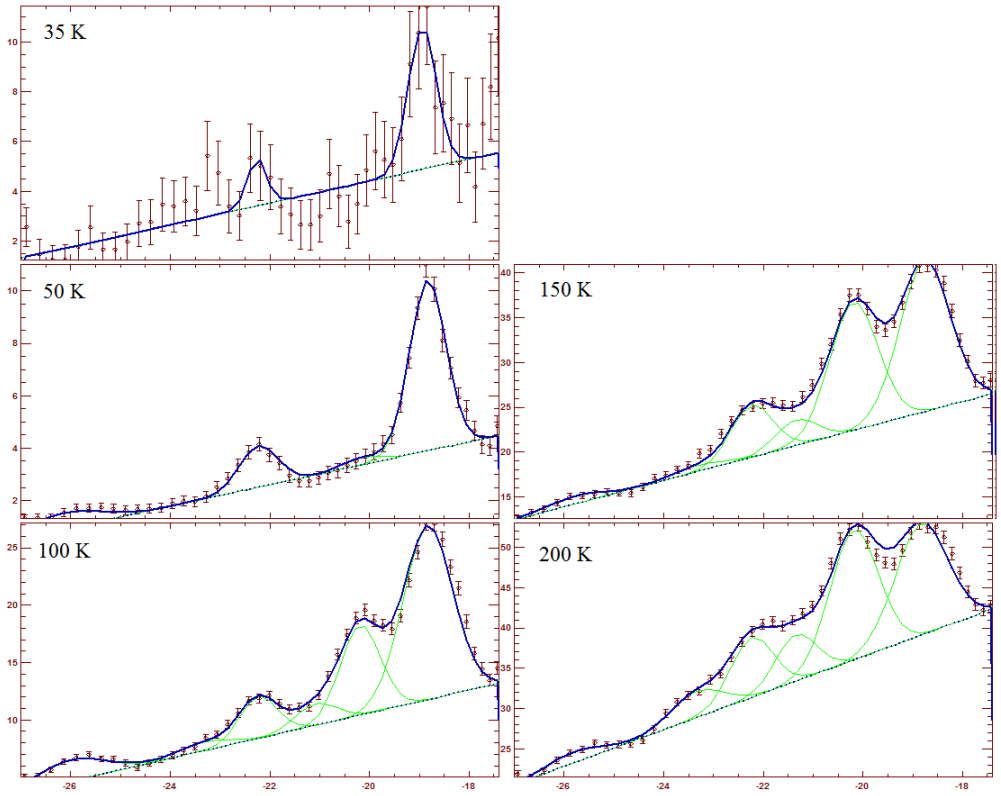

Figure 6.2.4: Fitting of the $-27 \leq \Delta E \leq -17.5$ meV energy transfer region of the IN5 spectra recorded at temperatures of 35 K, 50 K, 100 K, 150 K and 200 K. See text for details on the fitting procedure.

6.2.3 Analysis of the amplitude as a function of temperature plots

The fitting of the amplitude as a function of temperature plots are done using the Boltzmann equation (Equation 4.2.1) with the modified partition function (Equation 4.2.4). The q_p and q_o states are chosen to be the para-(111) state and the ortho-(111) state respectively, as both states begin to populate at around the same temperature (40 K). Starting with the energy levels determined from the IN4C analysis to obtain the initial Boltzmann equation and partition function, the following procedure is applied to determine the energy levels: (1) The energy values of the initial states of the transitions which are assigned to the peak is applied to the Boltzmann equation. (2) If there are no possible transitions within the energy level diagram that satisfies the energy transfer values or fits well to the temperature dependence plot of the unassigned peak, the energy values of the states which are not determined from the IN4C analysis are then altered to satisfy the energy transfer values or the fit of the temperature dependence plot of the unassigned peak. (3) The energy values of the remaining undetermined states are altered to obtain a better Boltzmann fit for the temperature dependence data of the determined peaks. (4) Check the altered energy states to see if they contradicts the IN4C, IN5 or TOFTOF spectra. (5) Swap the degeneracies of the states which have been split due to symmetry breaking to see if it results in a better fit to the temperature dependence data.

In order to obtain the best fit to all the amplitude as a function of temperature plots, the energy of the ortho-(0,0,2,xy) and ortho-(0,0,2,z) states have to be lowered to 25.3 meV and 27.6 meV respectively. These changes to the energy levels are also required to explain: (a) the temperature dependence plot of the -9.05 meV and -9.76 meV Gaussian amplitudes, which is assigned to the ortho-(0,0,2,xy) to ortho-(0,0,0,z) and ortho-(0,0,2,z) to ortho-(0,0,0,z) transitions respectively. This is because the other possibility, which is the para-(1,1,1) to ortho-(0,0,0,xy) transition, requires higher temperature to occur as the para-(1,1,1) state is not populated at $T < 45$ K, while the -9.05 meV Gaussian begins to populate at 20 K. (b) The -14.6 meV Gaussian emerges at too low of a temperature for it to be the para-(0,0,3) to ortho-(0,0,0,z) transition. Therefore, this Gaussian is assigned to the ortho-(0,0,2,z) to ortho-(0,0,0,z) transition instead.

The ortho-(1,1,1) band to para-(0,0,0) is observed as two separate bands that are centred at 38.7 meV and 39.6 meV respectively. The 38.7 meV band is observed from the -6.73 meV, -10.97 meV, -20.15 meV and -22.23 meV

Gaussians, which represents the transitions from 38.7 meV ortho-(1,1,1) to 32.6 meV ortho-(1,1,0), 27.6 meV ortho-(0,0,2,z), 18.7 meV ortho-(0,0,1,xy) and 16.8 meV ortho-(0,0,0,z) respectively. Whereas the 39.6 meV band is observed from the -11.09 meV and.-21.04 meV Gaussians, which represents the transitions from the 39.6 meV ortho-(1,1,1) to ortho-(0,0,2,z) and ortho-(0,0,1,xy) respectively. The -23.3 meV Gaussian is concluded to originate from the state which has higher energy than the ortho-(1,1,1) and para-(1,1,2) states. Besides the -23.3 meV Gaussian, all of the observed NE gain Gaussians originate from states with $E < 40$ meV.

The position of the NE gain Gaussians and the transitions they represent are compiled together with the those of the IN4C spectra into Table 6.1. The energy levels shown in this table are then compiled into the energy level diagram shown in Figure 6.2.5. The energy levels which are denoted with asterisks are the unobserved energy levels that have energy values which are based on Xu's simulated energy levels. It is worth noting that the energy levels which are denoted with asterisks are theoretical estimates and are not conclusive. It can be seen that the (0,0,ν_z) states have larger splitting than those in Xu's energy level diagram (Figure 5.1.3). This suggests that the rotational anisotropy is higher than those calculated by Xu et al. The translations along the z-axis are observed to be smaller than those calculated by Xu et al, while the translations along the xy- plane are observed to be consistent with Xu's calculation.

The Boltzmann fits of the temperature dependence data in Figures 6.2.6 and 6.2.7 are based on the energy of the initial state of the respective peaks as shown in Table 6.1, while the modified partition function used for the fits is based on the energy level diagram shown in Figure 6.2.5.

Gaussian peak position (meV)	Initial State	Energy (meV)	Final State	Energy (meV)	Instrument
-33.08	O-(1,1,0)	32.6	P-(0,0,0)	0	**(IN5)**
-28	O-(0,0,2,z)	27.6	P-(0,0,0)	0	**(IN5)**
	O-(1,1,0)	32.6	P-(0,0,1)	5.5	
-25.96	O-(0,0,2,xy)	25.3	P-(0,0,0)	0	**(IN5)**
-23.3	Higher energy state		-		**(IN5)**
-22.23	O-(0,0,1,z)	21.82	P-(0,0,0)	0	**(IN5)**
	O-(1,1,1)	38.7	O-(0,0,0,z)	16.8	
-21.04	O-(1,1,1)	39.6	O-(0,0,1,xy)	18.7	**(IN5)**
-20.15	O-(1,1,1)	38.7	O-(0,0,1,xy)	18.7	**(IN5)**
-18.78	O-(0,0,1,xy)	18.7	P-(0,0,0)	0	**(IN5)**
	O-(1,1,0)	32.6	O-(0,0,0,xy)	13.2	
-16.8	O-(0,0,0,z)	16.8	P-(0,0,0)	0	**(TOFTOF)**
	O-(1,1,1)	38.7	O-(0,0,1,z)	21.82	
-14.6	O-(0,0,2,z)	27.6	O-(0,0,0,xy)	13.2	**(TOFTOF)**
-13.36	O-(0,0,0,xy)	13.2	P-(0,0,0)	0	**(TOFTOF)**
	O-(0,0,1,xy)	18.7	P-(0,0,1)	5.5	
	O-(1,1,0)	29.8	O-(0,0,0,z)	16.8	
	O-(1,1,1)	38.7	O-(0,0,2,xy)	25.3	
-11.09	O-(1,1,1)	39.6	O-(0,0,2,z)	27.6	**(TOFTOF)**
-10.97	O-(1,1,1)	38.7	O-(0,0,2,z)	27.6	**(IN5)**
	O-(1,1,1)	38.7	P-(0,0,3)	27.9	
-9.76	O-(1,1,0)	31.62	O-(0,0,1,z)	21.82	**(TOFTOF)**
-9.05	O-(0,0,2,xy)	25.3	O-(0,0,0,z)	16.8	**(TOFTOF)**
-7.95	O-(0,0,0,xy)	13.2	P-(0,0,1)	5.5	**(TOFTOF)**
-6.73	O-(1,1,1)	38.7	O-(1,1,0)	32.6	**(TOFTOF)**
-5.5	O-(0,0,0,z)	16.8	O-(0,0,0,xy)	13.2	**(TOFTOF)**
-5.07	O-(0,0,1,z)	21.82	O-(0,0,0,z)	16.8	**(TOFTOF)**
5.47	O-(0,0,0,xy)	13.2	O-(0,0,0,z)	16.8	**(IN4)**
13.21	P-(0,0,0)	0	O-(0,0,0,xy)	13.2	**(IN4)**
14.524	O-(0,0,0,xy)	13.2	O-(0,0,2,z)	27.6	**(IN4)**
16.8	P-(0,0,0)	0	O-(0,0,0,z)	16.8	**(IN4)**
18.513	P-(0,0,0)	0	O-(0,0,1,xy)	18.7	**(IN4)**
21.82	P-(0,0,0)	0	O-(0,0,1,z)	21.82	**(IN4)**
25.29	P-(0,0,0)	0	O-(0,0,2,xy)	25.3	**(IN4)**
28	P-(0,0,0)	0	O-(0,0,2,z)	27.6	**(IN4)**
30.84	P-(0,0,0)	0	O-(1,1,0)	30.84	**(IN4)**
32.6	P-(0,0,0)	0	O-(1,1,0)	32.6	**(IN4)**

Table 6.1: Compilation of the positions and the assigned transitions of all the INS peaks observed in the IN4C, IN5 and TOFTOF spectra of the $H_2@C_{70}$ sample.

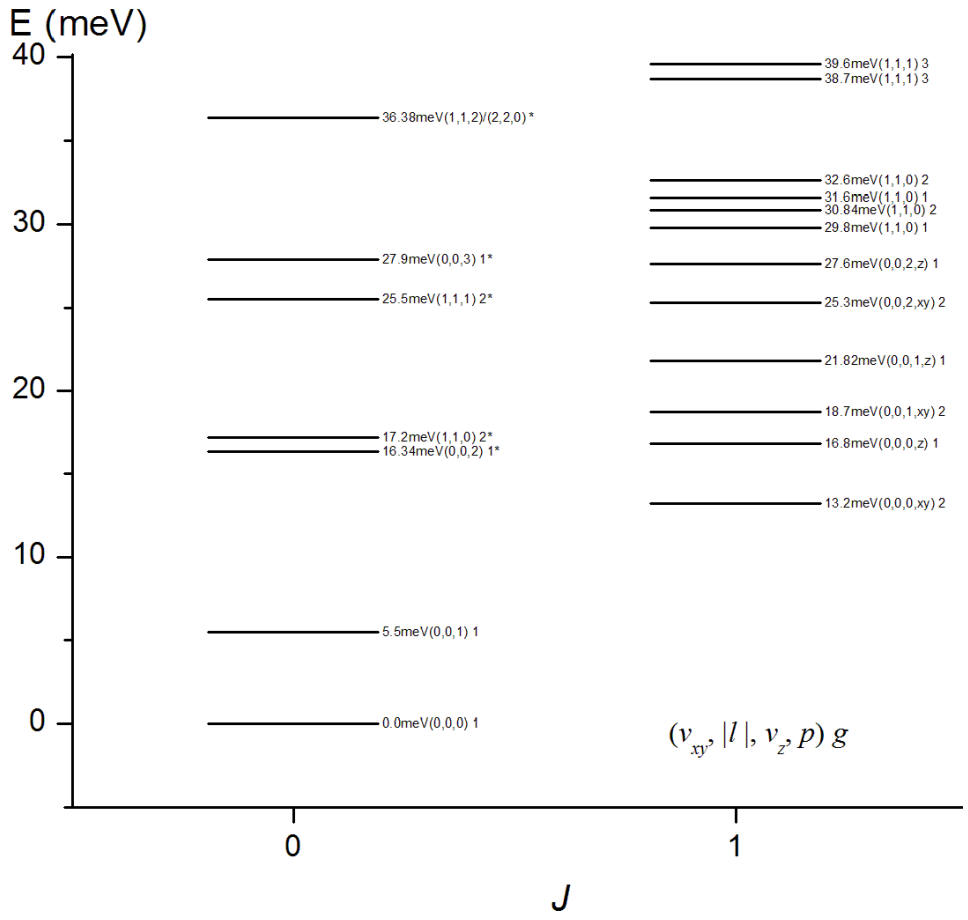

Figure 6.2.5: The deduced energy level diagram of $H_2@C_{70}$ that is based on the analysis of the IN4C, IN5 and TOFTOF spectra, except the unobserved energy levels that are denoted by asterisks, which have energy values which are based on Xu's simulated energy levels.

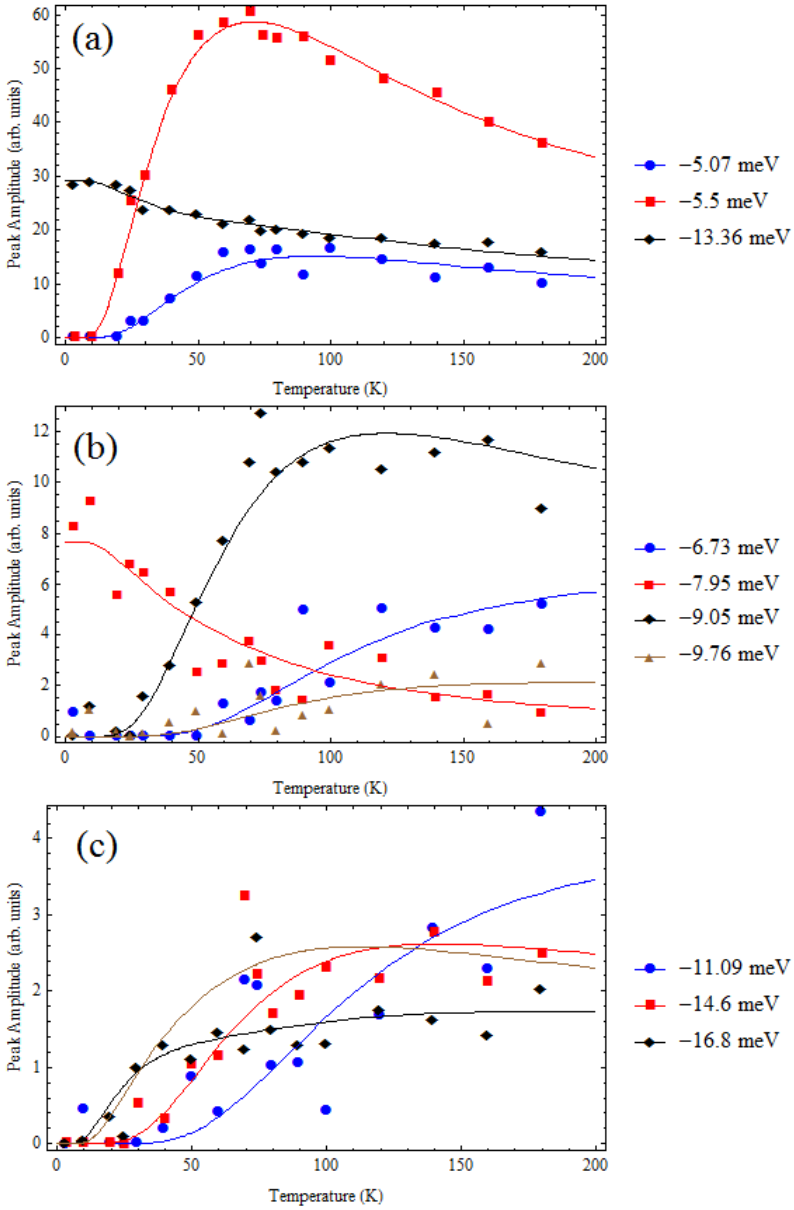

Figure 6.2.6: Amplitude as a function of temperature plots of the peaks observed in the $-17.5 \leq \Delta E \leq -5$ meV energy transfer region of the TOFTOF spectra of $H_2@C_{70}$. The data is fitted with the Boltzmann equation that is based on the energy of the initial state of the respective peaks as shown in Table 6.1, while the modified partition function is based on the energy level diagram shown in Figure 6.2.5.

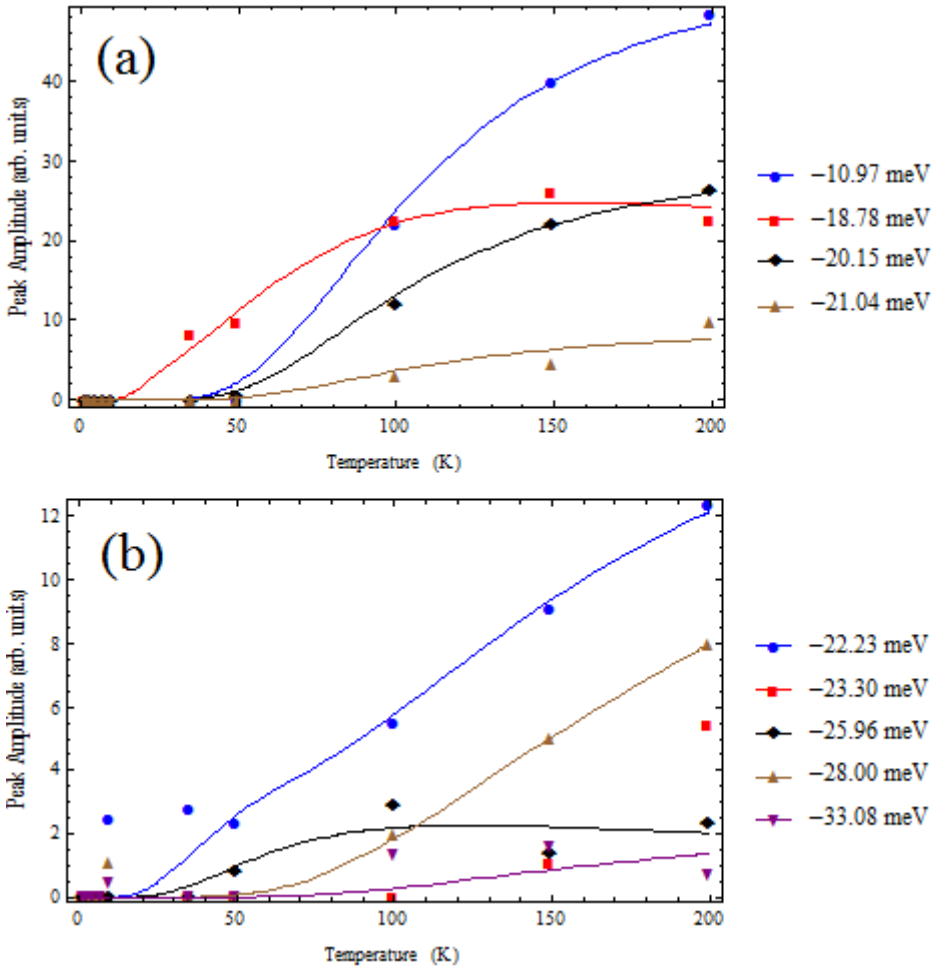

Figure 6.2.7: Amplitude as a function of temperature plots of the peaks observed in the $-35 \leq \Delta E \leq -17.5$ meV energy transfer region of the IN5 spectra of $H_2@C_{70}$. The data is fitted with the Boltzmann equation that is based on the energy of the initial state of the respective peaks as shown in Table 6.1, while the modified partition function is based on the energy level diagram shown in Figure 6.2.5.

6.3 Conclusion

The INS study of the $H_2@C_{70}$ has resulted in the experimentally deduced energy level diagram of $H_2@C_{70}$ (Figure 6.2.5). This energy level diagram provide insights on the effect of an elongated axis of the C_{70} cage, with respect to the C_{60} cage, on the entrapped H_2. The comparison between the energy level diagrams of the $H_2@C_{60}$ and $H_2@C_{70}$ molecules has shown that the elongated axis of the C_{70} cage results in the splitting of the translational and rotational states. The energy of the first translational ortho state of the $H_2@C_{70}$ (≈ 39 meV) is observed to be similar to the first translational ortho state of $H_2@C_{60}$ because the diameter of the xy-plane of the C_{70} is similar to the diameter of the C_{60}. Unlike the $H_2@C_{60}$, no rotational fine structure is observed in the INS spectra of $H_2@C_{70}$.

The INS analysis of the $H_2@C_{70}$ have shown that the energy difference between the rotational wavefunction that is polarised along the long z-axis and the rotational wavefunction that is polarised along the long xy-plane is larger than those calculated by Xu et al [46]. The weighted mean energy of ortho-(0,0,0) state is calculated to be 14.4 meV, which is consistent with the observed rotational constant of $H_2@C_{60}$. The size of the observed splitting of the ortho-(0,0,1) and ortho-(0,0,2) states are consistent with the splitting of the ortho-(0,0,0) state.

The ortho-(0,0,2,xy) and ortho-(0,0,2,z) states are also shown to be lower than those calculated by Xu et al and may be coincidently degenerate with the para-(1,1,1) and para-(0,0,3) states respectively if the energy values of the two para states are as calculated by Xu et al. However, there is no clear evidence that those two para states are observed in the spectra, as they may be masked by the two coincidently degenerate ortho states. Furthermore, the temperature dependence data of the NE gain peaks have shown that the peaks which are assigned to the -27.6 meV and -25.3 meV energy states only consist of transitions which originate from those two ortho states. Therefore, it can be concluded that either the para-(1,1,1) and para-(0,0,3) states have energy values which are different to those calculated by Xu et al, or the transitions from those two para states to the lower energy ortho-states are forbidden. Besides the aforementioned differences, the observed higher translational ortho-states, namely the ortho-(1,1,0) and ortho-(1,1,1) states, are consistent with Xu's simulated energy levels.

The determination of the lower energy states of the $H_2@C_{70}$ has allowed us to understand the fundamental dynamics of the entrapped molecule, which is essential for analysing the higher energy INS spectra of the

sample recorded with the IN1-Lagrange spectrometer. More importantly, the overall study of the $H_2@C_{70}$ could provide insights on the dynamics of other similar molecular complexes which have a molecule entrapped in a less symmetric potential, such as the H_2O entrapped in a geometrically distorted C_{60} cage, which is discussed in the next chapter.

Part IV

$H_2O@C_{60}$

Chapter 7

Theory and properties of $H_2O@C_{60}$

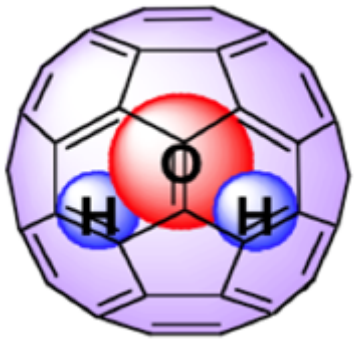

Figure 7.0.1: Schematic of the $H_2O@C_{60}$ supramolecular complex.

The encapsulation of a water molecule inside a C_{60} cage provides a unique opportunity to study H_2O in a highly symmetric and isolated environment. Like the H_2 molecule counterpart, the water molecule exhibits spin isomerism, having both ortho and para species (ortho-H_2O and para-H_2O) [64, 65, 66, 67, 68, 69, 70, 71, 72]. Unlike the H_2 molecule, H_2O possess a permanent electric dipole moment and a lower rotational symmetry [73]. The lower rotational symmetry is reflected in the otherwise degenerate rotational level in the H_2 molecule (see Figure 7.1.2).

Another striking feature of the $H_2O@C_{60}$ which is not observed in the H_2 endohedral fullerenes is the presence of meta stable ortho-H_2O (ortho to para conversion) at cryogenic temperatures in the absence of catalysts. The nuclear spin-isomer conversion of the ground state ortho-H_2O to the ground state para-H_2O is observable via the decay of the signal originating from ortho-H_2O and the growth of the signal originating from para-H_2O.

The $H_2O@C_{60}$ is synthesised using a similar method (molecular sur-

gery) as the one used to synthesise the $H_2@C_{60}$ [5, 6]. The sample is normally in the form of a black powder which is stable under a wide range of physical conditions and is very convenient to handle. $H_2O@C_{60}$ samples of different filling factors are prepared to study the interactions between neighbouring entrapped H_2O. The sample with 90% filling factor (with the remaining 10% being empty C_{60} cages) is synthesised by our collaborators at Columbia University and has been rigorously sublimed by Mark Denning at the University of Southampton to remove the impurities, while the samples with lower filling factors, namely the 50% and 20% filled samples, are synthesised and rigorously sublimed by A. Krachmalnicoff at the University of Southampton.

Similar to the spectroscopic measurements of the $H_2@C_{60}$, three complementary spectroscopic methods: INS, FIR and NMR are used to study the $H_2O@C_{60}$. The advantages of the three aforementioned spectroscopies in the study of the $H_2O@C_{60}$ are identical to those mentioned in Chapter 3. As with the $H_2@C_{60}$, the entrapped H_2O are relatively isolated from one another, thus resulting in relatively narrow lineshapes being observed in the spectra.

Preliminary spectroscopic studies of $H_2O@C_{60}$ have been performed by the worldwide collaboration of the groups in University of Nottingham, University of Southampton and National Institute of Chemical Physics and Biophysics in Estonia using INS, MAS NMR and FIR respectively [75]. However, the early studies were conducted on a relatively impure sample, leading to broader lineshapes that masked important details in the spectrum. Furthermore, only low energy incident neutrons were used in this preliminary INS investigation. Hence, we began a new investigation on a highly purified 90% filled sample using both higher and lower energy incident neutrons. Only the 90% filled sample has been investigated using INS as the yields of the 50% and 20% filled samples are not high enough for INS investigation. Therefore, NMR investigations were performed on the 50% and 20% filled samples instead to study the inter-fullerene interactions.

The experimental analysis of the $H_2O@C_{60}$ molecule is divided into three chapters: the INS spectral analysis chapter, the NMR spectral analysis chapter (Chapter 9) and the low temperature nuclear spin-isomer conversion analysis chapter (Chapter 10).

7.1 Rotational dynamics of H_2O

The H_2O is an asymmetric top quantum rotor that is characterised by the rotations about the a, b, and c molecular fixed frame axes with their respective subscript labelled moment of inertia being defined as $I_a < I_b < I_c$. The rotational constants about the respective principle axes are defined as $A = \hbar^2/2I_a$, $B = \hbar^2/2I_b$ and $C = \hbar^2/2I_c$. The graphical illustration of the principal axes relative to the molecular frame is shown in Figure 7.1.1(a).

There are two classes of molecular rotation for H_2O, the prolate and oblate rotations [63]. The prolate rotation involves rotation about the major axis of the molecular fixed frame, which is the a-axis (see Figure 7.1.1(a)); while the oblate rotation involve rotation the minor axis of the molecular fixed frame, which is the b-axis. The ground state rotation of ortho-H_2O is about the a-axis (prolate), as the H_2O rotation about the a-axis has the lowest moment of inertia.

Unlike the case of $H_2@C_{60}$, no theoretical model for the $H_2O@C_{60}$ system have been calculated. Therefore, the theoretical gaseous water model calculated by P. Helminger and F. C. Delucia [76], which assumes non-interacting H_2O molecules in free space, is instead used as a basis to understand the quantum rotation of H_2O. The translational dynamics of the entrapped H_2O orbiting within the C_{60} cage is not taken into account in this model.

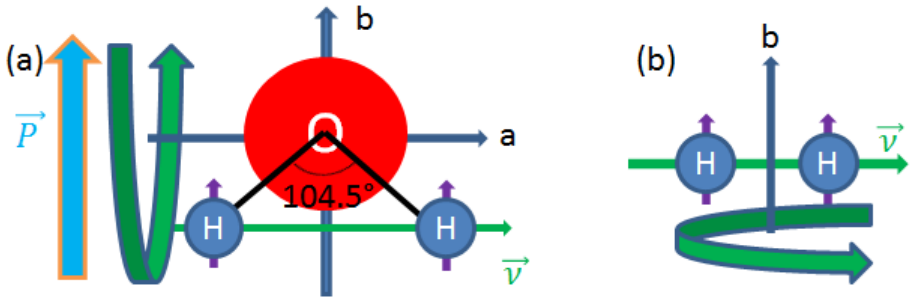

Figure 7.1.1: (a) The ground state rotation planes of ortho-H_2O (around the a-axis, prolate). (b) The ground state rotation planes of ortho-H_2 (around the b-axis). (a and b) It can be seen that the vector connecting the two protons in H_2O ($\vec{\nu}$) is orthogonal to the rotation plane, whereas this vector is parallel to the rotation plane in the case of H_2. It can also be seen that the rotation of the ground state ortho-H_2O results in the effective electric dipole moment being averaged to zero, as the electric dipole moment rotates with the ortho-H_2O molecule along the molecular rotation plane.

7.1.1 Gaseous H_2O model

The energy level diagram of the theoretical gaseous water model is illustrated in Figure 7.1.2 with each energy level represented by the quantum numbers $J_{K_aK_c}$, where J is the quantum number for the total angular momentum, K_a and K_c are the quantum numbers for the angular momentum in the corresponding prolate and oblate symmetric tops. The degeneracy of each state is determined by $g = (2J + 1)$. The para-H_2O (total spin $I = 0$) and the ortho-H_2O (total spin $I = 1$) each have even and odd parity respectively for $K_a + K_c$ in the vibrational ground state due to Pauli Exclusion principle.

The larger number of non-degenerate states in the energy level diagram of gaseous H_2O relative to the energy level diagram of $H_2@C_{60}$ is attributed to the lower symmetry of the H_2O molecule as compared to the H_2 molecule. Even though the theoretical gaseous water model does not include the translational modes of the entrapped H_2O in the C_{60} cage, it remains a good basis for identifying the lower energy rotational states of $H_2O@C_{60}$ which are also in the translational ground state.

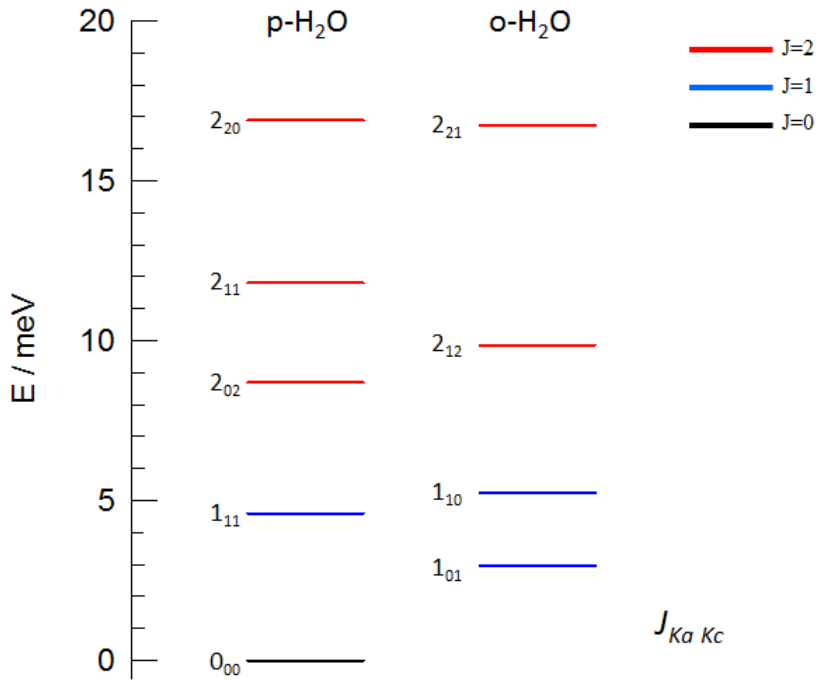

Figure 7.1.2: Energy level diagram of gaseous H_2O as calculated by P. Helminger and F. C. Delucia [76].

7.2 Effective electric dipole and quadrupole moments of $H_2O@C_{60}$

The effective electric dipole moment of the $H_2O@C_{60}$ complex has been calculated to be less than the electric dipole moment of the encapsulated H_2O using various computational methods that does not take into account quantum rotations [80, 81, 82, 83], as the simulations have shown that the electric dipole moment of the entrapped H_2O induces an electric dipole moment with opposing polarity onto the C_{60} cage. These various computational methods have calculated the electric dipole moment P_w of the entrapped H_2O to be $1.93 \leq P_w \leq 2.09$ D, the induced electric dipole moment P_i of the C_{60} cage to be $1.47 \leq P_i \leq 1.7$ D, and the effective electric dipole moment P_e of the $H_2O@C_{60}$ complex to be $0.4 \leq P_e \leq 0.62$ D[80]. It is predicted theoretically that the electric dipolar interactions between entrapped H_2O results in the ferroelectric alignment of the electric dipole moments at temperatures below the ferroelectric transition temperature T_0, thus generating a crystal field within the lattice [78, 79]. The ferroelectric transition temperature can be estimated using $T_0 = 16\mu^2$. Therefore, by substituting the largest value calculated for the effective electric dipole moment ($P_e = 0.62$ D) into the relation, the ferroelectric transition temperature T_0 is calculated to be 6.15 K. This is consistent with the results from the temperature dependence study of the dielectric permittivity of $H_2O@C_{60}$, where no dielectric anomalies is observed at $T \geq 8$ K [79].

Besides having a permanent electric dipole moment, H_2O also possess a relatively large electric quadrupole moment [84, 85]. Recent quantum calculation of the electric quadrupole moment of H_2O [85] has shown that the linear electric quadrupole moment along the b-axis (Q_0) is 0.28 DÅ, whereas the square planar electric quadrupole moment along the ac-plane (Q_2), which is perpendicular to the b-axis, is 2.13 DÅ.

It can be seen from Figure 7.1.1(a) that the electric dipole moment of the ground state ortho-H_2O (1_{01} state) rotates with its molecular rotation. Hence, it is deduced that the effective electric dipole moment of the ground state of ortho-H_2O is averaged to zero, whereas the ground state para-H_2O (0_{00} state) maintains its electric dipole moment as there is no rotational averaging. However, the same cannot be said for the electric quadrupole moment of H_2O as it is not parallel along the rotation plane. Hence, it is deduced that both ortho- and para-H_2O have non-zero effective electric quadrupole moments. This deduction is later shown to have significant consequences as it leads to the conception of several other deductions made

in this thesis to explain several experimental observations.

Chapter 8

INS spectral analysis of $H_2O@C_{60}$

The objective of the INS study of $H_2O@C_{60}$ discussed in this chapter is to study the quantum dynamics of the entrapped H_2O in the C_{60} cage. The dynamics of the H_2O in this system are particularly interesting because each entrapped H_2O is a freely rotating electric dipole that is arranged in a lattice structure. The INS experiments conducted on the highly purified $H_2O@C_{60}$ sample were recorded using the IN4C, IN5 and IN1-Lagrange spectrometers. All of the INS spectra were recorded by A. J. Horsewill, S. Rols, J. Ollivier and myself at the ILL, Grenoble. The low energy incident neutron investigation of the highly purified sample will give us the resolution to study the breaking of the icosahedral symmetry of the C_{60} cage environment by the electric dipole moment of the entrapped H_2O as well as the interactions between the dipoles of neighbouring H_2O. This breaking of the symmetry has been observed via the splitting in the ortho-H_2O ground state in the preliminary INS spectra [75]. On the other hand, the higher energy incident neutron investigation allows for the study of the higher energy quantum states, which could provide further insights on the symmetry of the cage potential. The assignments of the peaks in the IN4C, IN5 and IN1-Lagrange spectra shown in this chapter are based on the theoretical gaseous water model shown in Figure 7.1.2 [76].

As the $H_2O@C_{60}$ sample exhibits slow ortho-H_2O to para-H_2O conversion at $T < 20$ K, the sample is warmed to $T > 40$ K for 50 minutes prior to each experiments to replenish the population of ortho-H_2O before rapidly cooling it down to the set temperature for measurements.

8.1 Low temperature INS study

8.1.1 IN4C

The IN4C experiments were conducted at temperatures between 150 mK to 1.6 K. A dilution refrigerator insert was used for temperatures below 1.2 K. The IN4C experiments of the $H_2O@C_{60}$ sample performed at 1.6K were recorded using incident neutron wavelengths of 3 Å, 2.3 Å and 1.6 Å respectively; whereas experiments performed in the milli-Kelvin regime were only recorded at 3 Å. The milli-Kelvin spectra are identical to the 1.6 K spectra (Figure 8.1.1). Hence, they will not be illustrated in this section.

The recording procedure of the low temperature IN4C spectra of the purified $H_2O@C_{60}$ sample is similar to the preliminary INS experiment done on the non-purified sample [75]. The sample is equilibrated at $T \geq$50 K before cooling the sample down to 1.6 K for the recording of the spectra. It takes approximately 40 minutes for the sample to cool from $T \geq$50 K to 1.6 K. In order to obtain a set of time dependent spectra, a set of spectra has been continuously recorded with 10 minutes recording time throughout each experiment. These "10 minutes spectra" can be averaged to obtained a spectrum with better signal to noise ratio, which also results in longer time intervals between spectra. However, only the direction of change in the amplitude of the peaks over time is relevant in the INS spectral analysis. Knowing that the change in the amplitude is the result of the depopulation of the ortho-H_2O ground state to the para-H_2O ground state, the origin of the transitions could be determined by analysing the direction of the change in the amplitude of the peaks. If the amplitude of a peak is decreasing over time, then the peak has to originate from the ortho ground state; whereas if the amplitude is increasing overtime, then the peak has to originate para ground state. This additional feature of determining the origin of the peaks is particularly useful in the assignment of the peaks, especially when a large number of peaks is expected based on the large number of non-degenerate energy states in the energy level diagram of gaseous H_2O (Figure 7.1.2).

The time evolution INS spectrum of $H_2O@C_{60}$ recorded with 3 Å incident neutron wavelength is shown in Figure 8.1.1. The red and blue represents spectra recorded during the first and last 90 minutes of the experiment respectively. The entire experiment spans 8 hours 20 minutes from the time in which the sample starts cooling. The labels (J_{K_a,K_c}) represent the final states of their respective peaks; whereas the colour of the labels signify the spin species of the initial state of the transitions, with red

and blue representing the ortho and para ground states respectively. The peaks are identified based on the gaseous water energy level diagram seen in Figure 7.1.2, whereas its initial state is identified based on the change in the amplitude of the peak over time. The shoulder with the 1_{10} label and the peaks with the 0_{00} and 2_{02} labels are observed to be decaying with time. The 0_{00} peak at the NE gain part of the spectra is analysed in detail using the high resolution IN5 spectrometer in the next section. The doublet (1^a_{01} and 1^b_{01}) shows symmetry breaking interaction in the 1_{01} ortho ground state. This symmetry breaking effect is postulated to be caused by the geometrical distortion of the cage due to the cage interacting with the ferroelectrically aligned electric dipole moments of the surrounding para-H_2O. This postulate is discussed in detail in the later part of this chapter (Section 8.3).

The spectra with slightly higher energy excitations (2.3 Å) is shown in Figure 8.1.2. Similar to the 3 Å spectra, the red and blue spectra are spectra recorded during the first and last 90 minutes of the experiment. The merging of the 1_{01} doublet into a single peak is due to the loss of resolution from the use of higher energy incident neutrons. However, the 1_{10} shoulder seen in Figure 8.1.1 can still be identified by obtaining the spectra with only ortho peaks in it (green spectrum in Figure 8.1.2). This can be done by scaling a para peak of the early spectrum to the respective para peak of the later spectrum, before subtracting the scaled spectra by the later spectra. Using the same peak assignment procedure as the 3 Å spectra (Figure 8.1.1), the ortho and para peaks are identified and labelled accordingly based on the energy level diagram of gaseous $H_2O@C_{60}$ (Figure7.1.2). The 2_{12} peaks labelled in Figure 8.1.2 are transitions originating from the ortho (red label) and para (blue label) ground states respectively.

The 1.6 Å spectra of the $H_2O@C_{60}$ sample is illustrated in Figure 8.1.3. The higher energy transfer transitions to the $3_{K_aK_c}$ states are identified and labelled accordingly using the same peak assignment procedure used in the analysis of the 2.3 Å spectra (Figure8.1.2). The slower growth of the 23 meV peak relative to the 2_{12} peak is attributed to the existence of another ortho peak "hidden" within Gaussian. Results of all the IN4C spectra's peak assignments are compiled into Table 8.1.

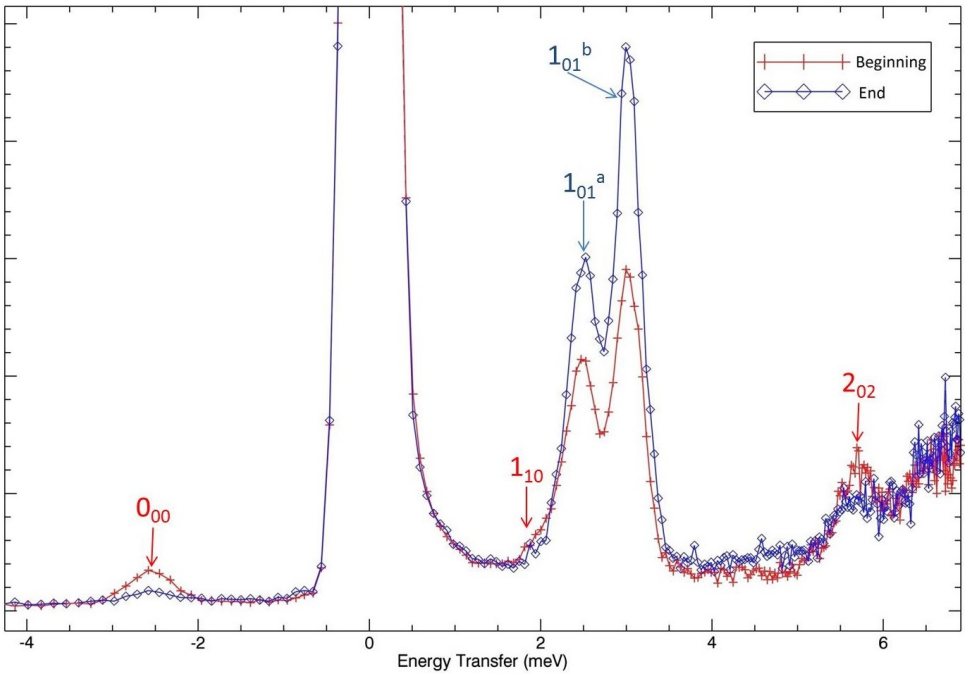

Figure 8.1.1: INS spectra of $H_2O@C_{60}$ recorded at 1.6 K using 3Å incident neutrons. The red and blue spectra are recorded during the first and last 90 minutes of the experiment respectively. The entire experiment spans 8 hours 20 minutes from the time in which the sample starts cooling. The labels signify the final states of their respective peaks, while the red or blue colour of the labels represent transitions which originate from either ortho or para ground states respectively. The identification of the initial state of the peaks are dependent upon the direction of change of the respective peak amplitude over time. See text for details on the peak assignments.

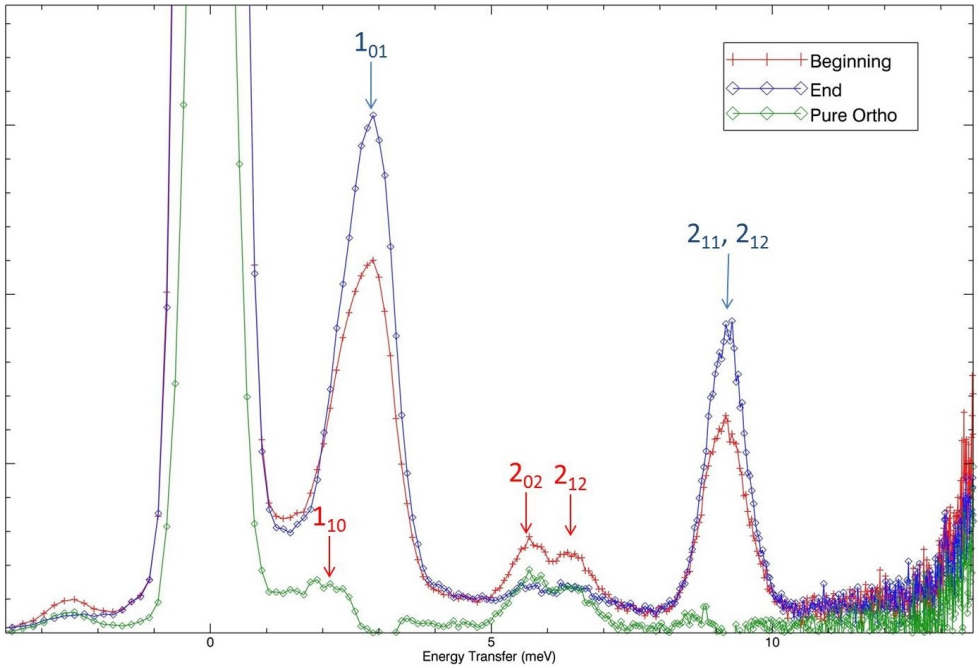

Figure 8.1.2: The 2.3 Å INS spectra of $H_2O@C_{60}$ at 1.6 K. The red spectrum represents the first 90 minutes (beginning) while the blue spectrum represents the last 90 minutes (end). The green spectrum contains only peaks that originate from the ortho ground state (see text for details). The entire experiment spans 8 hours from the time in which the sample starts cooling. The labels signify the final states of their respective peaks, while the red or blue colour of the labels represent transitions which originate from either ortho or para ground states respectively. See text for details on the peak assignments.

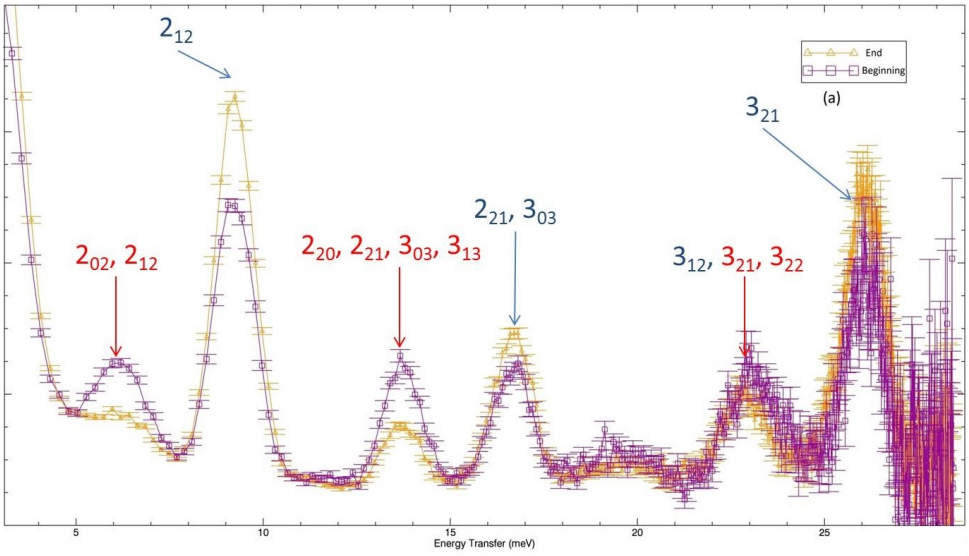

Figure 8.1.3: The 1.6 Å INS spectra of $H_2O@C_{60}$ at 1.6 K. The purple spectrum represents the first 90 minutes (beginning) while the yellow spectrum represents the last 90 minutes (end) of the experiment. The entire experiment spans 8 hours from the time in which the sample starts cooling. The labels signify the final states of their respective peaks, while the red or blue colour of the labels represent transitions which originate from either ortho or para ground states respectively. See text for details on the peak assignments.

$H_2O@C_{60}$ observed INS transitions with IN4C

Initial State ($J_{Ka\,Kc}$)	Final State ($J_{Ka\,Kc}$)	Energy Transfer (meV)
1_{01}^{a}	1_{11}	2.1 ± 0.05
0_{00}	1_{01}^{a}	2.5 ± 0.05
0_{00}	1_{01}^{b}	3.02 ± 0.05
1_{01}^{a}	2_{02}	5.68 ± 0.05
1_{01}^{a}	2_{12}	6.51 ± 0.05
0_{00}	$2_{12}, 2_{21}$	9.2 ± 0.05
1_{01}^{a}	$2_{20}, 2_{21}, 3_{03}, 3_{13}$	13.7 ± 0.1
0_{00}	$2_{21}, 3_{03}$	16.6 ± 0.1
0_{00}	3_{12}	22.8 ± 0.1
1_{01}^{a}	$3_{21}, 3_{22}$	23.3 ± 0.2
0_{00}	3_{21}	26.1 ± 0.2

Table 8.1: Compilation of the $H_2O@C_{60}$ INS peak positions as observed in the IN4C spectra. The assignment of the peaks are based on the theoretical gaseous water model in Figure 7.1.2. Peaks with multiple final states are those believed to contain unresolved multiplets.

8.1.2 IN5

The NE gain part of the spectra can be observed with much higher resolution using the IN5 spectrometer. Similar to the IN4C experiments, the sample is warmed to T> 40 K for 50 minutes to replenish the ortho-H_2O population before cooling it down rapidly to the set temperature in the space of 30 minutes to begin the experiment. The IN5 spectra are continuously recorded with 10 minutes recording time throughout each experiment. These "10 minutes spectra" are then grouped to obtained a spectrum with better signal to noise ratio.

The IN5 spectra seen in Figure 8.1.4 are recorded using 5 Å incident neutron wavelength at sample temperatures of 3 K and 1.5 K respectively. The energy transfer range of the spectra is set to be $-3.5 \leq \Delta E \leq -1.5$ meV. The -3.09 meV peak in Figure 8.1.4c is the 1^b_{01} to 0_{00} transition. It can be seen from Figure 8.1.4a, b and c that there is a shoulder ($1^{a'}_{01}$ to 0_{00}) next to the main -2.61 meV peak (1^a_{01} to 0_{00}). This shoulder is centred on -2.46 meV and is seen to be decaying at the same rate as the -2.61 meV peak (Figure 8.1.4a).

It can concluded that this shoulder is not a separate quantum state from the 1^a_{01}state for the following three reasons: Firstly, if it were to be a separate quantum state like the 1^b_{01}, we would expect a larger population in the $1^{a'}_{01}$ state than the higher energy 1^a_{01} state at low temperature. Secondly, the amplitude ratio between the -2.61 meV and -2.46 meV peak remains the same at higher temperatures. Thirdly, the conversion decay rate of the two peaks are identical. Hence, the $1^{a'}_{01}$ state is most likely a minority population of the 1^a_{01}state which experience a slightly different environmental potential as compared to the majority population. This is possibly due to H_2O molecules in the $1^{a'}_{01}$ state having an empty C_{60} cage next to it, which results in this H_2O molecule experiencing slightly less electric dipole-dipole interaction with its neighbours.

Assuming that the 1^b_{01} state is doubly degenerate and the 1^a_{01} state is non-degenerate, the weighted mean energy of the three peaks that constitute the 1_{01} state is calculated to be 2.93 meV, which is consistent with the energy of the 1_{01} state calculated in the gaseous H_2O model.

Unlike the $H_2@C_{60}$, there is no observable shift in the position of the main rotational peak (ortho ground state to para ground state transition) with temperature in the IN5 spectra.

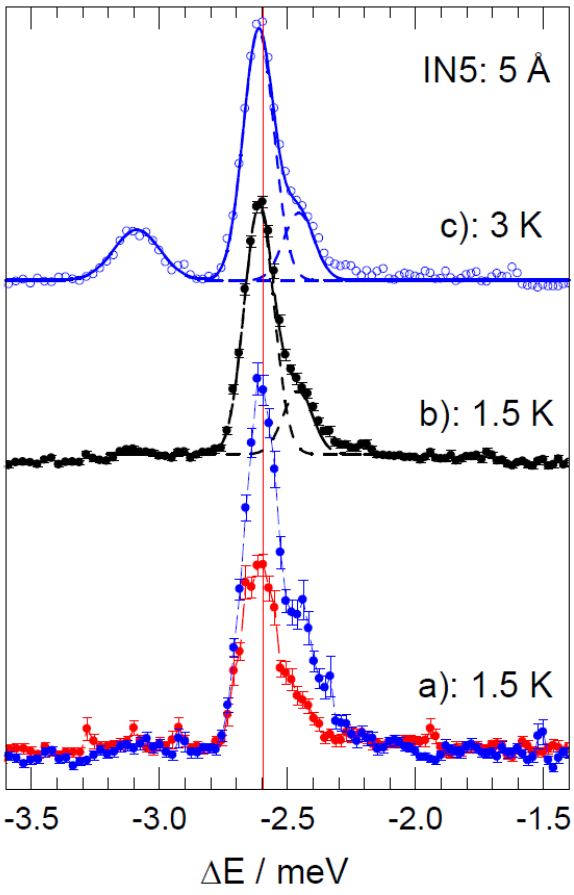

Figure 8.1.4: The 5 Å INS spectra recorded with IN5 spectrometer at sample temperatures of 1.5 K and 3K. All the peaks shown in this figure represent transitions from the 1_{01} state to the 0_{00} state. Figure a) shows spectra recorded in the first hour (red) and the fifth hour (blue) after cooling. The peak centred on the red line originates from the 1^{a}_{01} state. Figure b) shows the spectra recorded over a period of 5 hours after cooling. c) the sum of all neutrons recorded during the first 3 hours after cooling to 3 K. The appearance of the peak centred on -3.09 meV arises from the population of the 1^{b}_{01} state. The -2.46 meV shoulder is the transition originating from the $1^{a'}_{01}$ state (see text for more details). This splitting of the 1_{01} state is also observed in the 3 Å IN4C spectra (Figure 8.1.1).

8.1.3 IN1-Lagrange

The higher energy excitations (13 meV$\leq \Delta E \leq$ 80 meV) of $H_2O@C_{60}$ have been measured using IN4C and IN1-Lagrange. Similar to the $H_2O@C_{60}$ experiments recorded with IN4C and IN5, the sample is warmed to T$>$ 40 K for 50 minutes to replenish the ortho-H_2O population before cooling it down rapidly to 2.5 K temperature to begin the experiment. The peak resolution of the IN4C spectrometer is higher in the energy transfer region of 13 meV$\leq \Delta E \leq$20 meV, while the peak resolution of the IN1-Lagrange spectrometer is higher in the energy transfer region of $\Delta E \geq$20 meV. Thus, in this section, high energy excitations in the energy transfer region of $\Delta E \geq$20 meV are discussed.

The IN1-Lagrange experiment is performed at 2.5 K over a period of 23 hours. The IN1-Lagrange spectra of the $H_2O@C_{60}$ recorded at the beginning (red) and end (blue) of the experiment is shown in Figure 8.1.5. The INS signals from the Al in the foil sample holder and the C_{60} cages in the sample are removed from the $H_2O@C_{60}$ spectra by subtracting the separately measured "blank" sample spectra from the $H_2O@C_{60}$ spectra. This blank sample had a mass matched quantity of C_{60} inside an identical Al foil sachet. The red and blue spectra are recorded over the first and last 5 hours of the experiment respectively. The red spectrum contains a mixture of peaks originating from either the ortho-H_2O or para-H_2O ground states, while the blue spectrum ("pure para-H_2O spectrum") contains only peaks originating from the para-H_2O ground state to the ortho-H_2O states, as transitions from para-H_2O ground state to higher energy para-H_2O states are negligible. The black spectrum is the pure ortho-H_2O spectrum, which is obtained using similar subtraction procedure to those used to obtain the pure ortho-H_2O spectrum of the 2.3 Å IN4C spectra (see Section 8.1.1). The assignment of the peaks are based on the gaseous H_2O energy level diagram in Figure 7.1.2, with the origin of the peaks determined from the direction of change of the respective peak amplitudes.

The 3_{12} and 3_{21} labelled para-H_2O peaks, which are observed in the IN4C spectra (Figure 8.1.3), are also observed in the pure para-H_2O IN1-Lagrange spectrum (blue) in Figure 8.1.5. Due to the diminishing resolution at $\Delta E \geq$ 30 meV, it becomes increasingly ambiguous to assign transitions to the peaks in the $\Delta E \geq$ 30 meV energy transfer region. Nevertheless, there are a few obvious peaks in the $\Delta E \geq$ 30 meV energy transfer region of the pure para-H_2O spectra that follows the pattern exhibited by pure rotations of gaseous H_2O, such as peaks from the para-H_2O ground

state to the 5_{05}, 4_{32}, 5_{23}, and 6_{16} ortho-H_2O states. In the case of the pure ortho-H_2O spectrum (black) in Figure 8.1.5, the final state can either be para or ortho-H_2O. Therefore, pure ortho-H_2O spectrum is expected to contain twice as many peaks as the pure para-H_2O spectrum, which contains only peaks with ortho-H_2O final state. The doubling of the peak density combine with the inferior neutron counting statistics in the $\Delta E \geq 30$ meV energy transfer region results in little discernible detail in the $\Delta E \geq 30$ meV energy transfer region.

The peaks in the pure para-H_2O and ortho-H_2O spectra which do not follow the pattern exhibited by pure rotations of gaseous H_2O are labelled with question marks and asterisks. The two peaks labelled with asterisks are discussed in the translational modes section (Section 8.1.4), while the two peaks labelled with question marks remained unknown. The assignments of the peaks in the IN1-Lagrange spectra observed in Figure 8.1.5 are compiled into Table 8.2.

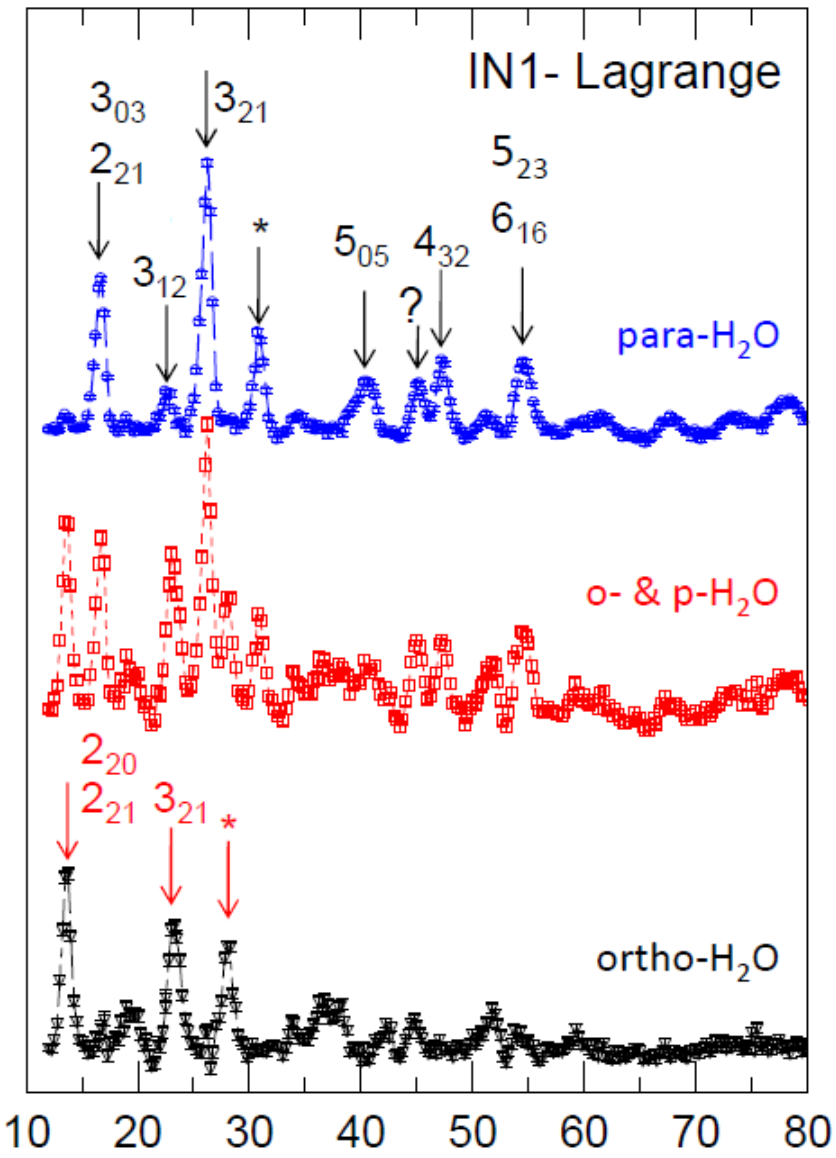

Figure 8.1.5: $H_2O@C_{60}$ INS spectra recorded with IN1-Lagrange at 2.5 K. (Blue): The spectrum is recorded during a 5 hour period beginning at 18 hours after the initial cooling of the sample from T> 40 K. The sample consists mainly of para-H_2O at this point of the experiment. (Red): The spectrum is recorded during the first 3 hours after cooling. The sample consists of a mixture of ortho-H_2O and para-H_2O at this point of the experiment. (Black) The spectrum is the result of the scaled subtraction of the blue spectrum from the red spectrum. This spectrum consists of peaks originating from ortho-H_2O ground state. The unassigned peaks which are labelled with question marks and asterisks are explained in text.

$H_2O@C_{60}$ observed INS transitions with IN1-Lagrange		
Initial State ($J_{Ka\,Kc}$)	Final State ($J_{Ka\,Kc}$)	Energy Transfer (meV)
1_{01}[a]	$2_{20}, 2_{21}, 3_{03}, 3_{13}$	13.7 ± 0.1
0_{00}	$2_{21}, 3_{03}$	16.6 ± 0.1
0_{00}	3_{12}	22.8 ± 0.1
1_{01}[a]	$3_{21}, 3_{22}$	23.3 ± 0.2
0_{00}	3_{21}	26.1 ± 0.2
1_{01}	*	28.1 ± 0.2
0_{00}	*	30.8 ± 0.2
0_{00}	?	39.4 ± 0.2
0_{00}	5_{05}	40.7 ± 0.2
0_{00}	?	45.1 ± 0.2
0_{00}	4_{32}	47.3 ± 0.2
0_{00}	$5_{23}, 6_{16}$	54.6 ± 0.2

Table 8.2: Compilation of the peak assignments of the IN1-Lagrange spectra in Figure 8.1.5.

8.1.4 Translational modes

Information on the translational modes of the entrapped H_2O have remained largely unknown as no quantum chemical calculations of the cage potential has yet been done. The first translational mode in the $H_2@C_{60}$ is observed to be centred on 22.5 meV. By considering the simple analysis based on a harmonic cage potential, the translational energy of H_2O should be a factor of 3 less than the H_2 counterpart (which is 7.5 meV) due to the translational energies scaling inversely with the square root of the reduced mass of the entrapped molecule. However, despite sharing the same cage as the $H_2@C_{60}$ system, the translational dynamics of H_2O entrapped in the C_{60} cage is significantly different than its H_2 counterpart. This is because the non-bonding interaction between H_2O and the C_{60} cage is vastly different to its H_2 counterpart. Therefore, the translational dynamics of $H_2@C_{60}$ are unable to be used as a reference for this system.

Besides the symmetry breaking mechanism observed in the ortho-H_2O ground state, the observed INS peaks with $\Delta E \leq 30$ meV have shown considerable consistency with the energy transfer values derived from the gaseous H_2O energy level diagram in Figure 7.1.2. However, the 30.8 meV peak labelled with asterisk in the pure para-H_2O spectrum have an energy transfer value which differs from the two closest para→ortho transitions in gaseous H_2O by +2.9 and -4.6 meV respectively (significantly larger

than experimental uncertainties). Similarly, the 28.1 meV peak in the pure ortho-H_2O spectrum has an energy transfer value which offsets the two nearest ortho→ortho or ortho→para rotational transitions in gaseous H_2O by ±3 meV. The offset values of the two peaks from their nearest rotational states are too large to be attributed to the symmetry breaking effect seen in the ortho-H_2O ground state. More significantly, the energy difference between the 30.8 meV and 28.1 meV peaks is close to the mean energy of the doublet in the ortho-H_2O ground state, thus leading to the conclusion that the two peaks share the same final state. However, the increase in mass of H_2O combined with the basic principles based on the harmonic potential concludes that this unassigned final state (denoted with asterisk) is unlikely to be the first translational mode. For the unassigned final state to be the first translational mode, the cage potential for $H_2O@C_{60}$ has to be substantially narrower than that of $H_2@C_{60}$. Nevertheless, it is possible that this unassigned state is related to the a higher translational harmonics or a combined translation-rotation transition.

8.1.5 Energy levels

As no theoretical model for the $H_2O@C_{60}$ system has been calculated, the theoretical gaseous water model is instead used as a reference to construct the energy level table of $H_2O@C_{60}$ for the lower energy levels based on the INS experiments. These energy levels will inform future computational and theoretical studies. The energy level table in Figure 8.1.6 is constructed based on the compilation of the observed INS peak positions shown in Table 8.1. The energy value of 1^b_{01} state is shown to be 2.61 meV instead of 2.5 meV in Table 8.1 is due to further splitting in the 1^b_{01} state (see Figure 8.1.4). The 1_{10} and 2_{11} states are not observable in the IN4C spectra. Their associated energy values are based on those calculated from the gaseous water model. The difference in energy between 2_{20}, 2_{21}, 3_{13} and 3_{03} states are too small to be resolved from the spectra. The same is also true for the 3_{21} and 3_{22} states. The construction of the energy level diagram of the $H_2O@C_{60}$ in Figure 8.1.7 is based on the energy values in Table 8.1.6 for the observed energy states, and the energy level diagram of the gaseous water model (Figure 7.1.2) for the unobserved energy states.

Para		Ortho	
$J_{Ka\,Kc}$	Energy (meV)	$J_{Ka\,Kc}$	Energy (meV)
$0_{0\,0}$	0.00`	$1_{0\,1}{}^{a}$	2.61 ± 0.05
$1_{1\,1}$	4.71 ± 0.05	$1_{0\,1}{}^{b}$	3.02 ± 0.05
$2_{0\,2}$	8.29 ± 0.05	$1_{1\,0}$	5.42` *
$2_{1\,1}$	11.8` *	$2_{1\,2}$	9.12 ± 0.05
$2_{2\,0}$	16.31 ± 0.1 !	$2_{2\,1}$	16.6 ± 0.1 !
$3_{1\,3}$	16.31 ± 0.1 !	$3_{0\,3}$	16.6 ± 0.1 !
$3_{2\,2}$	26.1 ± 0.2 !	$3_{1\,2}$	22.8 ± 0.1
		$3_{2\,1}$	26.1 ± 0.2 !
		$5_{0\,5}$	40.7 ± 0.2
		$4_{3\,2}$	47.3 ± 0.2
		$5_{2\,3}$	54.6 ± 0.2
		$6_{1\,6}$	54.6 ± 0.2

* Not observed (Energy value is based on gaseous water)

! Cannot be resolved

Figure 8.1.6: Energy level table of $H_2O@C_{60}$ based on the compilation of the observed INS peak positions shown in Table 8.1. The energy value of 1^a_{01} state is shown to be 2.61 meV instead of 2.5 meV in Table 8.1 because of the further splitting in the 1^b_{01} state (see Figure 8.1.4). The energy values of the 1_{10} and 2_{11} states are based on the theoretical gaseous water model as transitions to these states are not observable. The difference in energy between 2_{20}, 2_{21}, 3_{13} and 3_{03} states are too small to be resolved from the spectra. The same is also true for the 3_{21} and 3_{22} states.

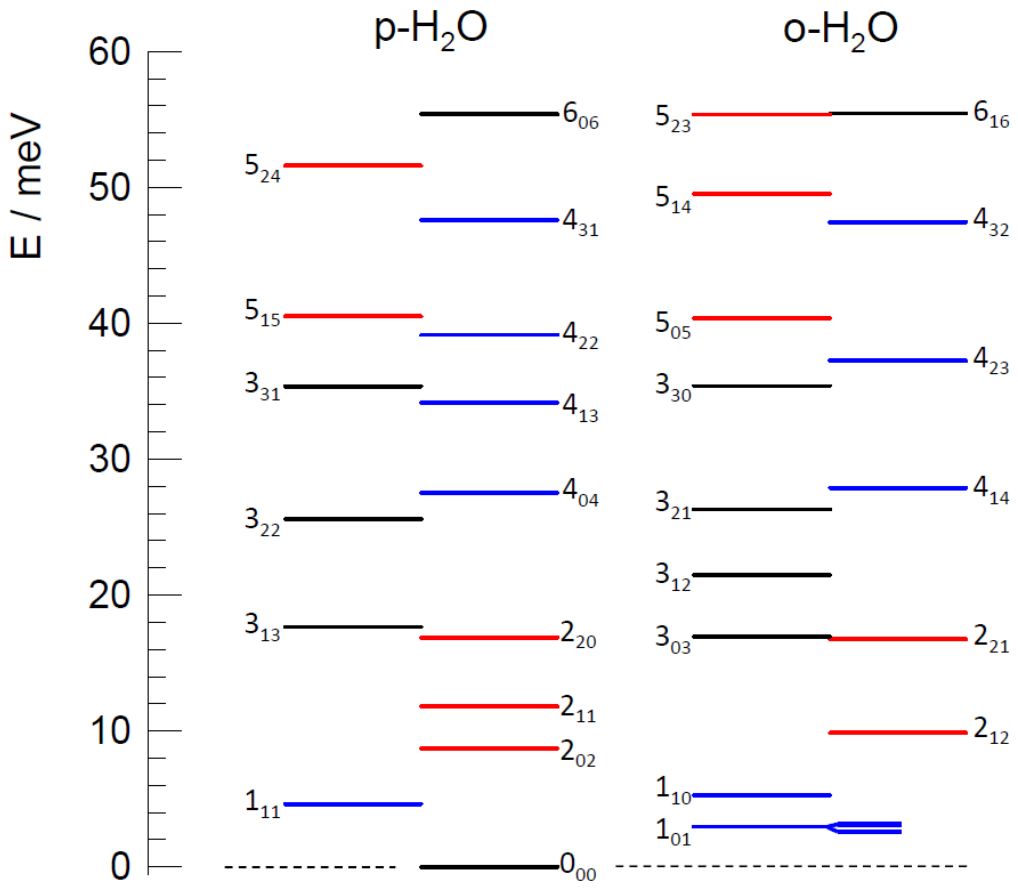

Figure 8.1.7: The energy level diagram of the $H_2O@C_{60}$. The states are labelled by the quantum numbers $J_{K_aK_c}$(see text for details), where the ortho and para states are distinguished by the respective odd and even values of $K_a + K_c$. The energy values of the lower energy states are based on Table 8.1.6, whereas the energy values of the higher energy states are based on the energy level diagram of the theoretical gaseous water model in Figure 7.1.2.

8.2 Temperature dependence study using cold neutron scattering

Similar to the IN5 experiment for $H_2@C_{60}$, the aim of this experiment is to obtain the temperature dependence of the peak amplitudes to determine their degeneracy and energy values. The temperature dependence IN5 spectra are recorded using incident neutron wavelength (λ_n) of 5 Å. The sample is warmed to T> 40K for 50 minutes to replenish the ortho-H_2O population before rapidly cooling it down to set temperature to begin recording the spectra. Unlike the low temperature INS spectra shown in Section 8.1, ortho to para conversion cannot be used to determine the origin of the peaks at higher temperatures for the following reasons: At $3 \leq T \leq 10$ K, peaks from higher energy ortho states which do not undergo nuclear spin-isomer conversion to para ground state begin to appear. However, the amplitude of the peaks originating from the ortho ground state (-2.61 and -2.46 meV) are still observed to decay with time; At $10 \leq T \leq 25$ K, the difference in population between the equilibrium and non-equilibrium ortho ground state becomes too small to be observed; At $T > 25$ K, the states of both spin species quickly equilibrate.

Due to the current lack of knowledge of the translational modes of the $H_2O@C_{60}$ system, only the temperature dependence analysis of the pure rotational transition region ($-3.8 \leq \Delta E \leq -1.9$ meV) of the IN5 spectra is discussed. A similar fitting procedure to the one used in the analysis of the $H_2@C_{60}$ temperature dependence IN5 spectra has been applied for this analysis. Examples of the fitted IN5 spectra recorded in the temperature range of $1.5 \leq T \leq 20$ K and energy transfer range of $-3.8 \leq \Delta E \leq -1.9$ meV are shown in Figure 8.2.1. Only spectra of up to 20 K have been chosen for this analysis because there are still unanswered questions regarding the higher energy levels of $H_2O@C_{60}$, such as the energy of the translational modes. By assuming that the highest occupied states being the 1_{11} (for para-H_2O) and the 1_{10} (for ortho-H_2O) states, we are able to identify 9 transitions which falls within the $-3.8 \leq \Delta E \leq -1.9$ meV energy transfer region. These 9 transitions are then categorised into 4 combined Gaussians as shown in Table 8.3. The energy transfer values of the transitions shown in Table 8.3 are based on the energy level table shown in Figure 8.1.6. These 4 combined Gaussians are then used to fit the spectra in Figure 8.2.1. In the fitting of the 1.5 K, 3 K and 5 K spectra, the FWHM of the -2.49, -2.64 and -3.09 meV combined Gaussians are fixed at 0.15, 0.15 and 0.25 meV respectively. The wider than resolution FWHM of the -3.09 meV

peak indicates that there is a further splitting in the 1^b_{01} state that is similar to the case of 1^a_{01} and $1^{a'}_{01}$ states. This further splitting in the 1^b_{01} state is also observed in the FIR spectra [75]. As for fitting of the 10 K, 15 K and 20 K spectra, the FWHM of the combined Gaussians are allowed to float to signify the increased number of peaks they represents (see Table 8.3) due to the occupation of the higher energy states (1_{10}, 1_{11} and 2_{02} states). This results in the higher temperature spectra having a wider combined Gaussians than the lower temperature spectra.

Combined Gaussian peak position (meV)	Initial State $(J_{Ka\,Kc})$	Final State $(J_{Ka\,Kc})$	Enegy Transfer (meV)
-2.18	1_{11}	1_{01}^{a}	-2.1
	1_{11}	$1_{01}^{a'}$	-2.24
-2.49	$1_{01}^{a'}$	0_{00}	-2.47
	1_{10}	1_{01}^{b}	-2.4
-2.64	1_{01}^{a}	0_{00}	-2.61
	1_{10}	1_{01}^{a}	-2.81
	2_{02}	1_{10}	-2.87
-3.09	1_{01}^{b}	0_{00}	-3.02
	1_{10}	$1_{01}^{a'}$	-2.95

Table 8.3: Table showing the 4 combined Gaussians used to fit the IN5 spectra in Figure 8.2.1 as well as the transitions they represents. The energy transfer values of the transitions are based on the energy level table shown in Figure 8.1.6.

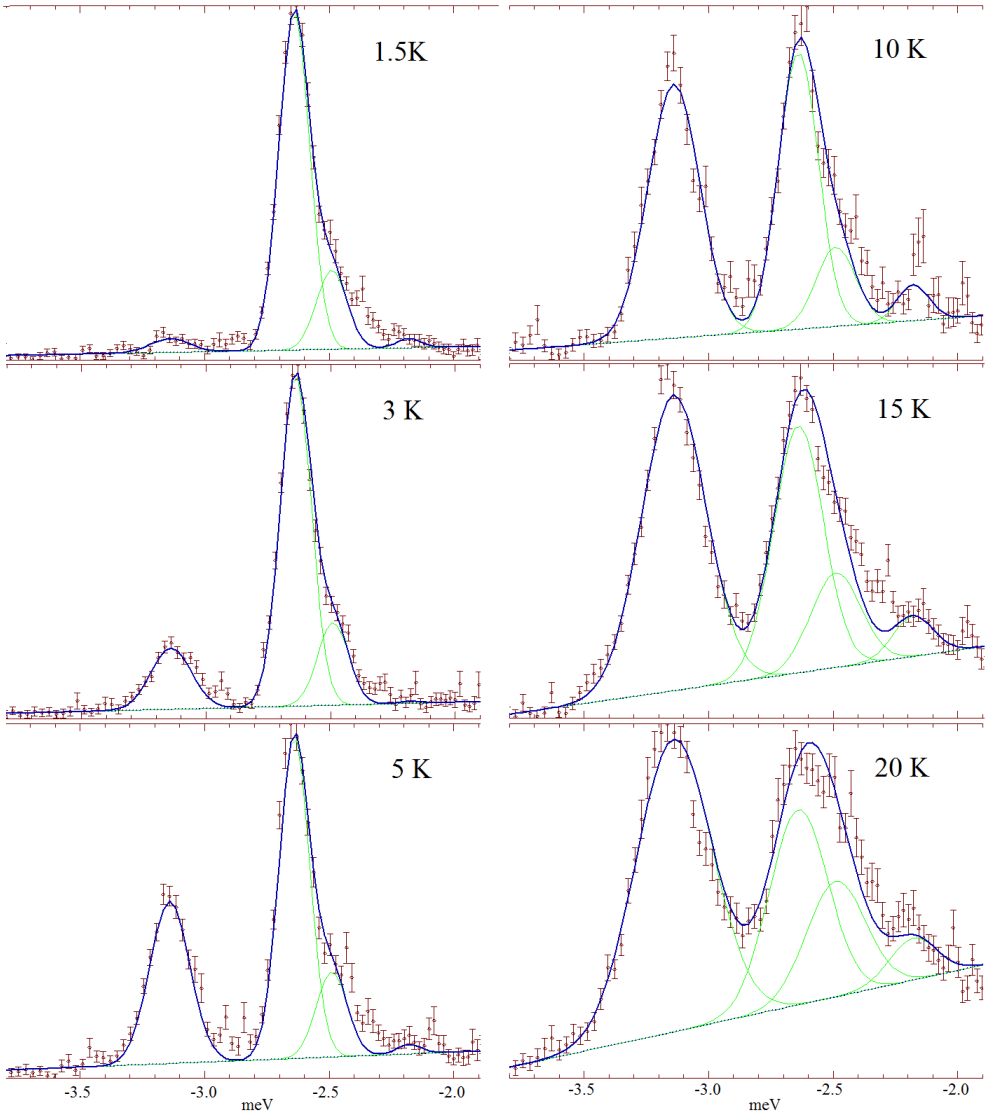

Figure 8.2.1: The IN5 spectra (λ_n= 5 Å) of $H_2O@C_{60}$ recorded 3 hours after cooling the sample to: 3 K; 10 K; 15 K; 20 K; 34 K; 45 K. The data are fitted with the 4 combined Gaussians shown in Table 8.3. Details of the fitting constraints can be found in text. Detailed description of the 1.5 K, 3 K and 5 K spectra can be found in Figure 8.1.4. The broadening of the peaks in the 10 K, 15 K and 20 K spectra signifies the emergence of the transitions originating from the higher energy states.

The amplitudes of the fitted combined Gaussians of different temperatures are then compiled into a temperature dependence plot of the respective Gaussian amplitudes (see Figure 8.2.2). The temperature dependence plot of the -2.49 meV (red circles) and -2.64 meV (blue squares) combined Gaussian amplitudes are summed to obtain a temperature dependence plot (black marker in Figure 8.2.2). This sum represents a more accurate description of the statistical distribution as both peaks originate from the same 1^a_{01} state albeit a slightly different environmental potential. The

brown triangles are the temperature dependence plot of the -3.09 meV combined Gaussian, which comprises of a transition that originates from 1^b_{01} state at low temperatures. It can be seen that the summed combined Gaussian amplitudes diminishes with increasing temperature, whereas the -3.09 meV combined Gaussian grows with increasing temperature.

Both black and brown data are fitted using the Boltzmann equation (Equation 4.2.1) with the modified partition function (4.2.4). Unlike the $H_2@C_{60}$, nuclear spin-isomer conversion do occur even at the lowest temperature. Hence, the q_p and q_o states are chosen to be the 1_{11} (first excited para state) and the 1^a_{01} (ortho ground state) states respectively for the purpose of calculating the modified partition function. To obtain the best fits for the the summed (black) and -3.09 meV (brown) temperature dependence plots, the degeneracy of the 1^a_{01} and 1^b_{01} states are set to 1 and 2 respectively (total degeneracy of the 1_{01} state is 3). Knowing that the 1^a_{01}state is non-degenerate reinforces the hypothesis that the 1^a_{01} and $1^{a'}_{01}$ states are of the same quantum state. The good fit to the -3.09 meV and the summed temperature dependence plot at low temperature further confirms the size of the splitting in the 1_{01}.

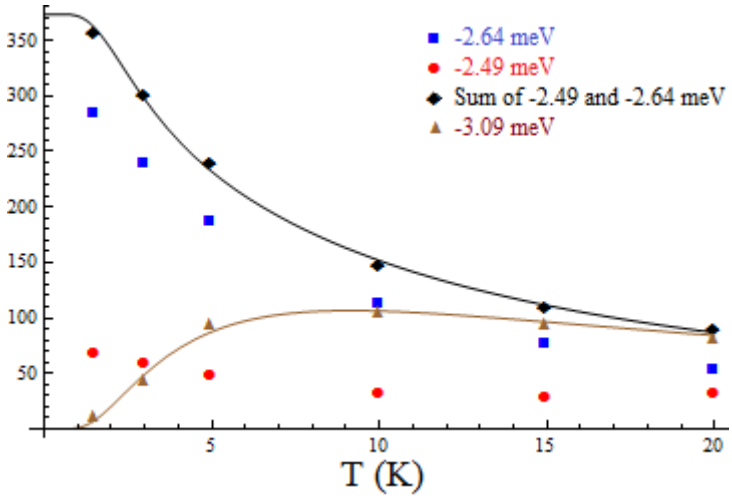

Figure 8.2.2: Temperature dependence plot of the amplitudes of the combined Gaussians obtained from the fit in Figure 8.2.1. The black diamond markers are the sum of the amplitude of the -2.49 and -2.64 meV peaks. This sum represents a more accurate description of the statistical distribution as both peaks originate from the same 1^a_{01} state albeit a slightly different environmental potential. The black and brown lines are the best fits to the data points of their respective colours using the Boltzmann equation (Equation 4.2.1) with the modified partition function (4.2.4).

8.3 Symmetry breaking mechanism

Knowing the distribution of the degeneracies between the 1_{01} states (singly degenerate 1_{01}^{a} state ($m_z = 0$) and doubly degenerate 1_{01}^{b} state ($m_z = \pm 1$)) from the temperature dependence analysis of the peak amplitudes has provided valuable insight in understanding the mechanism behind this symmetry breaking effect. It is postulated that this symmetry breaking is due to the distortion of the cage symmetry from the interaction with the net electric field generated by the ensemble of the ferroelectrically aligned electric dipole moments of the neighbouring para-H_2O (crystal field, $\vec{E}_{crys}$), as the ground state ortho-H_2O is deduced to not have an effective electric dipole moment (as explained in Section 7.1). The nature of this distortion can either be geometrical or electronic distortion.

The crystal field generated (in the direction along the z-axis) by the ensemble of neighbouring para-H_2O induces an electric dipole moment on the C_{60} cage of an entrapped ortho-H_2O, thus generating an electric field between the two poles (along the z-axis) of the cage. In the case of geometrical distortion, the induced internal cage electric field then results in a Coulomb attraction between the two poles which is large enough to compress the C_{60} cage along the z-axis into an antithesis of the C_{70} (with oblate symmetry). It is shown in the INS spectral analysis of $H_2@C_{70}$ (Chapter 6) that the lower energy state has a degeneracy $g = 2$, whereas the higher energy state has $g = 1$. Hence, the opposite values of g detected for the two lowest ortho-$H_2O@C_{60}$ states is in-line with the oblate symmetry distortion postulate.

In the case of the electronic distortion, the induced internal cage electric field breaks the symmetry of the rotational state ground state of ortho-H_2O via the Stark effect. The energy of the multipole expansion is written as follows:

$$W = q\Phi - \overrightarrow{p} \cdot \overrightarrow{E} - \frac{1}{6}\sum_{i}\sum_{j} Q_{ij}\frac{\partial \overrightarrow{E_j}}{\partial x_i} + ... \qquad (8.3.1)$$

where q is the charge, Φ is the electric potential and Q_{ij} is the traceless quadrupole moment tensor [86]. It can be seen from this equation that the dipole interaction energy is dependent on the electric field strength while the quadrupole interaction energy is dependent on the electric field gradient. If the internal cage electric field were to couple with the electric dipole moment of ortho-H_2O to result in this splitting, one could find by solving the Hamiltonian that the degeneracy distribution have to be 2:1

instead of the observed 1:2. However, if the internal cage electric field were to couple with the electric quadrupole moment of ortho-H_2O instead, the degeneracy distribution could be either 2:1 or 1:2. Therefore, the observed 1:2 degeneracy distribution suggests that the induced internal cage electric field couples only with the electric quadrupole moment of the ground state ortho-H_2O and not the electric dipole moment. One can explain the absence of the electric dipole interaction by using the postulate in Section 7.2 that the ortho-H_2O ground state does not have an effective electric dipole moment.

The energy of the interaction with the electric quadrupole moment is dependent on the electric field gradient [86]. As the electric charges of the induced dipole of the cage is expected to spread along the curved surface of the C_{60}, the internal cage electric field generated by the induced dipole ($\overrightarrow{E_{int}}$) would not be constant (see Figure 8.3.1) and has a non-zero electric field gradient. Hence, there would be a coupling between the induced electric dipole moment of the cage and the electric quadrupole moment of ortho-H_2O.

If the ortho-H_2O were to have an effective electric dipole moment, then the C_{60} cage would be primarily distorted by the effective electric dipole moment of the ortho-H_2O in the cage. In this case, one would expect the rotational wavefunctions of all three 1_{01} states to be identical, as the geometrical distortion of the cage is always along the axis of the electric dipole moment (b-axis), thus resulting in no splitting in the 1_{01} states. Therefore, it is concluded that the source of the distortion has to be non-local to the cage for the observed symmetry breaking effect to occur. As the C_{60} molecule is likely to be rigid, the electronic distortion postulate is likely more plausible than the geometrical distortion postulate.

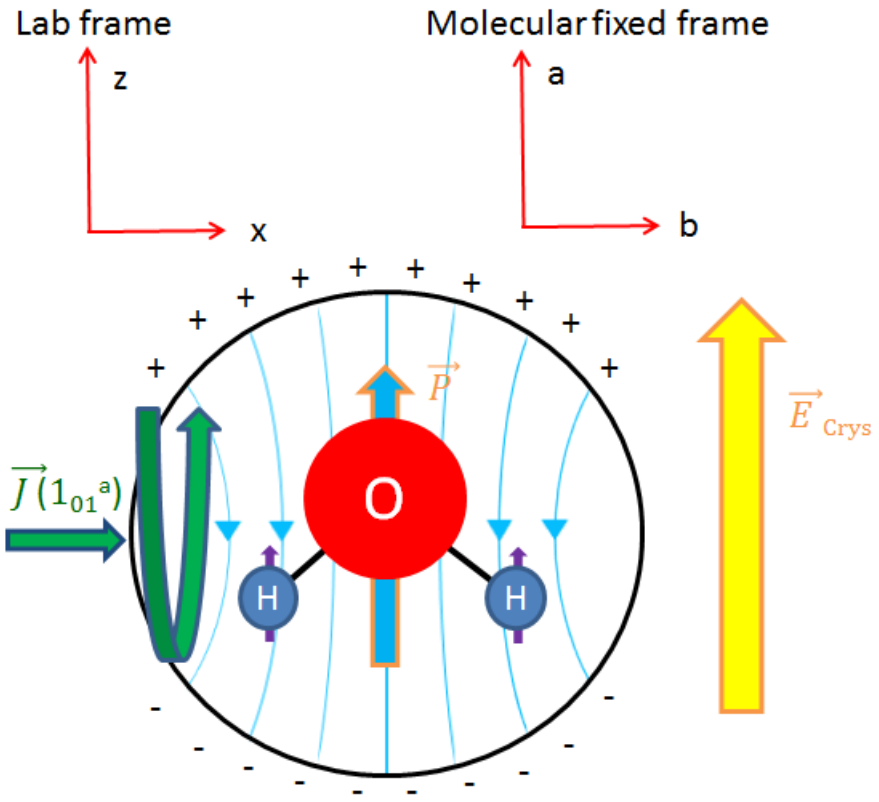

Figure 8.3.1: Illustration of the molecular dynamics of the ortho-H_2O ground state (1^a_{01}) in the C_{60} cage with an induced electric dipole moment. The crystal field ($\vec{E}_{crys}$), which is along the z-axis, electrically polarises the poles of the cage to generate an internal electric field within the cage. As the surface of the cage is curved, the internal electric field will have a non-zero electric field gradient which then interacts with the electric quadrupole moment of H_2O. This interaction lifts the degeneracy of the rotational wavefunction of the ortho-H_2O ground state (1_{01}) into a lower energy singly degenerate wavefunction with rotational angular momentum ($\vec{J}(1^a_{01})$, $m_z = 0$) and a higher energy doubly degenerate wavefunction with rotational angular momentum $\vec{J}(1^b_{01})$ ($m_z = \pm 1$). There are no electric dipole interaction between the H_2O and the internal electric field because the effective electric dipole moment of ortho-H_2O is zero.

8.4 Conclusion

The INS investigations of $H_2O@C_{60}$ with different energy transfer ranges have provided insights on the influences of the neighbouring entrapped H_2O, which are arranged in a lattice structure, onto the dynamics of an entrapped H_2O. The influences of the neighbouring entrapped H_2O (symmetry-breaking) and the confining potential of the C_{60} cage (translational modes) onto the dynamics of an entrapped H_2O are determined by comparing the observed energy states of the $H_2O@C_{60}$ with the calculated rotational states of the gaseous H_2O.

Observing the decay of the INS peak amplitudes over time due to nuclear spin-isomer conversion has given us an "additional dimension" in determining the origin of the transitions. Using a combination of high resolution cold neutron and high flux thermal neutron spectrometers to study the NE gain and NE loss regions respectively has enabled us to determine the dynamical states of the entrapped H_2O with good resolution. However, the translational motion of the H_2O orbiting within the cage has not been taken into account in the IN4C and IN5 analysis. This is due to a lack of knowledge of the interaction between the H_2O and its C_{60} cage. Hence, the energy level diagram constructed in Figure 8.1.7 is still incomplete, as the higher energy states ($E > 30$ meV) would require high-quality computational investigation such as those pioneered by Bacic and Xu [44, 45, 46]. Nevertheless, the lower energy states ($E < 30$ meV) are accurately determined on the basis of experimental data as they are likely to be in the ground translational mode. There are peaks in the $\Delta E \geq 30$ meV energy transfer region of the IN1-Lagrange spectra that do not follow the pattern exhibited by pure rotations of gaseous H_2O. These peaks are unlikely to be due to the first translational mode. However, there is a possibility that these unassigned states are related to the a higher translational harmonics or a combined translation-rotation transition.

The splitting of the ortho-H_2O ground state (1_{01}) has been identified to be due to the symmetry-breaking interaction acting on the H_2O molecules in their C_{60} cages. A further splitting of 0.15 meV in the lower ortho ground state (1^a_{01}) has also been observed with the high resolution IN5 spectrometer. However, by analysing the temperature dependence of the peak amplitudes, it is confirmed that this splitting is not due to the aforementioned symmetry-breaking effect. The result of the temperature dependence analysis has shown that the 1^a_{01} state is non-degenerate, while the 1^b_{01} state is doubly degenerate. Therefore, both 1^a_{01} and $1^{a'}_{01}$ states have

to be of the same quantum state. Furthermore, if $1_{01}^{a'}$ were to be of a different quantum state than 1_{01}^{a}, the occupation of the higher energy 1_{01}^{a} state should be much lower than the $1_{01}^{a'}$ state at 1.5 K. This splitting in the 1_{01}^{a} state is hypothesised to arise from the population of the $1_{01}^{a'}$ state experiencing a slightly different environment than the bulk 1_{01}^{a} population.

The $H_2O@C_{60}$ is shown to be more sensitive to the molecular environment external to the fullerene cage than the $H_2@C_{60}$. This is evident from the 0.5 meV splitting in the ortho-H_2O ground state from both symmetry-breaking effect (1_{01}^{a} and 1_{01}^{b} states) and environmental inhomogeneities (1_{01}^{a} and $1_{01}^{a'}$ states); whereas the splitting in the ortho-H_2 ground state is measured to be 0.14 meV (see Section 4.2.2.1). This difference between the $H_2@C_{60}$ and $H_2O@C_{60}$ system may be attributed to the electric quadrupole moment of H_2O (2.57 DÅ) being 4 times larger than that of H_2 (0.66 DÅ). It is also worth noting that the 1:2 degeneracy distribution of the ortho ground states of $H_2O@C_{60}$ is similar to the 1:2 degeneracy distribution of the ortho ground states of $H_2@C_{60}$. Hence, it is possible that both $H_2@C_{60}$ and $H_2O@C_{60}$ experience a similar symmetry breaking effect on their respective ortho ground state.

It is deduced that the symmetry breaking effect which causes the splitting in the 1_{01} state is due to the indirect coupling between the crystal field and the electric quadrupole moment of the ortho-H_2O. The crystal field induces an electric dipole moment on the cage, which then generates an internal electric field that couples with the electric quadrupole moment of ortho-H_2O. It is also deduced that the symmetry breaking effect is not due to the crystal field coupling with the electric dipole moment of ortho-H_2O.

Chapter 9

NMR spectral analysis of $H_2O@C_{60}$

NMR spectroscopy provides insights on the small intermolecular interactions between nuclear spins which are complementary to the INS and FIR spectroscopy. Preliminary MAS NMR experiment has been done on the impure $H_2O@C_{60}$ sample by our collaborators at the University of Southampton [75]. The NMR experiments performed on the pure $H_2O@C_{60}$ samples were recorded at temperatures ranging from room temperature to milli-Kelvin temperatures. The higher temperature NMR spectra (5 K$\leq$T$\leq$293 K) were recorded during the joint experiment with Malcolm Levitt's group at the University of Southampton, while the lower temperature NMR spectra (300 mK$\leq$T$\leq$4.2 K) were recorded by myself at the University of Nottingham.

The aim of the NMR experiments is to study the NMR lineshapes, low temperature nuclear spin-isomer conversion and the longitudinal relaxation rate (T_1) of $H_2O@C_{60}$. However, in this chapter, only the lineshape analysis of the NMR experiments is discussed. The low temperature nuclear spin-isomer conversion and T_1 relaxation analysis of the NMR experiments are discussed in Chapter 10. The study of the NMR lineshape could provide insights on the lower energy proton spin interactions of the entrapped H_2O, such as the dipole-dipole interaction, spin-rotation coupling interaction and the spin interaction with the effective local field. The study of these anisotropic spin interactions has to be done at low temperatures because these effects are not observable at higher temperatures due to the averaging of the higher energy spin states. Hence, the lineshape analysis of the milli-Kelvin NMR spectra will be the main subject of this chapter.

Despite not having any built-in shims within the dilution fridge, we are

still able to obtain a good measurements of the lineshape for the following reasons: Firstly, the super conducting magnet in the dilution fridge has a high enough field homogeneity to provide a good lineshape resolution; Secondly, the high signal-to-noise ratio (SNR) obtained from having a high polarisation results in a clearer lineshape.

9.1 Experimental details

There are various technical challenges with performing NMR spectroscopy at milli-Kelvin temperatures. Firstly, the longitudinal relaxation rate (T_1) becomes very long (in the order of minutes to days) when a sample is cooled to temperatures below 1 K [90, 91]. Therefore, each saturation recovery measurement will require a long time to complete, thus resulting in fewer measurement points in each experiment. However, it has proved possible to overcome the long T_1 problem by designing the pulse sequence discussed in the pulse sequence section. Secondly, the dilution fridge takes several hours to cool the sample down to a set temperature and then a further few more hours to have its temperature stabilised. The total length of the cooling process is dependent on the set temperature. The lower the set temperature, the longer it takes for the sample to cool. This is a disadvantage for the nuclear spin-isomer conversion measurements because by the time the sample reaches set temperature, a significant proportion of the ortho-H_2O would have been converted to para-H_2O. Therefore, the initial magnetisation cannot be known.

Similar to the low temperature $H_2O@C_{60}$ INS experiments, the sample is warmed to 65 K for 30 minutes to replenish the ortho-H_2O population before cooling it down rapidly to the set temperature. Due to the sensitivity of the $^3He/^4He$ mixing chamber, the probe has to be lifted away from the mixing chamber into the helium bath before the sample can be warmed to 65 K. After the sample is warmed for 30 minutes, it takes another hour for the probe to be reinserted into the spectrometer before being cooled by the mixing chamber. This further adds to the already lengthy process of cooling the sample to the set temperature. During the process of reinserting the probe into the dilution fridge, the sample is cooled from 65 K to 4.2 K (the temperature at which the nuclear spin-isomer conversion slows down dramatically, see Figure 10.1) in a span of 15 minutes due to the sample being in the helium bath. This is then followed by the cooling of the sample to 1.5 K with the 1 K pot in a span of 5 minutes, before cooling the sample further to the set temperature with the $^3He/^4He$ mixing chamber. It takes

1 hour and 30 minutes to cool from 1.5 K to 1 K; 2 hours and 30 minutes to cool from 1.5 K to 700 mK; 3 hours 30 minutes to cool from 1.5 K to 400 mK and 4 hours to cool from 1.5 K to 300 mK.

The time of the first measurement cannot be used as the origin of the experiment elapsed time[1] ($t_e = 0$) because each experiment takes a different amount of time to cool to the set temperature. To standardise the experiment start time ($t_e = 0$) for each experiment (for comparison purposes), the initial time is set to the moment that the heater is turned off.

The $H_2O@C_{60}$ samples used for the milli-Kelvin NMR experiments are the 90%, 50% and 20% filled samples. These samples are rigorously sublimed and are believed to have a high level of purity. The purpose of studying the samples with different filling factors is to study the effect of the inter-fullerene interactions on the nuclear spin-isomer conversion and its lineshape, as the H_2O in the lower filling factor samples have less neighbouring H_2O to interact with. The 90% filled sample has about 30 mg of material, while the 50% and 20% samples have about 8 mg of material. These amounts of material are inclusive of the empty C_{60} cages. The 90% filled sample is prepared separately by the group at Columbia University and is sublimed by Mark Denning at the University of Southampton, while the 50% and 20% filled samples are both prepared and sublimed by Andrea Krachmalnicoff at the University of Southampton.

All of our NMR measurements performed at the University of Nottingham are conducted on the proton spins. As ortho-H_2O has a total nuclear spin of 1, while para-H_2O has a total nuclear spin of 0, only ortho-H_2O will generate ^{1}H NMR signal. The probe frequency is fixed at around 104.8 MHz and the background magnetic field is set to 2.46T. The deadtime between the pulse and acquisition is set to 14 μs.

9.1.1 Pulse sequence

The goal of the milli-Kelvin experiment's pulse sequence is to measure the change in T_1 and lineshape over the course of the ortho-H_2O to para-H_2O conversion. Due to the change in the population of ortho-H_2O with time, both measurements have to be recorded in conjunction with one another. As explained in the experimental details section, using the usual saturation

[1] Experiment elapsed time (t_e) is the measure of the elapsed time since the start of the experiment ($t_e = 0$). In the case of the $H_2O@C_{60}$ NMR experiments, the experimental elapsed time could last up to 7 days to measure the slow decay of the signal due to the ortho-H_2O to para-H_2O conversion. This should not be confused with t, which is normally used as the elapsed time for the magnetisation recovery (T_1) measurements.

recovery method to measure the T_1 relaxation rate and the 90° acquisition FID is ineffective in the milli-Kelvin temperature regime, as the T_1 of most samples are in the order of minutes to days. Therefore, it will require a very long period of time to complete a T_1 measurement with reasonable number of points. The constantly decaying maximum magnetisation due to the nuclear spin-isomer conversion further suggests that each T_1 measurement has to be completed in a short period of time if meaningful T_1 measurements are to be obtained.

To overcome the aforementioned problems, the pulse sequence illustrated in Figure 9.1.1 is used. This pulse sequence allows all three measurements, the T_1, lineshape and integrated intensity measurements to be recorded in conjunction with one another throughout the duration of the experiment. This allows the study of the effect of the nuclear spin-isomer conversion on T_1, lineshape and integrated intensity (total magnetisation) of the protons in the $H_2O@C_{60}$ sample.

The pulse sequence in Figure 9.1.1 begins with a chain of 90° saturation pulses (saturation comb) to destroy the magnetisation before allowing it to recover its magnetisation. As the magnetisation recovers, a series of small angle acquisition pulses (≈9°) are used to probe the relative magnetisation at different points of the recovery curve without destroying the magnetisation. The size of the small angle pulse is chosen so that only ≈1% of the magnetisation is lost to the signal, which is a negligible amount. Hence, there is no need to saturate the signal and wait for the recovery of the signal before collecting the second point of the recovery curve. Signals with good SNR can still be obtained using the small angle pulses because samples at milli-Kelvin temperatures have high level of polarisation. This also ensures that the measurements of the sample magnetisation inflict minimal distortion to the system. After the magnetisation is fully recovered, the relative signal is expected to decay due to the ortho-H_2O to para-H_2O conversion. After collecting enough points on the T_1 recovery curve, a 90° acquisition pulse is then applied to record the lineshape of the spectrum with good SNR, before repeating the pulse sequence with a saturation comb followed by small angle T_1 measurements.

The length of the small angle T_1 measurements vary with set temperature. The length of the T_1 measurements are set to 4 hours for 1K; 5 hours for 700 mK; 6 hours for 500 mK and 400 mK; 8 hours for 300 mK. Despite the nuclear spin-isomer conversion being measured to have a half-life of 8 hours at temperatures below 1K, a reasonable number of points could still

be obtained to form the "conversion plot"[2] by using the integrated intensities of the fully recovered small angle T_1 spectra to form the conversion plot.

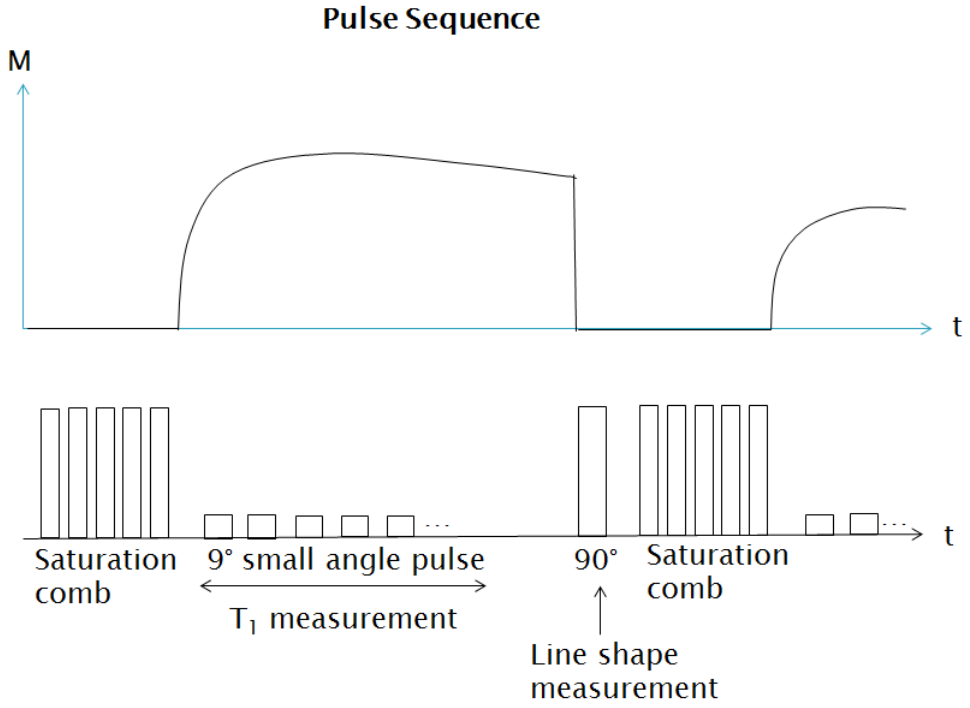

Figure 9.1.1: The pulse sequence used for the milli-Kelvin NMR experiments. The sequence begins with a saturation comb to destroy the magnetisation before applying a series of small angle acquisition pulses (~9°) to measure the relative magnetisation of the recovery curve. This measurement of the recovery curve could be used to measure the T_1. After the magnetisation is fully recovered, the relative signal is expected to decay due to the ortho-H_2O to para-H_2O conversion. A 90° is then applied after completing the measurements of the recovery curve to record the lineshape of the spectrum with good SNR. The sequence is then repeated with a saturation comb followed by small angle T_1 measurements.

[2]Integrated intensity of the spectrum plotted as a function of experiment elapsed time to observe the nuclear spin-isomer conversion rate.

9.2 Spectral lineshape

The study of ^{1}H NMR lineshape allows the probing of the magnetic interactions of the protons. In the case of $H_2O@C_{60}$, the spin Hamiltonian of the proton is expected to be dominated by the dipole-dipole interaction between the two protons in a H_2O molecule. As the sample is prepared in powder form, one would expect the lineshape to resemble a powder Pake pattern. The theory behind the powder Pake pattern is explained in the NMR theory section (Section 2.2.2.1).

Milli-Kelvin NMR experiments have been performed on the three samples with filling factors of 90%, 50% and 20% using the pulse sequence shown in Figure 9.1.1 to probe the T_1, lineshape and nuclear spin-isomer conversion. The 90% filled sample, which has the largest amount of material, is probed at temperatures of 1K, 700 mK and 400 mK; the 50% filled sample is probed at 1 K and 300 mK; while the 20% sample is only probed at 1 K.

The low proton density within the sample combined with a large portion of these proton being NMR silent results in the ^{1}H NMR signal from the probe accounting for a large portion of the detected signal. The proportion of the ^{1}H NMR signal from the probe becomes bigger as samples of lower filling factor are used for the measurement. Separate ^{1}H NMR measurements of the "empty probe" have been done at temperatures in which the samples have been recorded at, before subtracting the empty probe spectra from the respective ^{1}H NMR spectra of the sample.

The time dependence spectra of the 90% filled sample recorded at temperatures of 1 K, 700 mK and 400 mK respectively are illustrated in Figure 9.2.1. These spectra have had the ^{1}H NMR signal from the empty probe subtracted from them. It can be seen that the spectra resemble a powder Pake pattern, which is as expected. The frequency separation of the doublet is measured to be ≈20 kHz, which is 3/5 the size of the intra-molecular proton dipole-dipole coupling constant of H_2O ($\omega_{HH}^{H_2O}$ = 34.5 kHz). The analysis of the doublet separation frequency of the milli-Kelvin ^{1}H NMR spectra is discussed in Section 9.3.3. Besides the doublet, no other structure could be resolved from the spectra. This is due to the large broadening in the line shape. This broadening is attributed to the inter-fullerene interactions between an entrapped H_2O with its neighbouring H_2O. The asymmetry of the doublet is attributed to the chemical shift anisotropy effect, which is likely to be caused by the asymmetric perturbation of the electron density in the C_{60} cage [88, 89]. A similar observation can be seen in the higher temperature ^{1}H NMR spectra of the 90% filled $H_2O@C_{60}$ sample re-

corded at 1.7 K$\leq T \leq$8 K (Figure 9.2.2). The higher temperature spectra were recorded during a joint experiment with our collaborators at the University of Southampton with their 14.1 T NMR spectrometer. Unlike their spectra, our spectra show a higher intensity in the lower frequency peak instead of the higher frequency peak. This is likely to be due to the lack of shims in our NMR system to control the homogeneity of the magnetic field. As the ortho-H_2O converts to para-H_2O, the intensity of both doublet can be seen to decrease at the same rate. As the doublet diminishes, the central "non-decaying" peak becomes more prominent. The recovery time between the saturation and acquisition pulses varies with temperature to take into account the longer T_1 relaxation to ensure that the signal from the H_2O is fully recovered. The recovery times are: 4 hours for 1 K; 5 hours for 700 mK; 6 hours for 400 mK. The recorded change in the intensity of the spectra with respect to experiment elapsed time is discussed in Chapter 10.

The time dependence of the 50% filled sample spectra recorded at 1 K and 300 mK is illustrated in Figure 9.2.3. These spectra have had the ^{1}H NMR signal from the empty probe subtracted from them. The linewidths of the doublet are observed to be narrower than the 90% filled sample spectra in Figure 9.2.1. This is because each entrapped H_2O molecule experiences greater isolation due to having a higher probability of having an empty C_{60} cage next to it. This results in smaller number of inter-fullerene interactions with neighbouring H_2O that causes an increase in the ^{1}H linewidth. This increase in the resolving power has allowed for the structures of the lineshape to be determined. Other than the narrower doublets, the "shoulders" of the Pake doublet and a "dip" that is situated to left of the higher frequency peak (centred at 4 kHz) can be observed in the spectra. This dip is also observed in the ^{1}H NMR lineshape simulations of $H_2@C_{60}$, which are used to compare with the experimental ^{1}H NMR lineshapes of $H_2O@C_{60}$. The asymmetry of the spectra also looked more prominent as compared with the 90% filled sample spectra, with the dip being closer to the higher frequency peak. As ortho-H_2O converts to para-H_2O, the intensities of the doublet, shoulders and dip diminishes, revealing a non-decaying central peak similar to those observed in the 90% filled sample spectra.

The time dependence of the 50% filled sample spectra recorded at 300 mK also revealed a similar feature as the 1 K spectra. The recovery time between the saturation and acquisition pulses for the 300 mK experiment is set to 10 hours, instead of 4 hours in the 1 K experiment. It can be seen that the central peak in the 300 mK spectra is lower relative to the

doublet as compared to the 1 K spectra recorded at similar experiment elapsed time. One obvious example is by comparing the two green spectra ($t_e \approx 3200$ minutes) in Figure 9.2.3. The lower relative central peak of the 300 mK spectra can be attributed to the non-decaying central peak having a different change in T_1 with respect to temperature than the doublet. This suggests that the non-decaying signal may originate from the protonated impurities in the sample, as the T_1 of the protonated impurities is likely to be orders of magnitude larger than the T_1 of the quantum rotor (ortho-H_2O) at milli-Kelvin temperatures. Similar observation can also be seen in the comparison between the 1 K, 700 mK and 400 mK spectra of the 90% filled sample. It is deduced from the T_1 measurement of the 90% filled sample shown in Section 10.4 in the next chapter that the non-decaying signal has a longer T_1 than the decaying signal. It can also be seen that the "inner-shoulder" (centred at -8 kHz) of the lower frequency peak of the 300 mK spectra is larger than the "inner-shoulder" in the 1 K spectra, while the "outer-shoulder" (centred at 23 kHz) of the lower frequency peak of the 300 mK spectra is smaller than the 1 K spectra. These spectral features are explained later in the comparison with the ^{1}H NMR lineshape simulations of $H_2@C_{60}$ section.

The time dependence of the 20% filled sample spectra recorded at 1 K is illustrated in Figure 9.2.4. These spectra have had the ^{1}H NMR signal from the empty probe subtracted from them. The spectrum shows a similar pattern to the one observed in the 50% filled sample spectra, despite having a lower SNR due to having less H_2O in the sample.

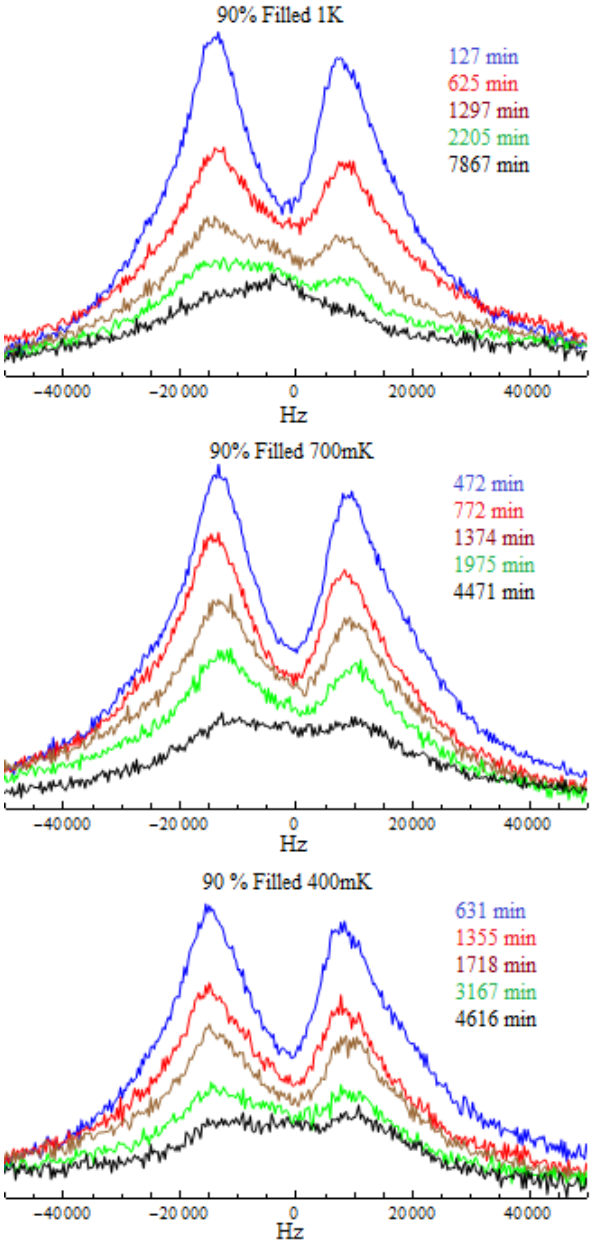

Figure 9.2.1: Time dependence NMR spectra of the 90% filled $H_2O@C_{60}$ sample recorded at 1K, 700 mK and 400 mK respectively. The spectra of all three temperatures have had the ^1H NMR signal from the empty probe subtracted from them. The separation of the doublet is measured to be 20 kHz, which is consistent with the size of the calculated dipole-dipole interaction between the proton spins in H_2O. As the ortho-H_2O converts to para-H_2O, the doublet is seen to decrease in intensity to reveal a non-decaying peak in between the doublet. See text for more details.

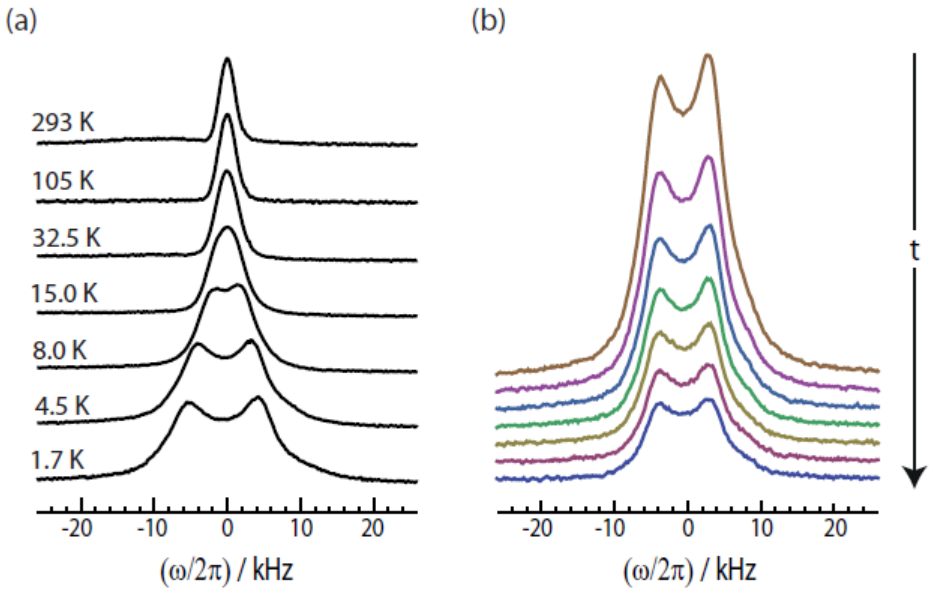

Figure 9.2.2: (a)^{1}H NMR spectra of H_2O @C_{60} from room temperature down to 1.7 K. (b) Time dependence ^{1}H NMR spectra recorded at 5 K with intervals of 2.25 hours. The first recorded spectrum (top) is taken 30 minutes after temperature has reached 5 K from 60 K to allow for the sample to reach thermal equilibrium.

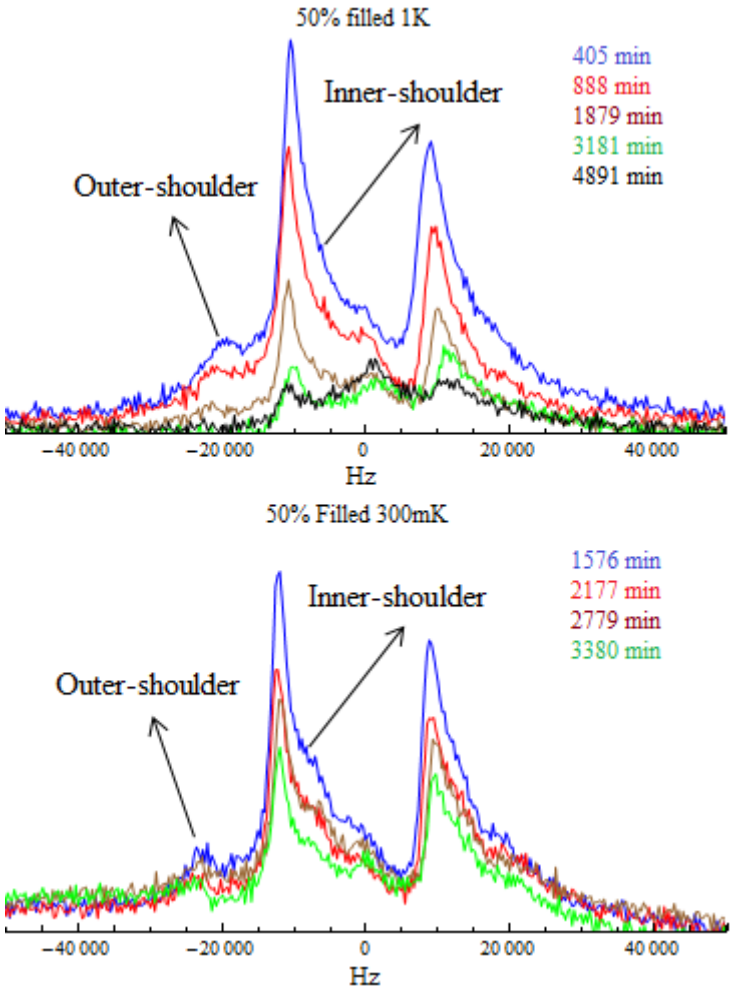

Figure 9.2.3: Time dependence NMR spectra of the 50% filled $H_2O@C_{60}$ sample recorded at 1K and 300 mK respectively. The spectra of both temperatures have had the ^1H NMR signal from the empty probe subtracted from them. The higher resolution lineshape than the lineshape of the 90% filled sample is attributed to higher local field homogeneity due to each H_2O having a lower chance of having a neighbouring H_2O. Narrower doublet, shoulders and a dip can be observed from the spectra. As ortho-H_2O converts to para-H_2O, the intensities of the doublet, shoulders and dip diminishes, revealing a non-decaying central peak similar to those observed in the 90% filled sample spectra.

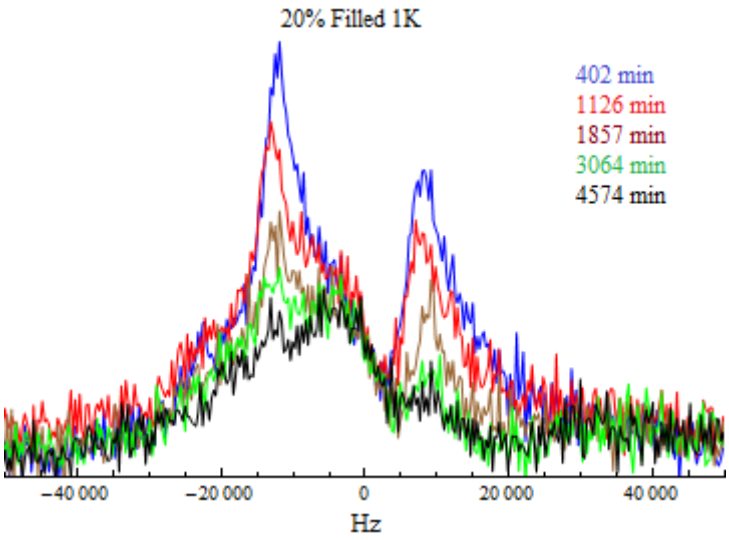

Figure 9.2.4: Time dependence NMR spectra of the 20% filled $H_2O@C_{60}$ sample recorded at 1K and 300 mK respectively. These spectra have had the ^1H NMR signal from the empty probe subtracted from them. The lineshape is similar to those seen in the 50% filled sample spectra (Figure 9.2.3).

The non-decaying signal, such as the central peak, could be discarded by subtracting the spectra by the last spectrum of the experiment ("end spectrum"). This ensures that the lineshape is only composed of signals that decay with time, which are those from $H_2O@C_{60}$. The subtracted 90% filled sample spectra is shown in Figure 9.2.5. The only observable difference in the 90% filled sample spectra is the wider gap in between the doublet due to the absence of the non-decaying central peak. Despite the absence of the non-decaying peak in the 50% and 20% filled sample spectra (shown in Figures 9.2.6 and 9.2.7), the "inner-shoulder" is still observable in the spectra of both samples. This proves that the "inner-shoulder" is the signal from $H_2O@C_{60}$. The "end spectrum" subtracted 20% filled sample spectra also have a lower intensity lower frequency peak as well as having a wider gap in between the doublet than the non-subtracted 20% filled sample spectra in Figure 9.2.4.

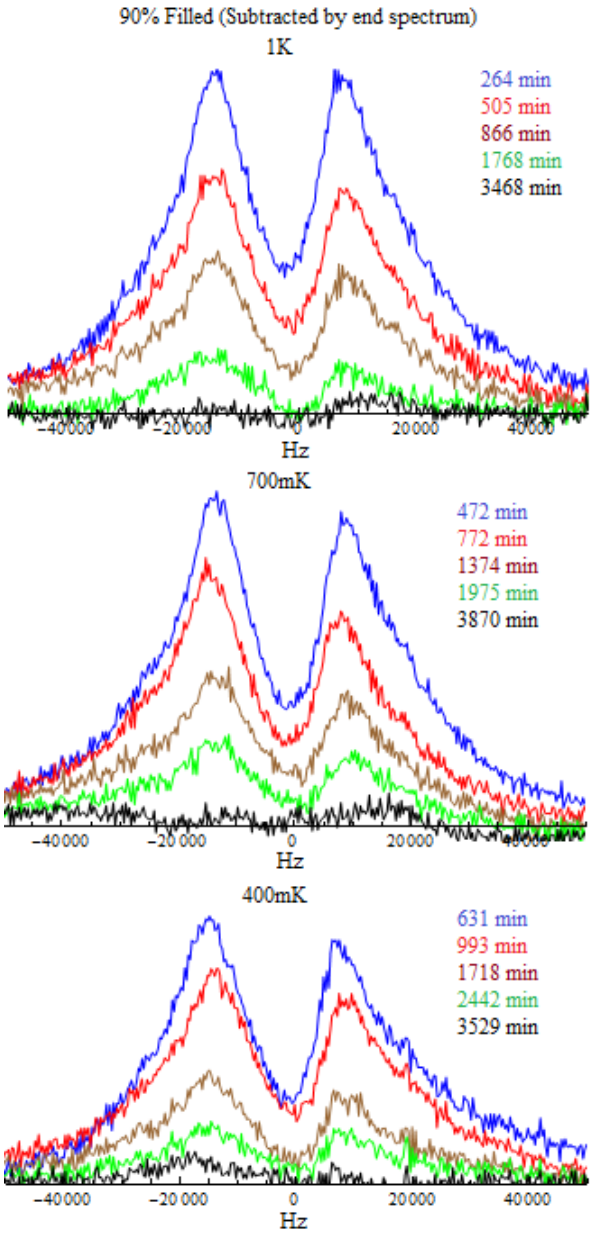

Figure 9.2.5: Time dependence NMR spectra of the 90% filled $H_2O@C_{60}$ sample which have had the long T_1impurity removed by subtracting the spectrum recorded at the longest times. Temperatures of the spectra (top to bottom): 1 K, 700 mK and 400 mK. These spectra are only composed of signals that decay with time, which are those from $H_2O@C_{60}$. There is no observable difference from the non-subtracted spectra other than the wider gap in between the doublet.

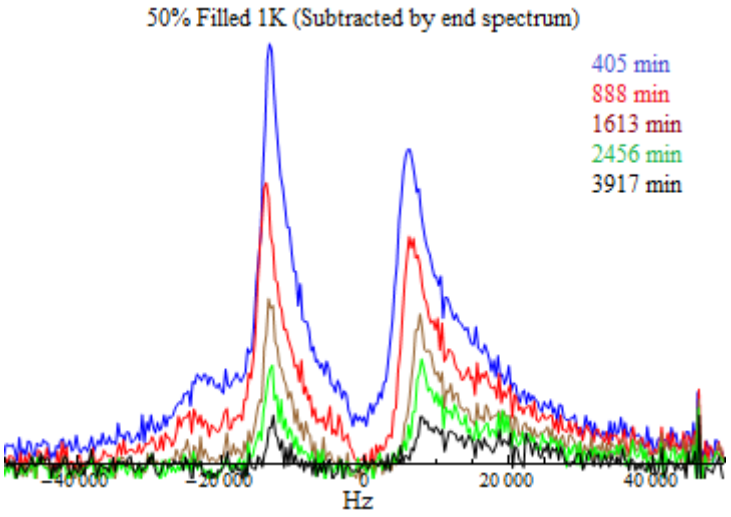

Figure 9.2.6: Time dependence NMR spectra of the 50% filled $H_2O@C_{60}$ sample which are recorded at 1 K and subtracted by the last spectrum of the experiment. There is no observable difference in the non-subtracted spectra other than the wider gap in between the doublet.

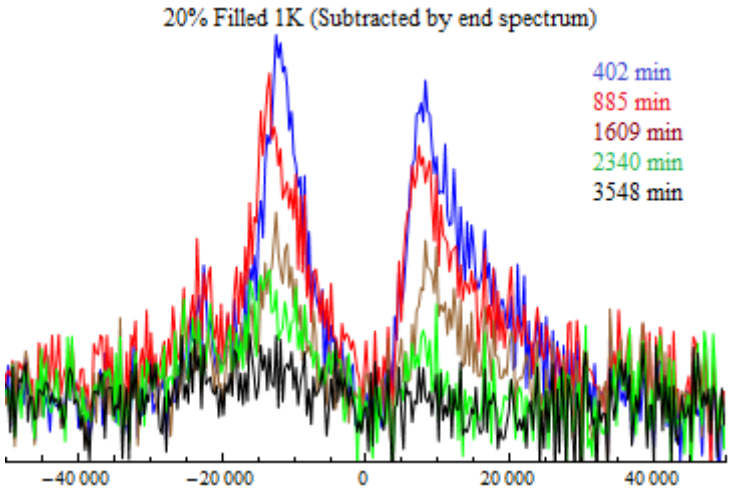

Figure 9.2.7: Time dependence NMR spectra of the 20% filled $H_2O@C_{60}$ sample which are recorded at 1 K and subtracted by the last spectrum of the experiment. There is no observable difference in the non-subtracted spectra other than the wider gap in between the doublet and a lower intensity lower frequency peak.

9.3 Lineshape analysis

The origin of the spectral features such as the aforementioned dip and inner-shoulder (see Figure 9.2.6) can be explained by comparing the experimental lineshape with a simulated NMR lineshape. Theoretical simulations of the NMR lineshape of the $H_2O@C_{60}$ have not been done and is beyond

the scope of my Ph.D.. Therefore, published NMR lineshape simulations of its analogous system, the $H_2@C_{60}$, shall be used as a comparison to the $H_2O@C_{60}$ lineshape recorded at milli-Kelvin temperatures. The NMR lineshape simulations of the $H_2@C_{60}$, which have been undertaken by S. Mamone at the University of Southampton [9], could be used as a good reference to understanding the NMR lineshape of $H_2O@C_{60}$ because both entrapped molecules have identical ortho ground state rotational wavefunction [87] and the spin dynamics of both supramolecular complexes are very similar. Besides having a pair of strongly interacting protons in the cage, both supramolecular complexes couple with their respective crystal fields in their lattices.

The notable differences between the two supramolecular complexes are the weaker H_2O dipole-dipole coupling constant (34.5 kHz as compared to 290 kHz) and the rotational dynamics of their respective entrapped molecules. The weaker dipole-dipole coupling constant of the H_2O is due to the larger separation distance between the two protons, which results in a smaller doublet separation than the H_2 counterpart. Furthermore, the crystal field in the $H_2O@C_{60}$ is generated by the first-order electric dipole and the second-order quadrupole moments, whereas the crystal field in the $H_2@C_{60}$ is only generated by the electric quadrupole moments. However, it is hypothesised in Section 8.3 that there is no coupling between the electric dipole moment of the ortho-H_2O ground state and the crystal field. Hence, the spin dynamics of the ground state of both ortho-H_2 and ortho-H_2O are expected to be dominated by the indirect coupling between the crystal field and the electric quadrupole moment[3].

9.3.1 NMR lineshape simulations of $H_2@C_{60}$

The section discusses the theory and simulations of the ^{1}H NMR lineshapes of $H_2@C_{60}$ undertaken by S. Mamone at the University of Southampton [9]. The spin Hamiltonian of a free ortho-H_2 molecule in its vibrational-rotational-translational ground state is described using the classical rigid rotor approach by Ramsey et al [92, 93]. The Hamiltonian described contains: the Zeeman terms for nuclear spin I and rotational angular momentum J; spin-rotation coupling term; and the dipole-dipole coupling term between the two protons. The spherical notation form of this Hamiltonian is written as:

[3]The crystal field induces an electric dipole moment on the C_{60} cage, which in turn generates an internal electric field within the cage that couples with the electric quadrupole moment of the entrapped ortho-H_2O.

$$H_{I-J} = \omega_H T_0^1(I) + \omega_J T_0^1(J) + \omega_c T^1(I) \cdot T^1(J) + \frac{3}{5}\omega_d T^2(I) \cdot T^2(J) \quad (9.3.1)$$

where T_q^k is the spherical tensor with k and $q = -k, ..., k$ being the rank and component of the tensors; $\omega_H = -\gamma_H B_0$ is the Larmor frequency of the proton with $\gamma_H = 267.513$ MHz T^{-1}; $\omega_J = -\gamma_j B_0$ is the rotational Larmor frequency of H_2 with $\gamma_j = -42.2$ MHz T^{-1}; $\omega_c \approx -715.68$ kHz is the spin-rotation coupling frequency; $\omega_d = \mu_0 \gamma_H^2 \hbar/(4\pi r^3)$ is the dipolar coupling frequency with $\omega_d \approx 1.8623$ MHz for $r = 0.74$ Å. Using the high magnetic field approximation (where Zeeman terms are much larger than the dipolar terms), the above Hamiltonian is then truncated to:

$$H_{I-J} \approx \omega_H T_0^1(I) + \omega_J T_0^1(J) + \omega_c T_0^1(I) \cdot T_0^1(J) + \frac{3}{5}\omega_d T_0^2(I) \cdot T_0^2(J) \quad (9.3.2)$$

The tensors in the above equation are expressed by:

$$T_0^1(\hat{I}) = \hat{I}_z \quad (9.3.3)$$

$$T_0^1(\hat{J}) = \hat{J}_z \quad (9.3.4)$$

$$T_0^2(\hat{I}) = \frac{1}{\sqrt{6}}[T_1^1(\hat{I})T_{-1}^1(\hat{I}) + 2T_0^1(\hat{I})T_0^1(\hat{I}) + T_{-1}^1(\hat{I})T_1^1(\hat{I})] \quad (9.3.5)$$

$$T_0^2(\hat{J}) = \frac{1}{\sqrt{6}}[T_1^1(\hat{J})T_{-1}^1(\hat{J}) + 2T_0^1(\hat{J})T_0^1(\hat{J}) + T_{-1}^1(\hat{J})T_1^1(\hat{J})] \quad (9.3.6)$$

As the ground rotational-translational state of ortho-H_2 has quantum numbers $J = 1$, $L = 0$, and $\Lambda = 1$, where $\Lambda = L + J$, the quantum number J in the above truncated spin Hamiltonian can be replaced directly with Λ for the general description of the angular momentum. This then results in the following equation:

$$H_{I-J} \approx \omega_H T_0^1(I) + \omega_J T_0^1(\Lambda) + \omega_c T_0^1(I) \cdot T_0^1(\Lambda) + \frac{3}{5}\omega_d T_0^2(I) \cdot T_0^2(\Lambda) \quad (9.3.7)$$

The truncated proton spin Hamiltonian of free ortho-H_2 is then used

to construct the full Hamiltonian of H_2 entrapped in C_{60} cage by applying the following effective local quadrupolar field term in the Hamiltonian:

$$H_{Q_\Lambda} = \delta\{T_0^2(\Lambda_P) + \frac{\eta}{\sqrt{6}}[T_2^2(\Lambda_P) + T_{-2}^2(\Lambda_P)]\} \tag{9.3.8}$$

where Λ_P is the angular momentum in the principal axis frame of the interaction; $\delta = V_{ZZ}^{C.-F.}$ is proportional to the size of the crystal field; $\eta = (V_{YY}^{C.-F.} - V_{XX}^{C.-F.})/V_{ZZ}^{C.-F.}$ is proportional to the deviation from the axial symmetry such that $|V_{XX}^{C.-F.}| \leq |V_{YY}^{C.-F.}| \leq |V_{ZZ}^{C.-F.}|$. The tensors in the effective local field Hamiltonian is described as:

$$T_m^2(\Lambda_P) = \sum_{m'=-2}^{2} T_{m'}^2(\Lambda) D_{m',m}^2(\Omega_{L\to P}) \tag{9.3.9}$$

where $\Omega_{L\to P}$ is the set of three Euler angles describing the orientation of the principal axis frame of the local field interaction with respect to the laboratory frame, as the crystal field is dependent on the orientation of the crystalline frame with respect to the background magnetic field.

The nature of the effective local field does not matter in Equation 9.3.8. In the case of $H_2@C_{60}$, it is the electric quadrupolar field generated by the solid packing of nearby entrapped H_2 molecules with non-zero electric quadrupole moments [52, 53, 55]. Molecules with an electric quadrupole moment such as dihydrogen molecules are sensitive to electric field gradients [86]. Furthermore, the molecular spin Λ is also dependent on the local field.

The full Hamiltonian of $H_2@C_{60}$ is obtained by combining the Hamiltonian of the free ortho-H_2 (Equation 9.3.7) and the effective local field Hamiltonian (Equation 9.3.8):

$$\begin{aligned} H_{I-J}(\delta, \eta, \Omega_{L\to P}) \approx\ & \omega_H T_0^1(I) + \omega_J T_0^1(\Lambda) + \omega_c T_0^1(I) \cdot T_0^1(\Lambda) + \\ & \frac{3}{5}\omega_d T_0^2(I) \cdot T_0^2(\Lambda) + \\ & \delta\{T_0^2(\Lambda_P) + \frac{\eta}{\sqrt{6}}[T_2^2(\Lambda_P) + T_{-2}^2(\Lambda_P)]\}. \end{aligned} \tag{9.3.10}$$

Details on solving the full Hamiltonian of $H_2@C_{60}$ (Equation 9.3.10) to obtain the spin resonances of the respective principal axis frame (PAF) orientation with respect to the laboratory frame can be found in S. Mamone's Ph.D. thesis [9]. The resulting spin resonances of all the possible PAF orientation with respect to the laboratory frame is then "powder averaged" over a set of angles with their respective weights to simulate the NMR lineshape of a uniform distribution of crystallites in a $H_2@C_{60}$ powder.

The values of the crystal field variables of $\kappa = \delta/\omega_\Lambda$ and η have been

varied to study the change in the NMR lineshape with respect to these variables. κ is a dimensionless parameter used as a measure for the size of the crystal field relative to ω_Λ. Simulations of the proton NMR lineshapes at 14.1 T and 2 K with different values of κ and η are shown in Figure 9.3.1. The simulations assume that the magnetic quadrupolar field of the protons are acting on their molecular spin Λ in the slow exchange limit, which is more significant than the fast exchange limit at low temperatures. The size of the crystal field, κ, is varied with an upper limit of $\kappa = 600$ to match the maximum size of the splitting observed in INS and FIR experiments (0.2 meV). It is shown that the experimental NMR lineshape of $H_2@C_{60}$ recorded at T= 1.7 K and B= 14.1 T resembles the simulations with $|\kappa| = 2$, $\eta = 0.66$, 1 [9].

9.3.2 Comparing lineshape simulations of $H_2@C_{60}$ with milli-Kelvin lineshape of $H_2O@C_{60}$

The Hamiltonian in Equation 9.3.10 could be used to describe the spin dynamics of $H_2O@C_{60}$ as they have included most of the major spin interactions, including the crystal field interaction with the electric quadrupole moments. By comparing the subtracted spectra of the 50% and 20% filled $H_2O@C_{60}$ samples in Figures 9.2.6 and 9.2.7 to the simulations in Figure 9.3.1, it can be seen that the simulations in the top right corner ($\kappa = 100$, $\eta = 0$ and $\kappa = 600$, $\eta = 0$) shows the strongest resemblance to the experimental lineshape. This is consistent with the fact that $H_2O@C_{60}$ have a larger crystal field than $H_2@C_{60}$ due to H_2O having a permanent electric dipole moment. These simulations contain features which are observed in the experimental lineshape, such as having a dip in between the doublet and a protruding shoulder next to the lower frequency peak. The higher "inner-shoulder" and the lower "outer-shoulder" observed in the 1 K spectra of the 50% filled sample resembles the simulation with $\kappa = 100$, $\eta = 0$; whereas the lower "inner-shoulder" and the higher "outer-shoulder" observed in the 300 mK spectra of the 50% filled sample resembles the simulation with $\kappa = 600$, $\eta = 0$ (see Figure 9.2.3). This can either mean that the ortho-H_2O experiences a larger crystal field or a smaller rotational Larmor frequency (ω_Λ) at lower milli-Kelvin temperatures. As the rotation of the 1^a_{01} state is the result of quantum rotation, ω_Λ is likely to be independent of temperature.

The lack of asymmetry in the lineshape as compared to the experimental lineshape is attributed to the simulations not taking into account

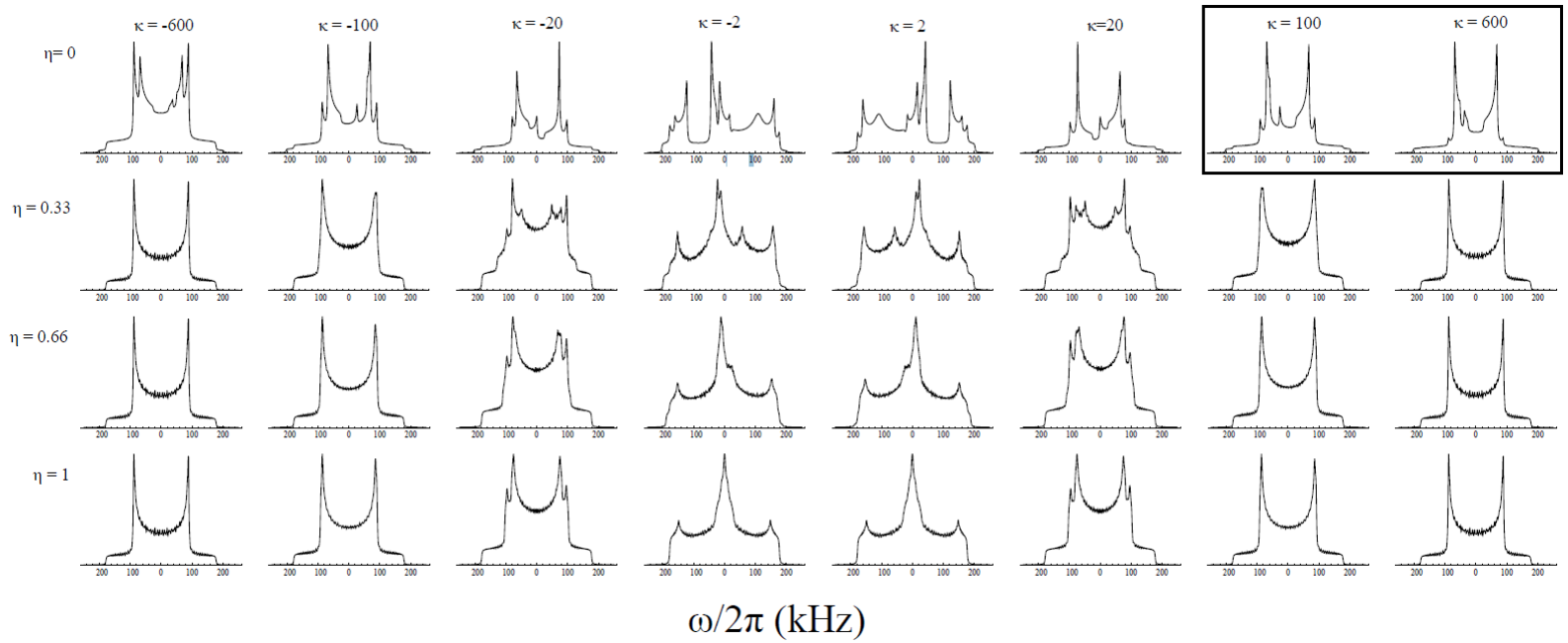

Figure 9.3.1: Simulations of the proton NMR lineshapes of $H_2@C_{60}$ at 14.1 T and 2 K in the presence of the quadrupolar field of the protons acting on their molecular spin Λ in the slow exchange limit. The simulations are obtained by solving the Hamiltonian in Equation 9.3.10 with various values of κ and η. $\kappa = \delta/\omega_\Lambda$ is related to the size of the crystal field, whereas η is related to the biaxiality of the crystal field. The two simulated lineshapes which resemble the observed NMR lineshapes of $H_2O@C_{60}$ are highlighted with a box.

the CSA experienced by the protons due to the C_{60} cage. The lack of resemblance with the simulated lineshapes with higher η suggests that the the crystal field is uniaxial. Therefore, it can be concluded from this comparison that the crystal field interaction with the proton spins in 50% and 20% filled $H_2O@C_{60}$ samples is uniaxial and plays a dominant role in the spin Hamiltonian (high κ value). The linewidth of the 90% filled sample spectra is too broad to be compared with the simulated sample spectra.

The close resemblance of the $H_2O@C_{60}$ spectral lineshape with the simulated lineshape of $H_2@C_{60}$ further suggests that there is no electric dipole interaction with the ground state ortho-H_2O. Ultimately, NMR lineshape simulations of $H_2O@C_{60}$ are required to accurately explain the milli-Kelvin experimental lineshapes. Due to experimental limitations such as the absence of shims in the NMR spectrometer, the interpretation of the milli-Kelvin experimental lineshapes should be done with caution. There is also a possibility of the dip in between the doublet is due to the 14μs of deadtime between the pulse and acquisition. Nevertheless, the milli-Kelvin experimental lineshapes could still be used as a good comparison for the NMR lineshape simulations of $H_2O@C_{60}$ in the future.

9.3.3 Doublet separation frequency

The change in the separation frequency of the Pake doublet with temperature is evident in the temperature dependence spectra of the 90% filled $H_2O@C_{60}$ sample in the higher temperature regime (T$\geq$ 1.5 K) shown in Figure 9.2.2. This increase in the separation frequency is a result of motional narrowing, which is due to less motional averaging of the dipole-dipole coupling as a result of the slower molecular tumbling at lower temperatures. The doublet separation frequency of ortho-H_2O should be a factor of 3/2 the size of its proton dipole-dipole coupling constant ($\omega_{HH}^{H_2O} = 34.5$ kHz) if the two protons remain stationary relative to each other (no rotations or tumbling). However, due to the ortho-H_2O ground state being a quantum rotor with $J = 1$, it continues to rotate even at milli-Kelvin temperatures. Hence, the doublet separation frequency at temperatures low enough for macroscopic rotational ground state occupation should instead be $\frac{3}{5} \times \omega_{HH}^{H_2O}$ due to the quantum averaging over the rotational ground state of ortho-H_2O [9, 75]. According to the Boltzmann statistics, almost all of the ortho-H_2O is expected to occupy the rotational ground state at T$\leq$ 1.5 K. Therefore, the doublet separation frequency should theoretically be equal to the effective dipole-dipole coupling constant, $\omega_{HH,eff}^{H_2O} = \frac{3}{5} \times 34.5$ kHz = 20.4 kHz, for all temperatures below 1.5 K if only the intra-molecular dipole-dipole coupling is considered.

Moving averages are performed on the spectra to reduce the noise before locating the maximum frequency position of the doublet. The separation frequency of the doublet (ν_{sep}) is then obtained by subtracting the maximum frequency position of the lower frequency peak from that of the higher frequency peak. The separation frequency of the doublet of the 90% filled sample spectra recorded at 1 K, 700 mK and 400 mK are plotted against experiment elapsed time (t_e) in Figure 9.3.2. The scattering observed in the plot is the result of the ambiguity in locating the peak maxima due to the broad linewidth seen in the 90% filled sample spectra (see Figure 9.2.5). Nevertheless, the mean values of ν_{sep} can still be used to compare the doublet separation frequencies at different temperatures. There is no observable change in ν_{sep} with respect to t_e. The ν_{sep} as a function of t_e plots for the 50% filled sample recorded at 1 K and 300 mK are illustrated in Figure 9.3.3. The plots from the 50% filled sample have shown less scattering relative to the 90% filled sample. This is because the linewidth of the 50% filled sample spectra are narrower than the 90% filled sample spectra (see Figure 9.2.6), thus resulting in a less ambiguous determination

of the peak's maxima. Similarly small scattering can be seen in the ν_{sep} as a function of t_e plots for the 20% filled sample recorded at 1 K in Figure 9.3.4. The figure compares the ν_{sep} as a function of t_e data for all three samples at 1 K. It can be seen from the ν_{sep} as a function of t_e plots of the 50% and 20% filled samples that the doublet separation frequency increases sharply at $t_e < 54 \times 10^3$ seconds, followed by a period of no change in the doublet separation frequency at $54 \times 10^3 \leq t_e \leq 138 \times 10^3$ seconds, before a second rise in the doublet separation frequency at $t_e > 138 \times 10^3$ seconds.

The mean doublet separation frequency values of the data points that fall within the experiment elapsed time range of $800 < t_e < 2800$ minutes are compiled into Table 9.1. It can be seen from both 90% and 50% filled sample that there is a systematic increase in the doublet separation frequency value with lowering of the temperature. The difference in the doublet separation frequency between the 1 K and 400 mK data of the 90% filled sample is 530 Hz, which is consistent with the 649 Hz difference in the doublet separation frequency between the 1 K and 300 mK data of the 50% filled sample. The difference in the doublet separation frequency between the 90% and 50% filled samples at 1 K is 2 kHz, while the 50% and 20% filled samples show almost identical doublet separation frequencies at 1 K.

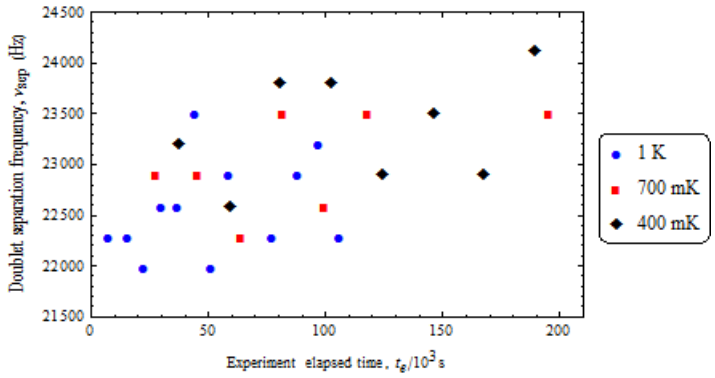

Figure 9.3.2: Doublet separation frequency of the Pake doublet observed in the 90% filled $H_2O@C_{60}$ sample spectra plotted as a function of experiment elapsed time. The scattering of the data points is due to the ambiguity in determining the position of the peak's maxima. The mean doublet separation frequency values of the 1 K, 700 mK and 400 mK data points that fall within the experimental elapsed time range of $48 \times 10^3 < t_e < 138 \times 10^3$ seconds are 22.714 kHz, 22.949 kHz and 23.244 kHz respectively.

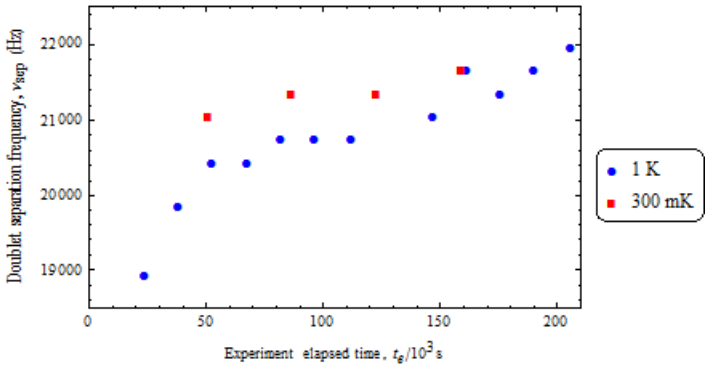

Figure 9.3.3: Doublet separation frequency of the Pake doublet observed in the 50% filled $H_2O@C_{60}$ sample spectra plotted as a function of experiment elapsed time. The scattering of the data points are small relative to the 90% filled sample data. The mean doublet separation frequency values of the 1 K and 300 mK data points that fall within the experimental elapsed time range of $48 \times 10^3 < t_e < 138 \times 10^3$ seconds are 20.713 kHz and 21.362 kHz respectively.

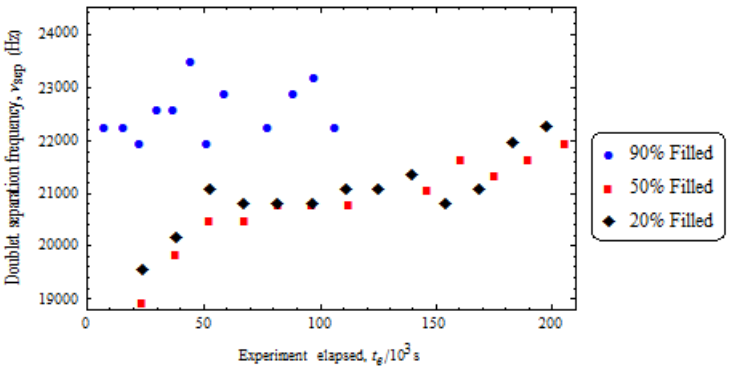

Figure 9.3.4: Doublet separation frequency of the Pake doublet observed in the 90%, 50% and 20% filled $H_2O@C_{60}$ sample spectra recorded at 1 K and plotted as a function of experiment elapsed time. The mean doublet separation frequency value of the 20% filled sample's data points that fall within the experimental elapsed time range of $48 \times 10^3 < t_e < 138 \times 10^3$ seconds is 20.905 kHz.

Mean doublet separation frequencies (800 <t_e<2800 minutes)

Temperature	90% filled	50% filled	20% filled
1 K	22,714 Hz	20,713 Hz	20,905 Hz
700 mK	22,949 Hz	N/A	N/A
400 mK	23,244 Hz	N/A	N/A
300 mK	N/A	21,362 Hz	N/A

Table 9.1: Compilation of the mean doublet separation frequencies of the 90%, 50% and 20% filled $H_2O@C_{60}$ sample spectra recorded at temperatures of 1 K, 700 mK, 400 mK and 300 mK respectively. The mean values are obtained from the averaging of data points that fall within the experimental elapsed time range of $800 < t_e < 2800$ minutes.

The deviation of the mean doublet separation frequencies of the 90% filled sample (≈23 kHz) from the theoretically calculated separation frequency (20.4 kHz) is postulated to be due to the indirect coupling with the crystal field generated by surrounding H_2O. The deviation of the mean doublet separation frequencies of the 90% filled sample from the theoretical value is larger than the 50% and 20% filled samples because the induced electric dipole moment of the C_{60} cage of each ortho-H_2O is larger in the case of the 90% filled sample than the 50% and 20% filled samples. This can be attributed to each ortho-H_2O in the 90% filled sample having more immediate neighbouring para-H_2O than the 50% and 20% filled samples.

The increase in the doublet separation frequency with lowering of the temperature may be attributed to one of the following two postulate: (1) The proton separation distance decreases with temperature. This is because there isn't any other source of averaging other than the quantum averaging at $T < 1.5$ K, as all of the ortho-H_2O would have occupied the rotational ground state, while the energy of the rotational ground state is independent of temperature. Thus, the only explanation to the increase in the dipole-dipole coupling strength is the increase in the dipole-dipole coupling constant, which is dependent on the distance between the two nuclear dipoles (see Equation 2.2.1). (2) The protons in the ortho-H_2O experience higher electric field from the surrounding para-H_2O at lower temperatures. This is a more plausible reason as it is consistent with the deduction obtained from the comparison between the observed 1 K and 300 mK 50% filled sample spectra and the simulated $H_2@C_{60}$ lineshapes (Section 9.3.2).

The increase in the doublet separation frequency with time observed at the early period of the ν_{sep} as a function of t_e plots of the 50% and 20% filled samples in Figure 9.3.4 is postulated to be due to the increase in the

size of the crystal field with time as a result of an increase in the population of the surrounding para-H_2O due to nuclear spin-isomer conversion. This increase in the size of the crystal field would then results in an increase in the size of the coupling with the electric quadrupole moment of ortho-H_2O. The result in Figure 9.3.4 also suggests that the range of the indirect electric dipole-quadrupole coupling is longer than the distance between two neighbouring C_{60}.

In the case of the 90% filled sample, the observed time independent doublet separation frequency in Figure 9.3.4 is postulated to be due to the induced electric dipole moment of the C_{60} cage of each ortho-H_2O having reached saturation since the beginning of the conversion experiment. This is likely due to each ortho-H_2O having immediate neighbouring para-H_2O from the beginning of the conversion experiment as compared to the 50% and 20% filled samples. As a result, the electric dipole moment of the C_{60} cage of each ortho-H_2O is strongly induced by the electric dipole moment of these immediate neighbouring para-H_2O. Therefore, the induced electric dipole moment of the C_{60} cage of each ortho-H_2O remains largely the same despite experiencing a larger electric field at the later period of the experiment. This postulate also explains the null change in the splitting of the ortho-1_{01} state with respect to conversion as observed in the INS spectra of the 90% filled sample (Figure 8.1.1), where the splitting of the ortho-1_{01} state is postulated to be due to the breaking of the cage symmetry by the crystal field.

The second rise in the doublet separation frequency seen at the end of the ν_{sep} as a function of t_e plots of the 50% and 20% filled samples may be attributed to the low SNR due to the loss of NMR signal from conversion.

9.4 Conclusions

The milli-Kelvin ^{1}H NMR spectra of the 90%, 50% and 20% filled $H_2O@C_{60}$ samples have revealed a doublet which resembles the powder Pake pattern. There is no observable change in the lineshape with respect to temperature for all three samples. The time dependent spectra of all three samples have shown systematic decay in the intensity of the doublet over the course of a few days. This decay is due to the ortho-H_2O to para-H_2O conversion at low temperatures. A non decaying central peak is revealed at the end of the experiment when most ortho-H_2O have been converted to para-H_2O. This non-decaying central peak has a much longer T_1 than decaying doublet, thus it is believed to originate from the protonated impurities in the sample and it could be removed from the analysis by subtracting a spectrum recorded at very long times after initial cooling. These "end-subtracted" spectra shows only the decaying signal, which is certain to originate from the $H_2O@C_{60}$. The broader lineshape seen in the spectra of the 90% filled sample is due to large number of inter-fullerene couplings with neighbouring H_2O. The narrower lineshape of the 50% and 20% filled sample spectra have revealed structures other than the doublet. These structures include a protruding "outer-shoulder" and an "inner-shoulder" on each sides of the lower frequency peak, and a dip in between the doublet.

As there are no NMR lineshape simulations of the $H_2O@C_{60}$ to date, the published NMR lineshape simulations of $H_2@C_{60}$ is used as a reference to understand the structure of the experimental NMR lineshape of $H_2O@C_{60}$ instead. Two of the simulated $H_2@C_{60}$ lineshape have shown strong resemblance to the experimental NMR lineshape of 50% and 20% filled $H_2O@C_{60}$ samples. These two simulations assume a large uniaxial crystal field, which is consistent with H_2O having a larger electric dipole moment than H_2, thus generating a larger electric field in the crystal, while the uniaxiality of the crystal field suggests that the electric dipole moments in the 50% and 20% filled sample are cooperatively aligned to form ferroelectricity. It is also concluded from the comparison between the experimental and simulated lineshapes that the size of the crystal field is larger at lower milli-Kelvin temperatures.

The analysis of the doublet separation frequency of the end-subtracted spectra has shown temperature, fill factor and time dependent doublet separation frequency at $T \leq 1.5$ K. It is deduced that the increase in the doublet separation frequency with respect to the decrease in temperature at $T \leq 1.5$ K is likely due to the increase in the size of the crystal field with

lower temperatures. Similar deduction is also made from the comparison between the experimental and simulated lineshape.

The increase in the doublet separation frequency with respect to conversion in the 50% and 20% filled samples is deduced to be due to an increase in the size of the crystal field as the population of para-H_2O increases as a result of conversion. This result further strengthens the postulate that only para-H_2O possess an effective electric dipole moment that contributes to the crystal field, while ortho-H_2O does not have an effective electric dipole moment.

As the electric field experienced by the C_{60} cage of each ortho-H_2O is much stronger in the case of the 90% filled sample, it is deduced that the induced electric dipole moment of the C_{60} cage of each ortho-H_2O has reached its saturation value since the beginning of the conversion experiment. This explains the time independent doublet separation frequency observed in the NMR spectra of the 90% filled sample. This also explains the null change in the size of the splitting of the ortho-1_{01} state with respect to conversion as observed in the INS spectra of the 90% filled sample (Figure 8.1.1). Therefore, based on conclusion made on the relation between the NMR doublet separation frequency and the splitting of the ortho-1_{01} state, it is interesting to see if there is an increase in the size of the ortho-1_{01} state splitting with respect to conversion in the 50% and 20% filled samples. This can be done by performing an INS investigation on the 50% and 20% filled samples.

The study of the low temperature proton NMR spectral lineshape of $H_2O@C_{60}$ have shown that the electric dipole moment of H_2O strongly influences the lineshapes of the NMR spectra. By analysing the spectra, we are able to determine several significant properties of the $H_2O@C_{60}$, such as the zero effective electric dipole moment of the ground state ortho-H_2O, uniaxial crystal field in the 50% and 20% filled samples, and the dependence of the crystal field strength with temperature. However, NMR lineshape simulations of $H_2O@C_{60}$ are still needed to fully explain the structure observed in the milli-Kelvin NMR lineshapes. Due to experimental limitations such as the absence of shims in the milli-Kelvin NMR spectrometer, the interpretation of the milli-Kelvin experimental lineshapes should to be done with caution. Nevertheless, the experimental milli-Kelvin NMR spectra could still serve as a good reference for the NMR lineshape simulations of $H_2O@C_{60}$ in the future.

Chapter 10

Low temperature nuclear spin-isomer conversion in $H_2O@C_{60}$

Preliminary studies on $H_2O@C_{60}$ with FIR, INS and NMR spectroscopy have revealed that the proton spins in $H_2O@C_{60}$ undergo nuclear spin-isomer conversion from ortho-H_2O to para-H_2O over a long period of time ($\sim$ 8 hours half-life) at T$<$ 20 K [75]. This has led to further investigation on this naturally occurring ortho-H_2O to para-H_2O nuclear spin-isomer conversion at low temperatures in the absence of catalysts in the hope of understanding the nuclear spin-isomer conversion mechanism. This chapter is dedicated to discussing the experimental results on the ortho-H_2O to para-H_2O conversion rate with respect to temperature. The recording of the ortho-H_2O to para-H_2O conversion rate in this chapter are done with NMR and INS spectroscopy on the purified $H_2O@C_{60}$ samples. The aim of these experiments is to understand the mechanism behind this nuclear spin-isomer conversion, which could potentially be used to selectively convert triplet nuclear spin states to singlet nuclear spin state for storage of the nuclear spin polarisation. This is because singlet states are long-lived nuclear spin states (LLS) with extended relaxation times exceeding the T_1 relaxation time by more than an order of magnitude [94, 95, 96, 97, 98, 99, 100, 101, 102].

The results of the nuclear spin-isomer conversion is demonstrated through the plotting of the integrated intensities of the signal with respect to time. In NMR spectroscopy, only the decay of the signal from ortho-H_2O can be recorded; whereas in INS, both decay and growth of the signals from ortho-H_2O and para-H_2O respectively can be recorded. As with the other low

temperature experiments on $H_2O@C_{60}$, the samples have to be warmed at high temperatures to populate the ortho-H_2O species, before rapidly cooling the sample down to set temperatures to begin the experiments.

The ortho-H_2O to para-H_2O conversion investigation using NMR spectroscopy have been collaboratively performed by our group at the University of Nottingham and M. H. Levitt's group at the University of Southampton [88]. Our group does the 4.2 K NMR experiments and the milli-Kelvin NMR experiments, while Levitt's group does the higher temperature NMR experiments (5 K$\leq$T$\leq$15 K), in which I have also participated during my stay in Southampton. Besides ^{1}H NMR spectroscopy, we have also used ^{13}C NMR spectroscopy to study the dependence of ortho-H_2O to para-H_2O conversion on the nuclear spins of ^{13}C at the University of Southampton. Both ^{1}H and ^{13}C NMR investigation of $H_2O@C_{60}$ at higher temperature (5 K$\leq$T$\leq$15 K) will also be discussed in this chapter.

10.1 Higher temperature nuclear spin-isomer conversion (4.2 K≤T≤15 K)

10.1.1 ^{1}H NMR

The experiments recorded at T≥5 K were recorded at 14.1 T using a Bruker AVANCE-II + spectrometer in Southampton while the 4.2 K experiment is recorded at 0.86 T using the field-cycling NMR spectrometer in Nottingham. Only the 90% filled $H_2O@C_{60}$ samples were used in the study of the higher temperature experiment. The aim of this experiment is to study the temperature dependence of the nuclear spin-isomer conversion in the temperature range of 4.2 K≤T≤15 K.

The ^{1}H NMR experiments performed in Southampton began with equilibrating the sample at 50 K for a few hours before cooling it down to set temperatures in approximately 30 minutes. The sample temperature is then maintained over several hours to record the NMR signals before warming the sample to 32.5 K for a few hours to study the back conversion. The NMR signals are recorded with time intervals of 180 seconds throughout the experiment using the saturation-recovery procedure. The T_1 relaxation rate of the sample at 5 K is measured to be 3 seconds.

The plot of the integrated intensity of the ^{1}H NMR spectra as a function of time recorded over the course of 12 hours is illustrated in Figure 10.1.1. The plot demonstrates the ortho-H_2O to para-H_2O conversion at 5 K and para-H_2O to ortho-H_2O back-conversion at 32.5 K . It can be seen from the plot that the signal's integrated intensity increases rapidly as the sample is being cooled to 5 K. This rapid increase in signal is not due to the increase in population of the ortho-H_2O, but due to the Curie law for nuclear magnetisation. After the temperature has stabilised at 5 K, the integrated intensity is seen to decay over time due to the loss of ortho-H_2O population as they convert to para-H_2O (NMR silent). After recording the decay of the signal for 10 hours at 5 K, the sample is then warmed and equilibrated at 32.5 K. The integrated intensity decreases as the sample is warmed to 32.5 K. This is again due to the Curie law for nuclear magnetisation. After the temperature has stabilised at 32.5 K, the integrated intensity then begins to increase over time. This increase in intensity is the result of para-H_2O converting to ortho-H_2O due to the population redistribution of the H_2O to occupy the higher energy states.

Similar experimental procedures have been done to measure the conversion from ortho-H_2O to para-H_2O at 10 K and 15 K. The plot of the

integrated intensity of the 5 K, 10 K and 15 K conversion as a function of time is shown in Figure 10.1.2(a) for comparison. The data does not fit well to a single exponential decay. The misfit with the single exponential decay equation is illustrated in the 4.2 K integrated intensity as a function of time plot in Figure 10.1.3(a). This result differs to the single exponential decay observed in previous studies of spin-isomer conversion for H_2O in inert gas matrices [103]. However, the data does show good fit to the second-order kinetic equation (Equation 10.1.3, red line). Figure 10.1.2(b) shows the data, which is transformed with Equation 10.1.4 to provide linear plots for the second-order kinetic. The derivation of the second-order kinetic equation is discussed in the nuclear spin-isomer conversion kinetics section (Section 10.1.2). It can be seen from the fit that the integrated intensity decays to a higher baseline when the experiment is recorded at a higher equilibrium temperature. This is because the equilibrium population of the ortho-H_2O is higher at higher temperatures.

In the case of the 4.2 K experiment done in Nottingham, the sample is equilibrated at 50 K for 30 minutes before rapidly cooling the sample down to 4.2 K in 12 minutes. The T_1 relaxation rate of the sample at 4.2 K is measured to be 3 seconds. The integrated intensity of the spectra is recorded every 2 minutes over a period of 48 hours using the saturation-recovery procedure. The integrated intensity of the ^1H NMR signal plotted as a function of time is illustrated in Figure 10.1.3. Due to the longer duration of the 4.2 K conversion experiment as opposed to the higher temperature experiments done at the University of Southampton, the data is able to be fitted to a higher degree of confidence. It can be seen that the data does not fit well with the single exponential decay (grey dotted line) as opposed to the second kinetic equation (red line). The data in Figure 10.1.3(a) has shown that the decay is too steep at the beginning and too slow at the end to be a single exponential decay. A separate measurement of the empty probe has been done after the experiment to measure the background signal from the probe and it is deduced that the last spectrum of the experiment still contain signal from the sample. Similar results could be seen from the linear fit of the transformed data to the second-order kinetics.

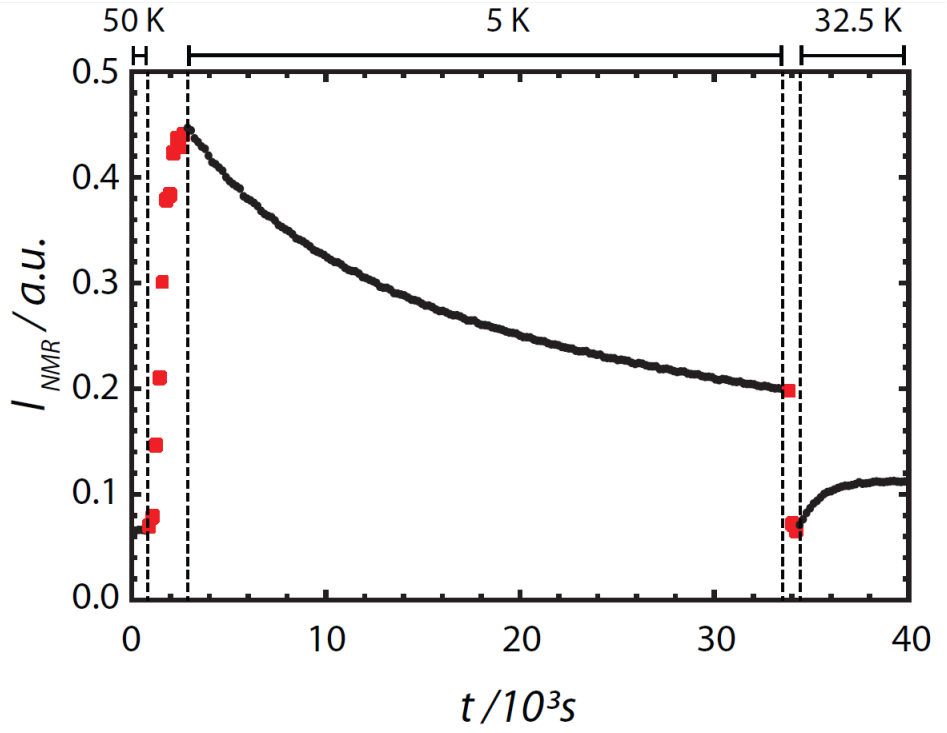

Figure 10.1.1: Integrated intensity of the ^{1}H NMR signals (I_{NMR}) of $H_2O@C_{60}$ as a function of time, recorded to investigate the ortho-H_2O to para-H_2O conversion at 5 K and para-H_2O to ortho-H_2O back-conversion at 32.5 K. The experiment begins with populating the ortho-H_2O at 50 K before cooling the sample down to 5 K to record the low temperature ortho-H_2O to para-H_2O conversion. The increase in the signal during the cooling of the sample is due to Curie law of nuclear magnetisation. After monitoring the decay of the signal at 5 K for 10 hours, the sample is warmed to 32.5 K to record the back-conversion from para-H_2O to ortho-H_2O. The signals are recorded at time intervals of 180 seconds throughout the experiment using the saturation-recovery procedure to ensure a well-controlled nuclear magnetisation. Integrated intensities of the NMR signals recorded at constant temperature are shown as black dots, while the integrated intensities recorded during the change in temperature are shown as red dots.

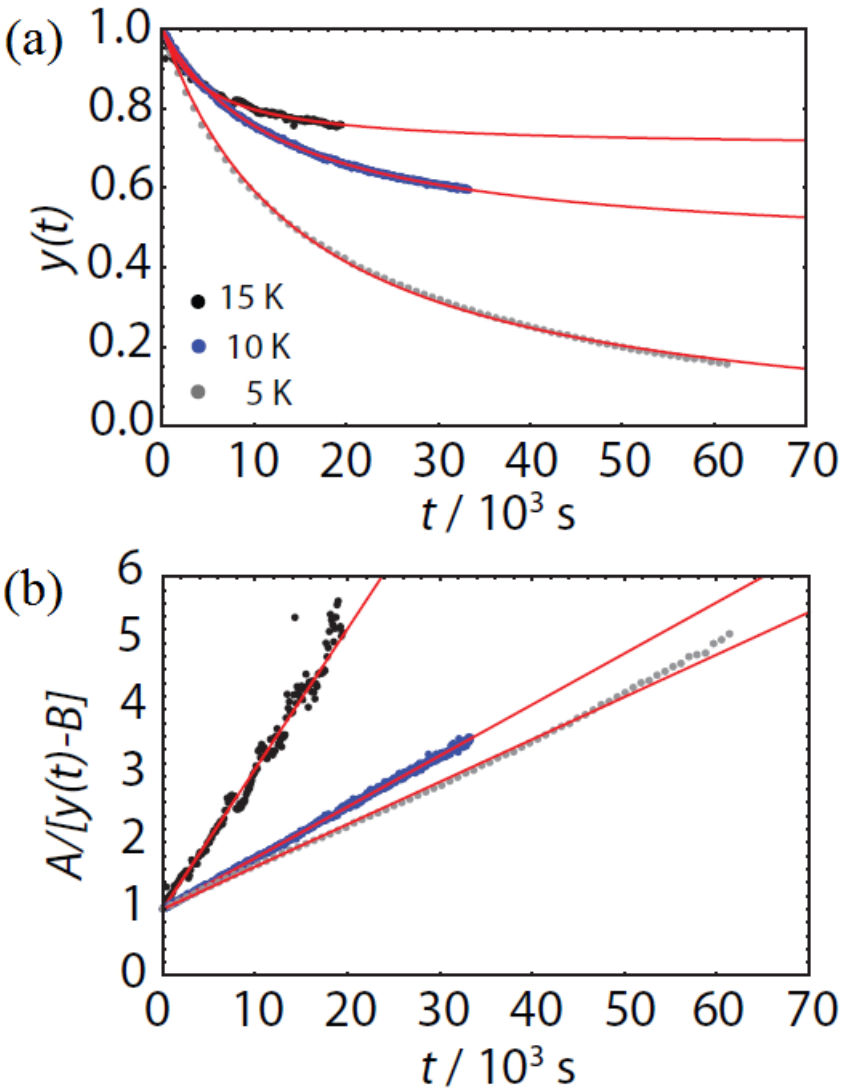

Figure 10.1.2: (a) Integrated intensity of the ^{1}H NMR signals of $H_2O@C_{60}$ as a function of time recorded at equilibrium temperatures of 5 K (grey dots), 10 K (blue dots) and 15 K (black dots) respectively after cooling the sample from 60 K. The 5 K data is identical to the data shown in Figure 10.1.1. The red lines are the second-order kinetic equation fit (Equation 10.1.3) to the respective data. (b) Data transformed with Equation 10.1.4 to provide linear plots for the second-order kinetics. The signals are recorded at time intervals of 60 seconds throughout the 10 K and 15 K experiments using the saturation-recovery procedure.

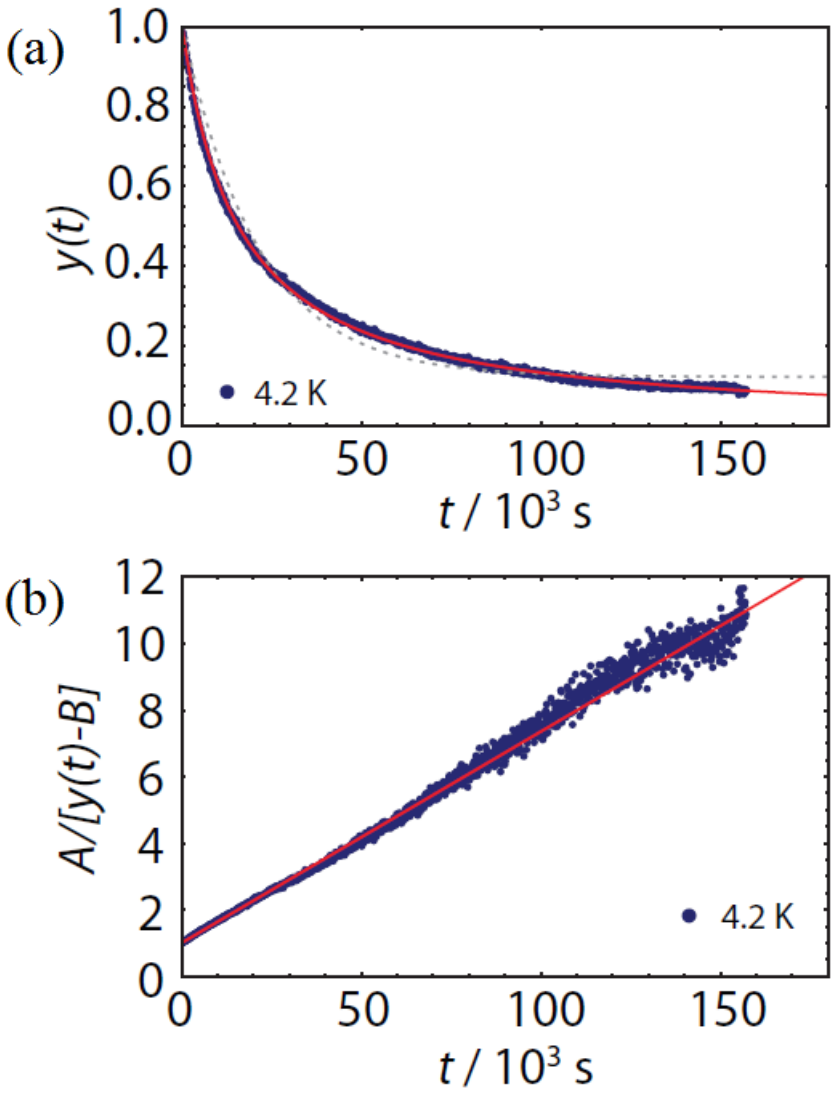

Figure 10.1.3: (a) Integrated intensity of the ^{1}H NMR signals of $H_2O@C_{60}$ as a function of time recorded at equilibrium temperatures of 4.2 K. The sample is equilibrated at 50 K for 30 minutes before cooling to 4.2 K. The integrated intensity of the spectra is recorded every 2 minutes over a period of 48 hours using the saturation-recovery procedure. The red line is the second-order kinetic fit to the data, while the grey dotted line is the first-order kinetic fit (single exponential decay) to the data. (b) The conversion data transformed with Equation 10.1.4 to provide the linear plot for the second-order kinetic.

10.1.2 Nuclear spin-isomer conversion kinetics

The low temperature nuclear spin-isomer conversion of $H_2O@C_{60}$ shows second-order kinetic behaviour, which involves two identical reactants to cause a reaction (in this case two ortho-H_2O). The second-order conversion process can be described with the following rate equation:

$$\frac{d\Delta\Phi(t)}{dt} = -k_2\Delta\Phi(t)^2 \tag{10.1.1}$$

where k_2 is the second-order rate constant and $\Delta\Phi(t) = \Phi(t) - \Phi_{eq}$ is the deviation of the instantaneous ortho fraction ($\Phi(t)$) from its equilibrium population (Φ_{eq}) at sample temperature. The solution of the rate equation is written as:

$$\Delta\Phi(t)^{-1} = \Delta\Phi(0)^{-1} + k_2 t \tag{10.1.2}$$

where $\Delta\Phi(0)^{-1}$ is the initial deviation of ortho fraction from equilibrium. The ^{1}H NMR signal ($I_{NMR}(t)$) is proportional to $\Phi(t)$ at constant temperature. Normalising I_{NMR} with $I_{NMR}(0)$ will then lead to the following relation:

$$y(t) = A(1 + \kappa t)^{-1} + B \tag{10.1.3}$$

where $y(t) = I_{NMR}(t)/I_{NMR}(0))$, $A + B = 1$, $A = \Delta I_{NMR}(0)/I_{NMR}(0)$, $B = \Phi_{eq}/\Phi(0)$ and $\kappa = \Delta\Phi(0)k_2$. This equation describes the second-order kinetic decay of the normalised signal over time, and is used to fit (shown as red line) the integrated intensity as a function of time data shown in Figures 10.1.2(a) and 10.1.3(a). The independent parameters A and κ are allowed to float with constraint $B = 1 - A$ to obtain the best fits. The rearrangement of Equation 10.1.3 into:

$$\frac{A}{y(t) - B} = \kappa t \tag{10.1.4}$$

can be used to transform the data ($A/(y(t) - b)$) to be linearly dependent with time, with κ acting as the slope of the straight line. The linear fit of the transformed data is shown in Figures 10.1.2(b) and 10.1.3(b). The parameters A and κ are adjusted to ensure that the transformed data is plotted as a straight line, before fitting with Equation 10.1.4 to obtain the slope κ. The second-order rate constant k_2 can be estimated from the the slope parameter κ using the equation $k_2 = \kappa/\Delta\Phi(0) = \kappa/[A\Phi(0)]$, where $\Phi(0)$ is the initial deviation of the ortho fraction from equilibrium population at $t = 0$, where $t = 0$ is the moment when ortho-H_2O begins converting to para-H_2O. However, the initial deviation is hard to estimate as it takes several tens of minutes for the sample to cool and the temperature to stabilised. Furthermore, the conversion rate is unknown during the cooling process. Therefore, the $\Phi(0)$ is estimated to between 0.5 and 0.7, with an upper value that corresponds to the thermal equilibrium at

the temperature before cooling of the sample.

The results of the fitting parameters and the estimated k_2 value with their respective confidence level is shown in Table 10.1. The conversion rates at $T \leq 10$ K is shown to be very much slower than the conversion rate at 15 K. The conversion rate does not show any dependence on the magnetic field strength. The increase in parameter A with lowering of temperature is the result of the lower baseline seen in the lower temperature integrated intensity versus time plots in Figure 10.1.2(a).

T/K	B/T	$\kappa/(10^{-3}\ s^{-1})$	A	$k_2/(10^{-3}\ s^{-1})$
15	14.1	210 ± 10	0.30 ± 0.02	1200 ± 250
10	14.1	77 ± 3	0.56 ± 0.01	230 ± 50
5	14.1	64 ± 2	1.04 ± 0.03	100 ± 20
4.2	0.86	63 ± 2	1.00 ± 0.01	105 ± 20

Table 10.1: Table showing the fitting parameters obtained from the fitting of the integrated intensities as a function of time plots in Figures 10.1.2(b) and 10.1.3(b) using Equation 10.1.4. k_2 is obtained by using the $k_2 = \kappa/[A\Phi(0)]$ relation, with $\Phi(0)$ estimated to be $0.5 \leq \Phi(0) \leq 0.75$.

10.1.3 ^{13}C NMR

The mechanism behind the low temperature nuclear spin-isomer conversion has initially been postulated to originate from the ^{13}C nuclei of the C_{60} cages. Despite the evidence in the previous section indicating a dominant second-order kinetic behaviour (reaction between two ortho-H_2O) in the nuclear spin-isomer conversion process, it remains interesting to see if the ^{13}C nuclei have a role in the conversion process as well. It can be calculated from the 1.07% natural abundance of the ^{13}C nuclei that 48% of the C_{60} cages contain at least one ^{13}C nuclei.

The effect of the ^{13}C on the nuclear spin-isomer conversion process can be measured by using Hartmann-Hahn cross-polarisation (CP) method to transfer magnetisation from the ortho-H_2O to the ^{13}C in the C_{60} cage before measuring the ^{13}C NMR signal. Through this method, the decay of the nuclear magnetisation of the ortho-H_2O with at least one ^{13}C nuclei in its cage can be observed. The ortho-H_2O without a ^{13}C nuclei in its cage will not have its nuclear magnetisation transferred to a ^{13}C nuclei. Therefore, the measured ^{13}C NMR signal are derived exclusively from the ^{13}C nuclei in the C_{60} cages with an encapsulated ortho-H_2O in it.

The pulse sequence of the ^{13}C NMR is illustrated in Figure 10.1.4. The pulse sequence begins with a chain of 90° pulses to saturate the ^{1}H magnetisation, followed by a τ delay to allow the magnetisation to recover. A 90° flip angle is then applied onto the proton spectra after the delay, followed by the respective "spin-locking" pulses for both ^{1}H and ^{13}C nuclei with a pulse width of τ_{cp} before acquiring the FID from the ^{13}C nuclei without proton decoupling. The frequency of the spin-locking pulses for the ^{1}H and ^{13}C nuclei are chosen to have their respective Larmor frequencies in the rotating frame matches ($\omega^{H}_{rot} = \omega^{C}_{rot} = \gamma_{H} B^{H}_{rot} = \gamma_{C} B^{C}_{rot}$, where B^{H}_{rot} and B^{C}_{rot} are the respective applied field of the spin-locking pulses).

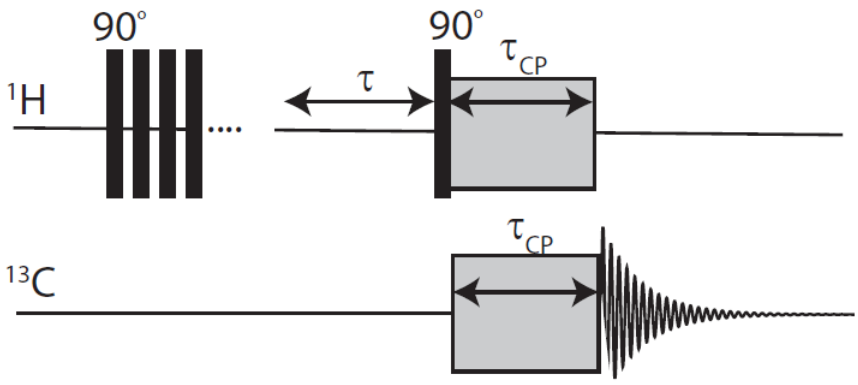

Figure 10.1.4: Pulse sequence used to measure the ^{13}C NMR signal via Hartmann-Hahn cross-polarisation method to transfer magnetisation from the ortho-H_2O to the ^{13}C in the C_{60} cage. The pulse sequence begins with a chain of 90° pulses to saturate the ^{1}H magnetisation, followed by a τ recovery delay, then followed by a 90° pulse, then the respective spin-locking pulses on both ^{1}H and ^{13}C nuclei for a duration of τ_{CP} to transfer the ^{1}H polarisation to the ^{13}C nuclei before acquiring the ^{13}C signal.

The spectra recorded with τ_{CP} of 1 ms, 5 ms and 10 ms at 5 K are illustrated in Figure 10.1.5(a). The lineshape of the spectra is the result of CSA from the C_{60} molecule [50, 104]. This lineshape resembles the simulated lineshape illustrated in Figure 10.1.5(b), which is based on the CSA principal values with a biaxiality of 0.28. The ^{13}C CSA tensors in C_{60} can be visualised as an ellipsoid with the long axis parallel to the cage radii (Figure 10.1.5(c)). At 5 K, the quantum wavefunction is localised at the centre of the cage. Therefore, the angle θ_{CH} between the ^{1}H-^{13}C inter-nuclear vector and the external magnetic field (see Figure 10.1.5(c)) is subtended by the radial vector from the centre of the cage to the ^{13}C.

The $\tau_{CP} = 1$ ms spectrum shows a dip in the lineshape region around the isotropic chemical shift value of 143 ppm. The dip in the lineshape

disappears when τ_{CP} is increased to 5 ms and 10 ms. When short τ_{CP} is applied, the transfer polarisation range is short. Therefore, the ortho-H_2O can only transfer its ^{1}H magnetisation to the ^{13}C of the same C_{60} cage. This is evident from the dip in the τ_{CP}= 1 ms spectrum around the isotropic chemical shift frequency value, which is composed of signal from ^{13}C that are at an angle θ_{CH} close to the magic angle $\theta_m = \arctan\sqrt{2}$. This strong loss of spectral intensity around the isotropic chemical shift frequency value is attributed to the lack of CP magnetisation transfer from the ^{1}H to the^{13}C nuclei due to the inter-nuclear vector being close to θ_m (see Figure10.1.5(b) and (c)), which results in no dipole-dipole coupling between the ^{1}H and ^{13}C nuclei. As longer τ_{CP} is applied, the ^{1}H polarisation transfer range is also increased. Hence, the ortho-H_2O is able to transfer its ^{1}H magnetisation to the ^{13}C nuclei of its neighbouring cages. This results in the ^{13}C at angle $\theta_{CH} = \theta_m$ being able to receive ^{1}H magnetisation from the ortho-H_2O of a different cage.

The observed dip in the lineshape serves as a strong confirmation that the cross-polarisation between the ^{13}C and ^{1}H nuclei is local to each $H_2O@C_{60}$ molecule. Therefore, the contact time of τ_{CP}= 1 ms is used to study the effect of the ^{13}C nuclei in the C_{60} cage on the nuclear spin-isomer conversion of the entrapped ortho-H_2O in the same C_{60} cage. The time dependent cross-polarised ^{13}C NMR spectra are illustrated in Figure 10.1.6(a). It can be seen that the intensity of the ^{13}C NMR signal decays evenly across the spectrum with time. This decay is attributed to having less ortho-H_2O cross-polarising nuclear magnetisation to the ^{13}C in its C_{60} cage as more ortho-H_2O converts to para-H_2O over time. The integrated spectral intensities of the cross-polarised ^{13}C NMR spectra (blue dots) and the directly observed^{1}H NMR spectra (black squares) are plotted against time in Figure 10.1.6(b). There are no observable difference in the rate of decay between the two integrated intensities versus time plot. Hence, it can be concluded that the ^{13}C nuclei in the C_{60} cage does not have an observable influence on the nuclear spin-isomer conversion of the H_2O encapsulated in same C_{60} cage.

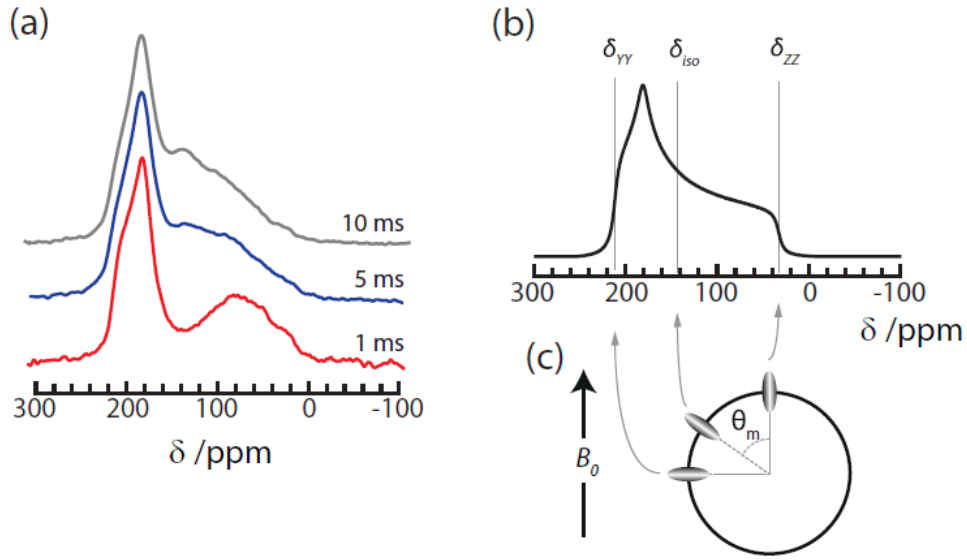

Figure 10.1.5: (a) ^{13}C NMR spectra magnetised through Hartmann-Hahn cross-polarisation between ^{1}H and ^{13}C nuclei using contact times τ_{CP}= 10 ms (grey), 5 ms (blue) and 1 ms (red) respectively without proton decoupling during signal acquisition. All of the three spectra are recorded at 5 K with 14.1 T background magnetic field. (b) Simulated static CSA pattern of C_{60} based on the principal values: δ_{XX}= 182 mppm, δ_{YY}= 213 ppm, δ_{ZZ}= 33 ppm [104]. (c) Schematic representations of the ^{13}C CSA tensors at three different positions in the fullerene cage with their respective signal contributions at the indicated spectral frequencies in the simulated lineshape in (b). The magnetic field is assumed to be in the vertical direction, with the most shielded principal axis Z oriented along the cage radius and the less shielded axis Y oriented perpendicular to the plane of the figure.

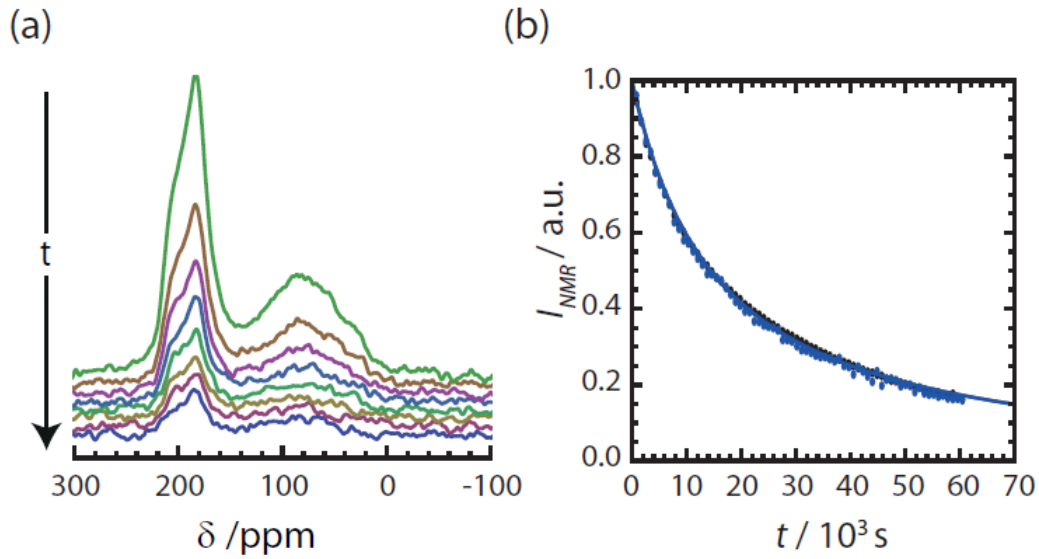

Figure 10.1.6: (a) ^{13}C spectra of $H_2O@C_{60}$ recorded with contact time of τ_{CP}= 1 ms at 5 K and background magnetic field of 14.1 T. The ^{13}C NMR signals are recorded using time intervals of 2.25 hours after cooling the sample rapidly from 60 K and waiting 30 minutes to equilibrate the sample temperature. (b) Integrated intensities of the CP ^{13}C NMR spectra (blue dots) and the directly observed^{1}H NMR spectra (black squares) plotted against time. The CP ^{13}C signal is obtained with τ_{CP}= 1 ms.

10.2 Milli-Kelvin nuclear spin-isomer conversion

10.2.1 INS

The INS experiments discussed in Chapter 8 are only recorded over a period of 8 hours due to heavier emphasis of studying the INS transitions. Therefore, the conversion plots have not been recorded long enough relative to the half-life of the nuclear spin-isomer conversion (∼8 hour) to make them suitable for studying the nuclear spin-isomer conversion rate. A separate INS experiment has been performed on the 90% filled $H_2O@C_{60}$ sample at the ILL, Grenoble to study the temperature dependent nuclear spin-isomer conversion rate at milli-Kelvin temperatures.

The milli-Kelvin INS experiments were done using the IN4C spectrometer fitted with a cryo-free dilution fridge insert in its sample cryostat. The entire sample cooling process to milli-Kelvin temperatures is divided into two separate processes. At the beginning of each experiment, the sample is equilibrated to 45 K for 30 minutes to populate the ortho-H_2O species before cooling it down rapidly to 10 K for an hour to siphon the helium out from the cryostat. After the helium has been removed from the cryostat, the dilution fridge then begins to cool the sample down to the set milli-Kelvin temperature. The entire sample cooling process takes 4 hours. Set sample temperatures of 150 mK and 500 mK were chosen for the temperature dependent study of the nuclear spin-isomer conversion. The 150 mK and 500 mK INS spectra are recorded over the course of 42 hours and 20 hours respectively.

3 Å incident neutron wavelength is used for the milli-Kelvin INS experiments to obtain highest possible resolution spectra to record the decay of the peak intensity with experiment elapsed time, t_e. Unlike the NMR conversion experiments, the decay of the ortho-H_2O peak and growth of the para-H_2O peaks are both observable in the INS spectra. Figure 10.2.1 illustrates the time evolution of the $H_2O@C_{60}$ INS spectra recorded at 150 mK. Both 150 mK and 500 mK spectra are identical to the 3 Å INS spectra recorded at 1.5 K (Figure 8.1.1), therefore similar peak assignments are applied to these spectra. The ortho-H_2O peak is denoted with (A), while the para-H_2O peaks are denoted with (B) and (C) respectively.

The normalised intensities of the peaks in the 150 mK and 500 mK spectra are plotted as a function of t_e in Figures 10.2.2 and 10.2.3 respectively. These peak intensities are obtained from their respective Gaussian

fit. It can be seen from Figure 10.2.2 that there is no observable difference between the conversion rates of the 150 mK and 500 mK conversion experiments. The 150 mK conversion plot is fitted to Equation 10.1.3 with the following parameters: A=1, $\kappa = 61.2 \times 10^{-3}$ s^{-1} and B=0. Due to the long cooling time required to reach set milli-Kelvin temperatures, there is a large ambiguity in determining the initial fraction of ortho-H_2O $\Phi(0)$. Hence, k_2 cannot be accurately determined. Figure 10.2.3 shows equal growth rate in the peak intensities at 150 mK and 500 mK for both (B) and (C) peaks.

It can be concluded from the INS nuclear spin-isomer conversion experiments that there is no temperature dependence in the nuclear spin-isomer conversion rate at milli-Kelvin temperatures.

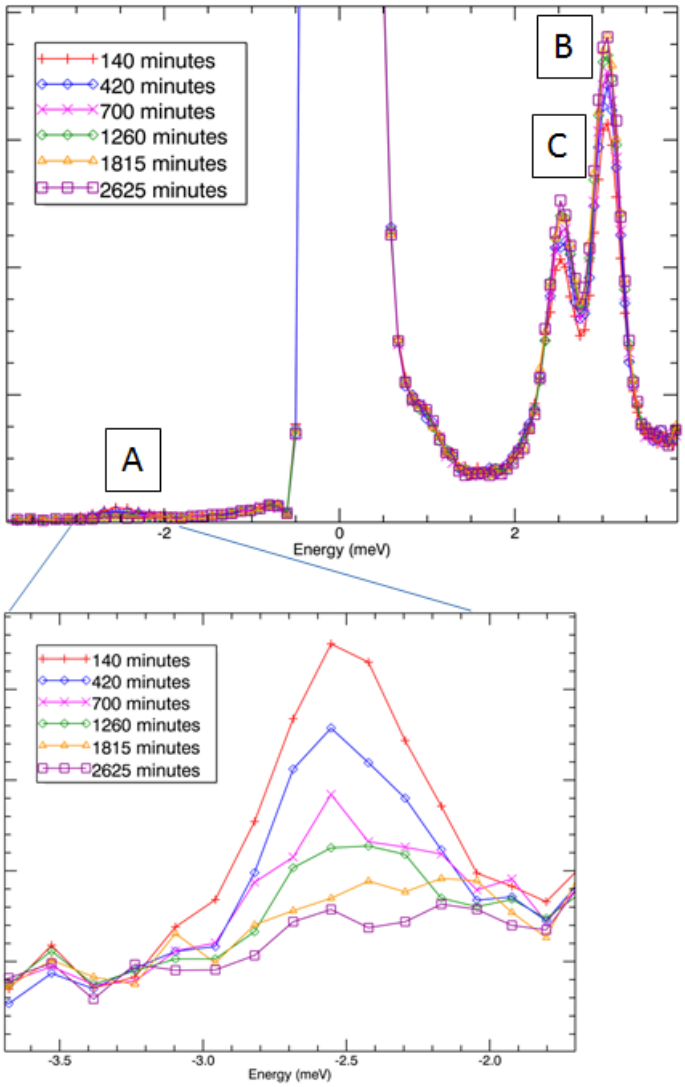

Figure 10.2.1: INS spectra of the 90% filled $H_2O@C_{60}$ sample recorded at 150 mK with 3 Å incident neutron wavelength. The different coloured spectra denotes spectra recorded different times of the experiment. The zoomed-in spectra of the peak labelled with (A) is shown below the full spectra. Peaks labelled with (B) and (C) are transitions from the ground state para-H_2O to the two respective ortho-1_{01} states.

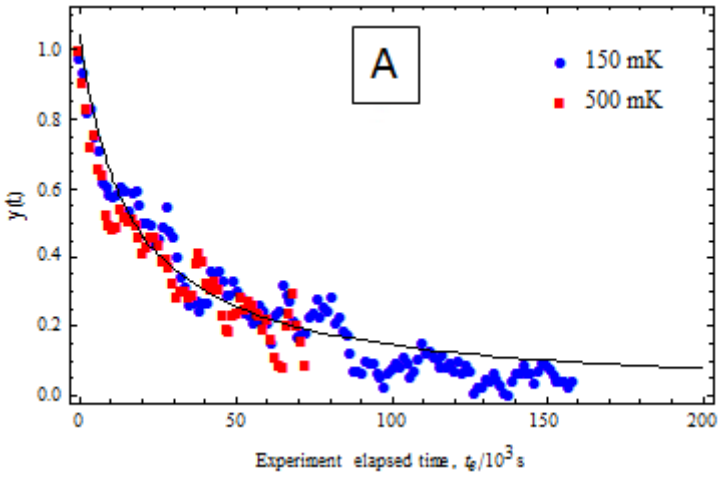

Figure 10.2.2: Intensity of the peak labelled with (A) in the 90% filled $H_2O@C_{60}$ INS spectra plotted as a function of t_e. The blue and red markers denote spectra recorded at 150 mK and 500 mK respectively. The line shows best fit to the 150 mK data using Equation 10.1.3 with the following parameters: A=1, $\kappa = 61.2 \times 10^{-3}$ s^{-1} and B=0.

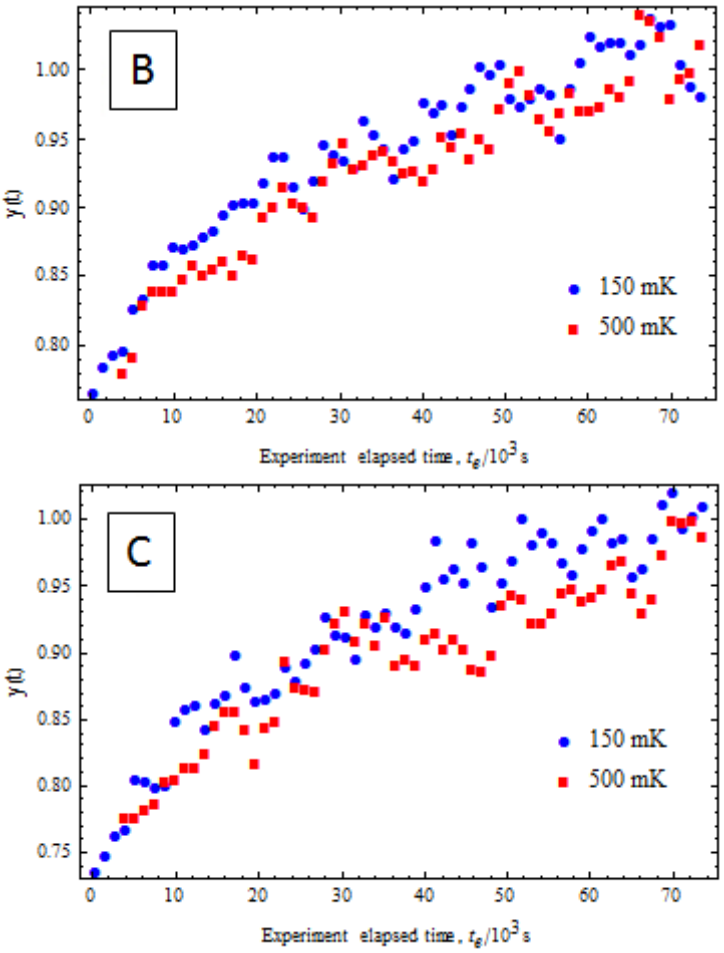

Figure 10.2.3: Intensity of the peaks labelled with (B) and (C) respectively in the 90% filled $H_2O@C_{60}$ INS spectra plotted as a function of t_e. The blue and red markers denote spectra recorded at 150 mK and 500 mK respectively.

10.2.2 NMR

This section discusses the analysis of the nuclear spin-isomer conversion of the milli-Kelvin ^{1}H NMR experiments on the 90%, 50% and 20% filled samples discussed in Section 9. The aim of this analysis is to study the temperature and fill factor dependence of the nuclear spin-isomer conversion at milli-Kelvin temperatures. The ^{1}H NMR measurements of the nuclear spin-isomer conversion of the 90% filled sample at milli-Kelvin temperatures is complementary to milli-Kelvin INS measurements of the nuclear spin-isomer conversion discussed in the Section 10.2.1. Both small angle and 90° acquisition data, which are run in conjunction with each other, can be used to plot the decay in the integrated intensity as a function of experiment elapsed time, t_e, to illustrate the nuclear spin-isomer conversion. However, only the 90% and 50% filled $H_2O@C_{60}$ samples have large enough yield to provide good SNR for the small angle measurements.

The integrated intensity of the milli-Kelvin ^{1}H NMR spectra are recorded for a much longer period of time ($\approx$ 3 days) than the higher temperature conversion experiments discussed in Section 10.1. Therefore, unlike the high temperature conversion experiments, the milli-Kelvin conversion experiments are able to reveal the trend of the decay at longer times. However, due to the long cooling times of the milli-Kelvin experiments, the first point of our conversion data is recorded at a much later time ($\approx$ 200 minutes) relative to the higher temperature conversion experiments (between 12 and 30 minutes). This results in the absence of the early and fast converting part of the conversion from the data.

The normalised integrated intensity of both small angle and 90° acquisition spectra as a function of t_e plots of the 90% filled sample recorded at 1 K are illustrated in Figure 10.2.4. The conversion plot obtained with small angle acquisition pulses is consistent with the conversion plot obtained with 90° acquisition pulses. Similar to the higher temperature conversion data, the milli-Kelvin conversion data fits well with the second-order kinetic equation (Equation 10.1.3). Due to the absence of the early and fast converting part of the conversion from the data, it is hard to estimate the initial ortho-H_2O fraction,$\Phi(0)$, for the experiment. Therefore, we are unable to obtain a conclusive conversion rate (k_2) from the milli-Kelvin conversion data. However, comparisons between the milli-Kelvin conversion data can still be made by plotting them on top of one another.

The conversion plots of the 90% filled sample recorded with 90° acquisition pulses at 1 K, 700 mK and 400 mK are illustrated in Figure 10.2.5.

The first points of the 700 mK and 400 mK conversion data are scaled to be in line with 1 K conversion data to compare the conversion rates of all three temperatures. Similar to the results from the milli-Kelvin INS experiments, there is no observable difference in the conversion rate at temperatures T$\leq$ 1.5 K.

The conversion plots of the 90%, 50% and 20% filled samples recorded at 1 K are shown in Figure 10.2.6. The first points of the 50% and 20% filled samples conversion data are scaled to the first point of the 90% filled sample data to have the conversion rates of all three samples compared. No difference in the conversion rate can be observed from the conversion plots of all three samples.

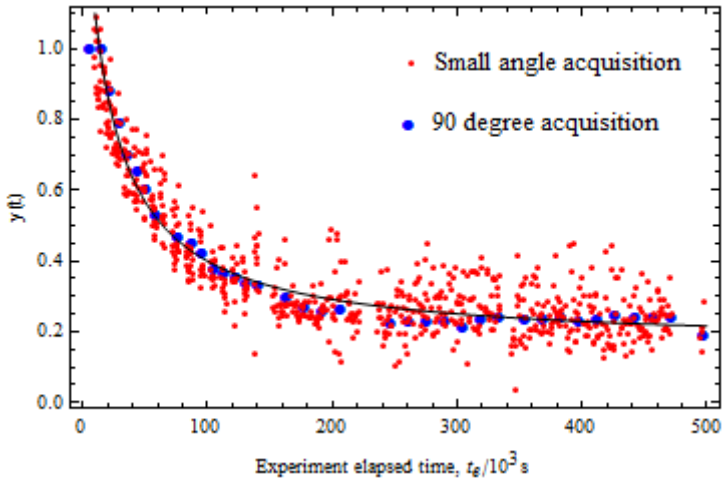

Figure 10.2.4: Integrated intensity of the small angle and 90° ^{1}H acquisition spectra as a function of t_e plots of the 90% filled sample recorded at 1 K. The solid line is the best fit to the conversion data using the second-order kinetic equation (Equation 10.1.3).

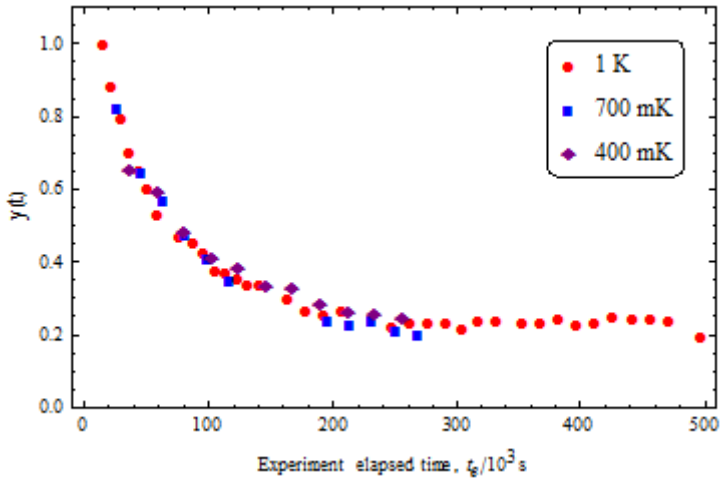

Figure 10.2.5: Integrated intensity of the 90° ^{1}H acquisition spectra as a function of t_e plots of the 90% filled sample recorded at 1 K, 700 mK and 400 mK respectively. The first point of the 700 mK and 400 mK conversion data is scaled to be in line with 1 K conversion data. There is no observable difference in the conversion rate of all three temperatures.

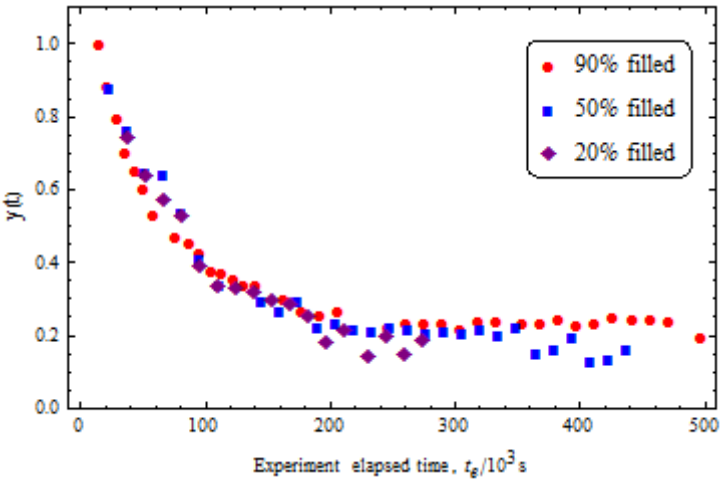

Figure 10.2.6: The respective integrated intensity of the 90° ^{1}H acquisition spectra as a function of t_e plots of the 90%, 50% and 20% filled samples recorded at 1 K. There is no observable difference in the conversion rate of all three samples.

10.3 Nuclear spin-isomer conversion mechanism

The aforementioned experimental evidence have indicated that the low temperature nuclear spin-isomer conversion process follows the second rate law. It is suggested that the second-order kinetics arise from bimolecular processes [88]. In our case, it involves two ortho-H_2O interacting with each other at close range to convert into two para-H_2O. The bimolecular mechanism can be written as:

$$o + o \rightarrow p + p* \tag{10.3.1}$$

where the left hand side indicates an interaction between a pair of neighbouring ortho-H_2O, while the right hand side indicates a pair of para-H_2O as a by product of this interaction. $p*$ indicates para-H_2O with excess energy as a result of converting from the higher energy ortho-H_2O. This para-H_2O is expected to have its excess energy dissipated to the lattice immediately after the conversion process.

Most bimolecular processes that gives rise to second-order kinetic behaviour are in solution state, where reagents freely diffuse in space. However, the reagents of $H_2O@C_{60}$ (ortho-H_2O) are fixed in space due to their confinement to the C_{60} cages, which are in solid state. It is shown in our joint paper [88] that our experimental results also indicate the occurrence of interactions between two non-neighbouring ortho-H_2O. It is shown that a significant fraction of ortho-H_2O will fail to convert to para-H_2O due to not having a nearby ortho-H_2O at later times if there is no interaction two non-neighbouring ortho-H_2O. Therefore, to explain the experimental observation where the ortho-H_2O continues to convert even with a small fraction of remaining ortho-H_2O in the sample, two postulate can be made: (1) there is a second process which "diffuses" the ortho-H_2O in $H_2O@C_{60}$; and (2) the bimolecular conversion process may take place at a distance longer than the distance between two neighbouring ortho-H_2O.

As there can be no physical diffusion of H_2O in $H_2O@C_{60}$, postulate (1) implies that the ortho-H_2O diffuses via a form of spin diffusion, where an ortho-H_2O have a finite probability of "swapping" spin state with a neighbouring para-H_2O, ie:

$$o + p \rightarrow p + o.$$

This allows for non-neighbouring ortho-H_2O to get close to another ortho-

H_2O to perform the bimolecular conversion process.

The combination of bimolecular and spin diffusion-like process seems likely to be a plausible explanation to the observed second-order kinetics of nuclear spin-isomer conversion. If the nuclear spin-isomer conversion were bimolecular processes, one would expect samples with lower cage filling factor to have slower conversion rate as it is less likely for each ortho-H_2O to have a neighbouring ortho-H_2O. Furthermore, occurrence of spin diffusion would have been greatly reduced as there would be empty C_{60} in the lattice where H_2O would not be able to "spin-diffuse" across. Hence, one would expect a higher baseline in the conversion plot for samples with lower cage filling factor due to larger portion of the ortho-H_2O being unable to convert to para-H_2O. However, the results of the milli-Kelvin conversion experiments have shown that both conversion rate (k_2) and height of the baseline (B) are independent of the cage filling factor of the sample. Therefore, it is unlikely that postulate (1) is the reason behind the second-order rate kinetic behaviour.

If the range of the bimolecular conversion process were to be much longer than the distance between two neighbouring ortho-H_2O as in the case of postulate (2), then one would expect both the conversion rate and the height of the baseline to be independent of the cage filling factor of the sample. The likely source of this long range interaction is the indirect coupling between the electric dipole moments of surrounding ortho-H_2O and the proton spins, where the electric dipole moments are coupled to the rotational angular momentum of the H_2O, which are in turn coupled to the nuclear spins via spin-rotation mechanism [105, 106]. It is already known that H_2O in high rotational states achieve uni-molecular nuclear spin-isomer conversion via this route [105, 106].

Furthermore, our experimental results has ruled out the possibility of the^{13}C in the cage having a role in the nuclear spin-isomer conversion.

10.4 Milli-Kelvin longitudinal relaxation (T_1)

The milli-Kelvin T_1 experiments have been done in conjunction with the milli-Kelvin lineshape and nuclear spin-isomer conversion experiments. Small angle acquisition pulses were introduced in the pulse sequence in Figure 9.1.1 to overcome the long T_1 relaxation rate by ensuring that the probing of the relative signal intensities does minimal disruption to the magnetisation, thus not requiring to saturate the signal after measuring each point of the T_1 recovery curve. The signal obtained from the small angle acquisition pulse still has a good SNR due to the increase in the polarisation from having a low sample temperature. All of the T_1 data discussed in this section are based on spectra which have been subtracted by the last spectrum of the experiment to ensure that only signal from the ortho-H_2O is analysed.

Of the three samples of different filling factor, only the T_1 of the 90% and 50% filled sample have been successfully measured. This is due to the 20% filled samples not generating enough proton signal from the small angle acquisition pulses to provide large enough SNR. Besides having less material than the 90% and 50% filled sample, the 20% sample also have a lower filling factor, thus resulting in lower number of protons in the samples.

The magnetisation recovery curve is the compilation of the integrated intensity of the spectra recorded at different recovery time, t. The longitudinal relaxation rate (T_1) can be obtained by fitting the magnetisation recovery curve with the inverse exponential equation. The inverse exponential equation is written as:

$$M(t) = M_0(1 - \exp(-\frac{t}{T_1})) + C \tag{10.4.1}$$

where $M(t)$ is the instantaneous magnetisation; t is the time variable; M_0 is the fully recovered magnetisation value; C is the magnetisation at $t = 0$. The direct fitting of the magnetisation recovery data with Equation 10.4.1 does not yield an accurate value of T_1 due to the exponential nature of this equation. Equation 10.4.1 can be rearranged into the following logarithmic expression:

$$\frac{t}{T_1} = -\log[\frac{M_0 - M(t)}{M_0}] \tag{10.4.2}$$

to allow for a linear fit to T_1^{-1}. The data, $M(t)$, is transformed into the above logarithmic form to allow for the linear fitting of the data using Equation 10.4.1 to obtain the T_1 value. This logarithmic fit provides a smaller

standard deviation to the T_1 fit value than Equation 10.4.1. However, this fitting method requires an accurate measure of M_0.

The magnetisation recovery curve illustrated in Figure10.4.1(a) is obtained from the integrated intensity of the small angle acquisition pulse spectra which have been subtracted by the last spectrum of the experiment ("end spectrum") [1] and recorded at 1 K and $t_e = 262$ minutes. The slope observed at the end section of the T_1 recovery curve the resulted of the ortho-H_2O converting to para-H_2O. The logarithmic data[2] of Figure 10.4.1(a) and its fit (using Equation 10.4.2) is shown in Figure 10.4.1(b). The M_0 value used in the logarithmic transformation of each T_1 data is obtained from the insertion of their respective t_e value into the fit equation of the conversion plot in Figure 10.2.4. This method of obtaining the M_0 value is used to reduce the scatter in the fitted T_1 value. Only the logarithmic transformed data points with $t < 400$ s are used for the fit, as the data points with $t \geq 400$ s have large standard deviation. A linear fit is applied to the logarithmic transformed data to obtain the fitted T_1 value.

The effect of the ^{1}H NMR signal from non-converting protonated impurities on the fitted T_1 values can be seen from the two T_1 as a function of t_e plots shown in Figure 10.4.2. By comparing the T_1 of the spectra which have (blue) and have not (red) had the last spectrum of the experiment subtracted from them, it can be seen that the red plot have higher fitted T_1 values than the blue plot, thus suggesting that there is a long T_1 component in the non-subtracted spectra. The result of the blue plot suggests that as more ortho-H_2O converts to para-H_2O, the T_1 of the remaining ortho-H_2O increases. The T_1 of the ortho-H_2O then plateaus to ≈ 60 s^{-1} as the conversion slows down dramatically. The large scattering observed in the T_1 values obtained at the end of the experiment is the result of the diminishing ortho-H_2O ^{1}H NMR signal towards the end of the experiment.

A similar procedure is done to treat the magnetisation recovery data of the 90% filled sample recorded at 700 mK and 400 mK, and the 50% filled sample recorded at 1 K to convert them to the logarithmic form before fitting the data to obtain the respective T_1 values. The T_1 as a function of t_e plots for the 90% filled sample recorded at all three temperatures are illustrated in Figure 10.4.3. The T_1 at the beginning of the conversion experiment are observed to be the same (≈ 20 s) for all three temperature data. As more ortho-H_2O converts to para-H_2O, the T_1 of all three tem-

[1] The subtraction method is similar to the those performed on the 90° acquisition pulse spectra shown in Figures 9.2.5, 9.2.6 and 9.2.7.

[2] Logarithmic form of the magnetisation recovery data.

perature data begins to diverge, with the $T_1$of the lower temperature data increases at a faster rate than the higher temperature data. The T_1 of all three temperature data eventually plateaus as the conversion slows down dramatically, with the higher temperature data plateauing at a higher T_1 value than the lower temperature data. The comparison between the T_1 as a function of t_e plots of the 90% and 50% filled samples at 1 K are illustrated in Figure 10.4.4. Besides the poorer statistics at the later points of the T_1 data of the 50% filled sample, there are no observable difference in the two T_1 as a function of t_e plots.

The experiments on the $H_2O@C_{60}$ samples have shown remarkably fast T_1 even at 400 mK (as low as 50 s), where most samples would have a T_1 of the order of tens of minute to a few hours. This relatively fast T_1 is attributed to the quantum rotation of the ground state ortho-H_2O contributing to the T_1 relaxation mechanism at milli-Kelvin temperatures. The observed increase in the T_1 with time is related to the ortho-H_2O to para-H_2O conversion, where the reduced presence of neighbouring quantum rotors (ortho-H_2O) at later times of the experiment results in the reduced contribution from the inter-cage interactions to the overall T_1 relaxation process. The null dependence of the T_1 relaxation rate on the cage filling factor suggests that the inter-cage T_1 relaxation process occurs at a much longer distance than the distance between two neighbouring C_{60} cages.

It is also possible that the indirect coupling between the rotating electric dipole moments of the surrounding ortho-H_2O and the nuclear spins are responsible for this long range T_1 relaxation process, similar to the nuclear spin-isomer conversion mechanism explained in the previous section. Since T_1 relaxations are dependent on molecular motions (i.e. rotations) to spontaneously change the local field experienced by the spins, this suggests that the electric dipole moments of the surrounding molecules would require to have some form of molecular motion to cause T_1 relaxation. It is demonstrated in Figure 7.1.1 that the electric dipole moment of the ground state ortho-H_2O rotates together with the molecular rotation along the same rotation plane. Therefore, it is plausible that the electric field of the surrounding ortho-H_2O is responsible for the long range T_1 relaxation process required to explain the null dependence of T_1 on the cage filling factor. Therefore, it is plausible that both nuclear spin-isomer conversion and T_1 relaxation share the same mechanism, albeit the nuclear spin-isomer conversion of H_2O only occurring from extra-molecular interactions (as it require symmetry breaking within the H_2O molecules), whereas T_1 relaxation can occur from both extra- and intra-molecular interactions (as it does

not require symmetry breaking within the H_2O molecules).

(a)

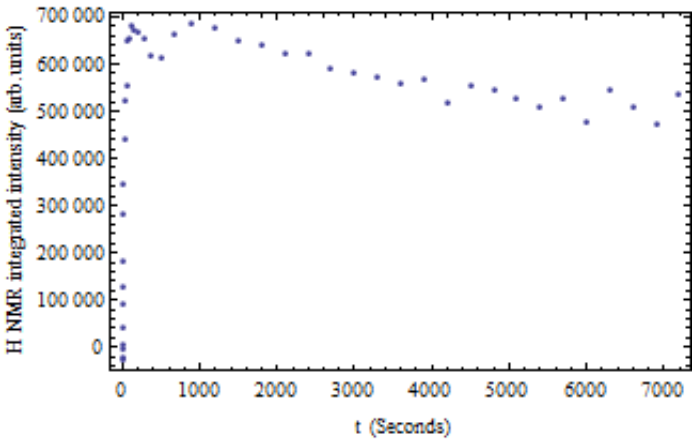

(b)

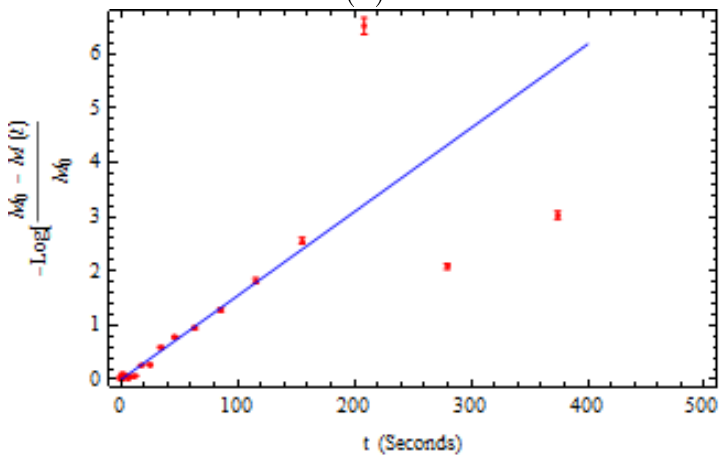

Figure 10.4.1: 90% filled sample: (a) Magnetisation recovery curves of the $H_2O@C_{60}$ ^{1}H NMR spectra at T =1 K and t_e = 262 minutes. Each point in the curve is the integrated intensity of the spectra which are recorded with small angle acquisition pulse and have not been subtracted by the last spectrum of the experiment. (b) The logarithmic form of the magnetisation recovery curve shown in (a). Equation 10.4.2 is used for the linear fitting of the logarithmically transformed T_1 data to obtain the T_1 value.

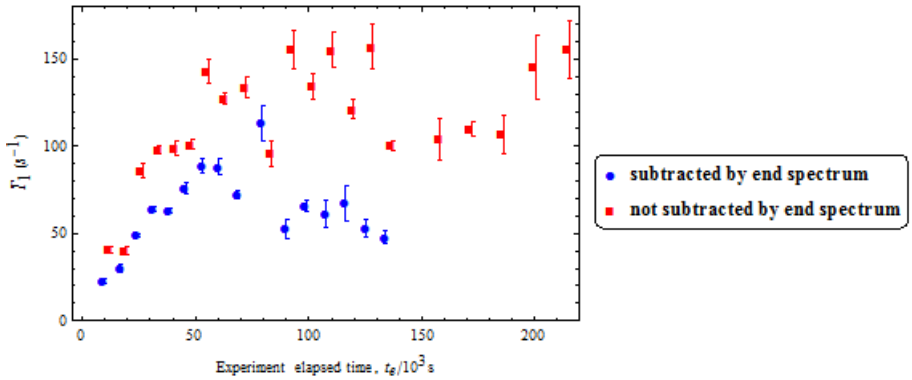

Figure 10.4.2: 90% filled sample: (Red) T_1 of the $H_2O@C_{60}$ ^1H NMR spectra which have and have not been subtracted by the last spectrum of the experiment plotted against the experimental elapsed time t_e. (Blue) T_1 of the $H_2O@C_{60}$ ^1H NMR spectra which have been subtracted by the last spectrum of the experiment plotted against the experimental elapsed time t_e. The higher T_1 values seen in the non-subtracted spectra suggests that there is a long T_1 component in the spectra.

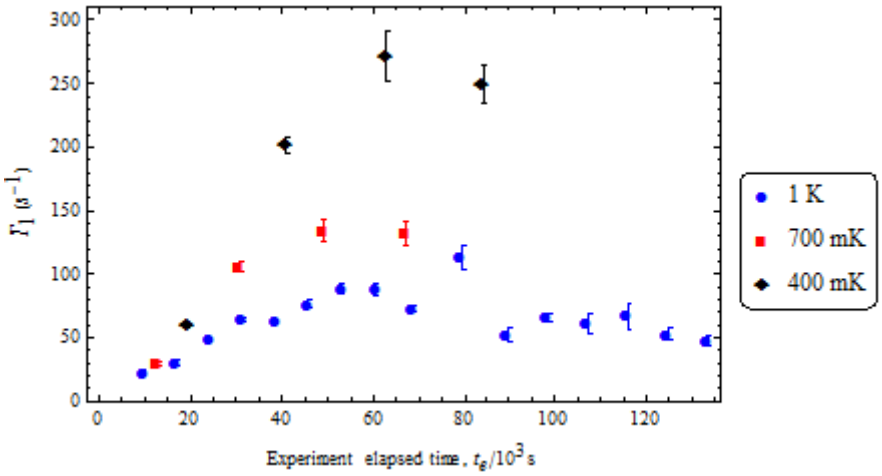

Figure 10.4.3: 90% filled sample: T_1 of the $H_2O@C_{60}$ ^1H NMR spectra which have been subtracted by the last spectrum of the experiment plotted against the experimental elapsed time t_e. The sample temperatures of the recorded T_1 are: 1 K (blue), 700 mK (red) and 400 mK (black). It can be seen from the plots that the T_1 plateaus at a higher value at lower temperatures.

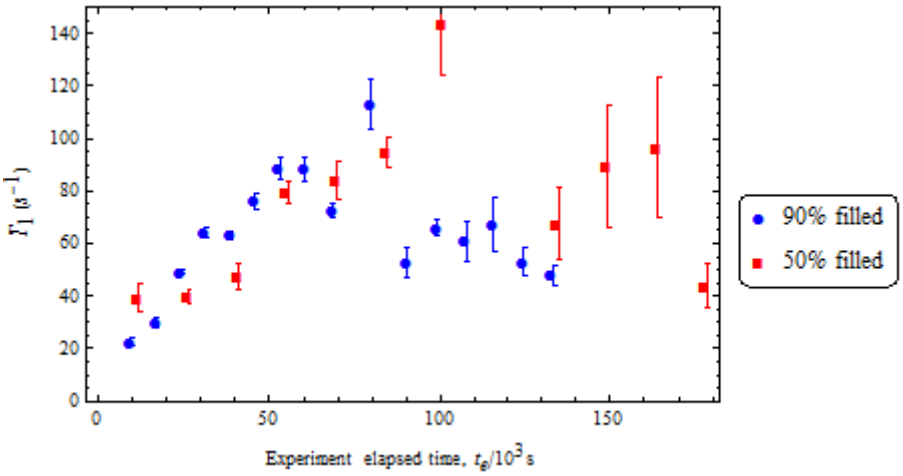

Figure 10.4.4: 1 K sample temperature: T_1 of the ^{1}H NMR spectra of the 90% and 50% filled $H_2O@C_{60}$ sample plotted against the experimental elapsed time t_e. The spectra of both samples have been subtracted by the last spectrum of the experiment. No observable difference is seen between the two T_1 as a function of t_e plots for the 90% and 50% filled samples.

10.5 Conclusions

The nuclear spin-isomer conversion experiments of $H_2O@C_{60}$ at cryogenic temperatures have revealed a conversion process that follows the second-order rate law. This suggests that the nuclear spin-isomer conversion in $H_2O@C_{60}$ is a bimolecular process that involves a pair of neighbouring ortho-H_2O interacting to convert into a pair of para-H_2O.

The higher temperature conversion experiments (4.2 K$\leq$T$\leq$15 K) has shown that the conversion rate (k_2) is fast and changes rapidly with temperature at 10 K$\leq$T$\leq$15 K, and slows down and becomes weakly dependent on temperature at 4.2 K$\leq$T$\leq$10 K. It is also shown from the milli-Kelvin NMR and INS experiments that the conversion rate becomes independent of temperature at T$\leq$1.5 K. Furthermore, the ^{1}H NMR conversion experiments of the 90%, 50% and 20% filled $H_2O@C_{60}$ samples at milli-Kelvin temperatures have shown that the conversion rate is not dependent on the cage filling factor at T$\leq$1 K. ^{13}C CP NMR experiments have also been done at 5 K to show that the nuclear spin-isomer conversion is not dependent on the ^{13}C in the cage.

The milli-Kelvin T_1 experiments on the $H_2O@C_{60}$ samples have shown relatively fast T_1 relaxation rates at milli-Kelvin temperatures due to the quantum rotation of ortho-H_2O. The observed increase in the T_1 with respect to time is likely to be due to the ortho-H_2O to para-H_2O conversion which results in the reduced presence of surrounding ortho-H_2O contributing to the inter-molecular T_1 relaxation. Furthermore, the null dependence of the T_1 on the cage filling factor indicates that the inter-molecular T_1 relaxation process takes place at a range beyond the neighbouring C_{60} cages. Based on the properties of the ground state ortho-H_2O deduced in Chapter 7, it is likely that the rotating electric dipole moment is responsible for this long range interaction. Therefore, it is postulated that in addition to the intra-molecular T_1 relaxation process, the nuclear spins of the ortho-H_2O is also relaxed through indirect coupling with the rotating electric dipole moment of the surrounding ortho-H_2O.

Based on the results gathered from the nuclear spin-isomer conversion and milli-Kelvin T_1 analysis, it is deduced that the long range indirect coupling between the rotating electric dipole moment of the surrounding ortho-H_2O and the nuclear spin is responsible for the nuclear spin-isomer conversion. This deduction is required to explain the fact that H_2O requires extra-molecular interactions to cause symmetry breaking within the molecule to achieve nuclear spin-isomer conversion, while long range inter-

actions are required to explain the null dependence on the cage filling factor observed in both T_1 and nuclear spin-isomer conversion experiments.

Part V

Conclusions and final remarks

Chapter 11

Conclusions and final remarks

The aim of this Ph.D. thesis is to investigate the quantum dynamics of the encapsulated small molecules inside the fullerene cages (small molecule endohedral fullerenes), namely the $H_2@C_{60}$, $H_2@C_{70}$ and $H_2O@C_{60}$molecules, using inelastic neutron scattering (INS) and nuclear magnetic resonance (NMR). The thesis begins by introducing the basic concepts of small molecule endohedral fullerenes and the theories of INS and NMR spectroscopy. This is then followed by the discussion of the experimental results of the three aforementioned samples, which can be summarised with the following points:

1. The INS investigation of the simplest variant of small molecule endohedral fullerene, the $H_2@C_{60}$. The temperature dependence study using cold neutron scattering have shown that transitions from different translational states can be identified by analysing the temperature in which the transition appears in the spectra. The dynamics of this molecule is the most well understood among the variants of small molecule endohedral fullerene and is served as the foundation for the other two variants, the $H_2@C_{70}$ and $H_2O@C_{60}$.

2. The effect of molecules being entrapped in a less symmetric C_{70} cage (as compared to C_{60}) is investigated by studying the dynamics of $H_2@C_{70}$ using INS. Lifting of the degeneracies of both rotational and translational states has been observed as a result of having an elongated axis relative to C_{60}. The results from the analysis of this symmetry breaking effect is used to understand a similar symmetry breaking effect observed in the INS spectra of $H_2O@C_{60}$.

3. The INS investigation of the $H_2O@C_{60}$ has revealed a symmetry breaking effect which is deduced to originate from the electrical dis-

tortion of the C_{60} cage. The NMR lineshape investigation at milli-Kelvin temperatures has led to several preliminary deductions on the inter-fullerene interactions as well as the properties of the crystal field generated by the electric dipole moments of H_2O. The NMR investigation of the low temperature nuclear spin-isomer conversion and T_1 relaxation have also led to several preliminary deductions on the properties of the ground state ortho-H_2O to explain the required symmetry breaking effect. The compilation of the preliminary deductions made on the $H_2O@C_{60}$ and the respective observations in which they are based on are shown in Table 11.1.

Even though the deductions made on the interactions and molecular dynamics of $H_2O@C_{60}$ are consistent with the experimental results, further discussion, experimentation and computational simulations are needed to verify these deductions. Experiments such as the INS investigation of the lower filled $H_2O@C_{60}$ samples could provide further insights on the effect of inter-fullerene interactions on the quantum dynamics of the encapsulated H_2O, while the ^1H NMR lineshape simulations of $H_2O@C_{60}$ could provide more accurate interpretation of the recorded milli-Kelvin ^1H NMR lineshape.

Deductions:	Observations in which the deductions are based on:
Ortho-H_2O does not possess an effective electric dipole moment, while para-H_2O does. Only para-H_2O contributes to the crystal field.	Symmetry breaking of the 1_{01} state (INS); Temperature dependence analysis of the IN5 spectra (INS); Increase in T_1 with respect to conversion (NMR).
The crystal field indirectly couples with the electric quadrupole moment of an ortho-H_2O by inducing an electric dipole moment on its cage, which in turn generates an internal electric field that couples with the electric quadrupole moment of the entrapped ortho-H_2O to break the symmetry of the ortho-H_2O ground state.	Symmetry breaking of the 1_{01} state (INS); Temperature dependence analysis of the IN5 spectra (INS); Comparing the degeneracy distribution of the two lowest ortho-H_2@C_{70} states with those of the two lowest ortho-H_2O@C_{60} states (INS).
The ground state ortho-H_2O is not degenerate and rotates in the plane parallel to the induced electric dipole moment of the cage.	Temperature dependence analysis of the IN5 spectra (INS).
The crystal field of the H_2O@C_{60} lattice is uniaxial.	Comparison between experimental H_2O@C_{60} lineshapes and the simulated H_2@C_{60} lineshapes (NMR).
The crystal field strength increases with lower milli-Kelvin temperatures.	Comparison between the experimental H_2O@C_{60} lineshapes and the simulated H_2@C_{60} lineshapes (NMR); Increase in the doublet separation frequency with respect to lower milli-Kelvin temperatures (NMR).
The induced electric dipole moment of the C_{60} cage of each ortho-H_2O in the 90% filled sample is saturated since the beginning of the conversion experiment.	No change in the doublet separation frequency of the 90% filled sample with respect to nuclear spin-isomer conversion (NMR).
The electric dipole interactions are long range interactions that occurs at a distance longer than the distance between two neighbouring C_{60}.	Increase in the separation frequency of the doublet in the 50% and 20% filled sample spectra with respect to conversion (NMR); Second order kinetic behaviour of the conversion process (INS and NMR); No observable difference in the conversion rate between the 90%, 50% and 20% filled samples (NMR); No observable difference in T_1 between the 90%, 50% and 20% filled samples (NMR).
The long range indirect coupling between the nuclear spins and the rotating electric dipole moments of the surrounding ortho-H_2O is responsible for the non-local symmetry breaking effect required to cause nuclear spin-isomer conversion at low temperatures.	Second order kinetic behaviour of the conversion process (INS and NMR); Slow conversion rate at the end of conversion experiment indicates that para-H_2O does not contribute to conversion process (INS and NMR); No observable difference in the conversion rate between the 90%, 50% and 20% filled samples (NMR).
The rotating electric dipole moments of surrounding ortho-H_2O is responsible for the long range inter-fullerene T_1 process, while the spin-rotation coupling is responsible for intra-fullerene T_1 process.	No observable difference in T_1 between the 90% and 50% filled samples, indicating long range T_1 process (NMR); Relatively fast T_1 relaxation rate at milli-Kelvin temperatures (NMR).

Table 11.1: Compilation of the preliminary deductions made on the interactions and molecular dynamics of H_2O@C_{60} along with the respective observations in which the deductions were based on.

Bibliography

[1] Y. Murata, M. Murata, K. Komatsu, Journal of the American Chemical Society 125, 7152 (2003).

[2] K. Komatsu, M. Murata, Y. Murata, Science 307 238–240 (2005).

[3] M. Murata, Y. Murata, and K. Komatsu, J. Am. Chem. Soc. 128, 8024 (2006).

[4] M. Murata, S. Maeda, Y. Morinaka, Y. Murata, K. Komatsu, J. Am. Chem. Soc., 130, 15800 (2008).

[5] K. Kurotobi, Y. Murata, Science, 333, 613–616 (2011).

[6] A. Krachmalnicoff, M. H. Levitt, R. J. Whitby, Chem. Commun., 50, 13037 (2014).

[7] R. J. Cross, The Journal of Physical Chemistry A 105, 6943 (2001).

[8] H. W. Kroto, J. R. Heath, S. C. O'Brien, R. F. Curl, R. E. Smalley, Nature 318, 162 (1985).

[9] S. Mamone, Theory and spectroscopy of dihydrogen endofullerenes. Ph.D. thesis. University of Southampton (2012).

[10] W. I. F. David et al Europhys. Lett. 18 219 (1992).

[11] P. Heiney, J. Fischer, A. McGhie, W. Romanow, A. Denenstein, J. McCauley Jr., A. Smith, and D. Cox, Physical Review Letters 66, 2911 (1991).

[12] R. Tycko, G. Dabbagh, R. M. Fleming, R. C. Haddon, A. V. Makhija, and S. M. Zahurak, Physical Review Letters 67, 1886 (1991).

[13] P. Heiney, J. Fischer, A. McGhie, W. Romanow, A. Denenstein, J. McCauley, A. Smith, and D. Cox, Physical Review Letters 67, 1468 (1991).

[14] W. Schranz, A. Fuith, P. Dolinar, H. Warhanek, M. Haluska, and H. Kuzmany, Physical Review Letters 71, 1561 (1993).

[15] C70 fullerene, accessed 20 October 2014, <http://en.wikipedia.org/wiki/C70_fullerene>.

[16] G. B. M. Vaugham et al, Science 254, 1350 (1991).

[17] R. M. Fleming et al, Phys. Rev. B 44, 888 (1991).

[18] M. A. Verheijen et al, Chem. Phys. 166, 287 (1992).

[19] G. van Tendeloo et al, Europhys. Lett. 21 329 (1993).

[20] D. H. Oh et al, Phys. Rev. Lett.,75, 4230, (1995).

[21] M. Sprik, A. Cheng and M. L. Klein, Phys. Rev. Lett. 69, 1660 (1992).

[22] J. R. Heath, S. C. O'Brien, Q. Zhang, Y. Liu, R. F. Curl, F. K. Tittel, R. E. Smalley, Journal of the American Chemical Society 107, 7779 (1985).

[23] Y. Chai, T. Guo, C. Jin, R. E. Haufler, L. P. F. Chibante, J. Fure, L. Wang, J. M. Alford, R. E. Smalley, The Journal of Physical Chemistry 95, 7564 (1991).

[24] R. D. Johnson, M. S. de Vries, J. Salem, D. S. Bethune, C. S. Yannoni, Nature 355, 239 (1992).

[25] C. Knapp, K.-P. Dinse, B. Pietzak, M. Waiblinger, and A. Weidinger, Chem. Phys. Lett. 272, 433 1997.

[26] M. Kanai, K. Porfyrakis, G. A. D. Briggs and T. J. S. Dennis, Chem. Commun. 2, 210 (2004).

[27] J. J. L. Morton, A. M. Tyryshkin, A. Ardavan, K. Porfyrakis, S. A. Lyon, and G. A. D. Briggs, J. Chem. Phys. 122, 174504 2005.

[28] J. J. L. Morton, A. M. Tyryshkin, A. Ardavan, K. Porfyrakis, S. A. Lyon, G. A. D. Briggs, J. Chem. Phys. 124, 014508 (2006).

[29] J. J. L. Morton, A. M. Tyryshkin, A. Ardavan, S. C. Benjamin, K. Porfyrakis, S. A. Lyon, G. A. D. Briggs, Phys. Stat. Sol. (b) 243, 3028 (2006).

[30] G. Liu , A. N. Khlobystov, G. Charalambidis, A. G. Coutsolelos, G. A. D. Briggs, K. Porfyrakis, J. Am. Chem. Soc., 134, 1938 (2012).

[31] S. Stevenson, G. Rice, T. Glass, K. Harich, F. Cromer, M. R. Jordan, J. Craft, E. Hadju, R. Bible, M. M. Olmstead, K. Maitra, A. J. Fisher, A. L. Balch, H. C. Dorn, and Others, Nature 401, 55 (1999).

[32] Y. Rubin, Top Curr Chem 199:67–91 (1999).

[33] G. L. Squires, Introduction to the theory of thermal neutron scattering, Cambridge University Press (2012).

[34] A. J. Horsewill et al, Phys. Rev. B 85, 205440 (2012).

[35] T. Yildirim and A. B. Harris, Phys. Rev. B 66, 214301 (2002).

[36] J. A. Young and J. U. Koppel, Phys. Rev. 135, A603 (1964).

[37] Thermal neutron time-of-flight spectrometer IN4C, ILL, accessed 18 October 2014, <https://www.ill.eu/instruments-support/instruments-groups/instruments/in4c/description/instrument-layout/>.

[38] Disk chopper time-of-flight spectrometer IN5, accessed 19 October 2014, <http://www.ill.eu/instruments-support/instruments-groups/instruments/in5>.

[39] Hot neutron three-axis spectrometer IN1 - TAS/Lagrange, accessed 19 October 2014, <https://www.ill.eu/instruments-support/instruments-groups/instruments/in1-taslagrange/description/instrument-layout/>.

[40] M. Levitt, Spin Dynamics. Basics of Nuclear Magnetic Resonance, 2nd ed., John Wiley and Sons, Chichester (2008).

[41] Dipolar Interaction, accessed 20 October 2014, <http://mutuslab.cs.uwindsor.ca/schurko/ssnmr/ssnmr_schurko.pdf>.

[42] L Ulivi1, M Celli, A Giannasi, A J Ramirez-Cuesta and M Zopp, J. Phys: Condensed Matter 20, 104242 (2008).

[43] A. J. Horsewill, K. S. Panesar, S. Rols, M. R. Johnson, Y. Murata, K. Komatsu, S. Mamone, A. Danquigny, F. Cuda, S. Maltsev, M. C. Grossel, M. Carravetta, and M. H. Levitt, PRL 102, 013001 (2009).

[44] M. Xu, F. Sebastianelli, Z. Bacic, R. Lawler, and N. J. Turro, J. Chem. Phys. 128, 011101 (2008).

[45] M. Xu, F. Sebastianelli, Z. Bacic, R. Lawler, and N. J. Turro, J. Chem. Phys. 129, 064313 (2008).

[46] M. Xu, F. Sebastianelli, B. R. Gibbons, Z. Bacic, R. Lawler, and N. J. Turro, J. Chem. Phys. 130, 224306 (2009).

[47] M. Xu, S. Ye, A. Powers, R. Lawler,3 N. J. Turro, and Z. Bacic J. Chem. Phys. 139, 064309 (2013).

[48] S. F. Parker and P. I. Haris. Spectroscopy-an International Journal, 22, 297-307 (2008).

[49] M. Carravetta, O. G. Johannessen, M. H. Levitt, I. Heinmaa, R. Stern, A. Samoson, A. J. Horsewill, Y. Murata, K. Komatsu, J. Chem. Phys. 124, 104507 (2006).

[50] M. Carravetta et al, Phys. Chem. Chem. Phys. 9, 4879–4894 (2007).

[51] M. H. Levitt, Phil. Trans. R. Soc. A 371, 20120429 (2013).

[52] S. Mamone et al, J. Chem. Phys. 130, 081103 (2009).

[53] M. Ge et al, J. Chem. Phys. 134, 054507 (2011).

[54] M. Ge et al, J. Chem. Phys. 135, 114511 (2011).

[55] S. Mamone, J. Y-C Chen, R. Bhattacharyya, M. H. Levitt, R. G. Lawler, A. J. Horsewill, T. Room, Z. Bacic, N. J. Turro, Coord. Chem. Rev. 255, 938–948 (2011).

[56] G. Herzberg, Molecular Spectra and Molecular Structure, I. Spectra of Diatomic Molecules, 2nd ed. Van Nostrand, Princeton (1950).

[57] E. J. Allin, W. F. J. Hare, and R. E. MacDonald, Phys. Rev. 98, 554 (1955).

[58] W. F. J Hare, E. J. Allin, and H. L. Welsh, Phys. Rev. 99, 1887 (1955).

[59] A. J. Horsewill, K. Goh, S. Rols, J. Ollivier, M. R. Johnson, M. H. Levitt, M. Carravetta, S. Mamone, Y. Murata, J. Y-C Chen, J. A. Johnson, X. Lei and N. J. Turro, Phil. Trans. R. Soc. A 371, 20110627 (2013).

[60] Y. Kohama et al, Phys. Rev. Lett. 103, 073001 (2009).

[61] Personal communication with A. J. Horsewill and S. Mamone (2014).

[62] TOFTOF, Cold neutron time-of-flight spectrometer, Heinz Maier-Leibnitz Zentrum, accessed 16 September 2014, <http://www.mlz-garching.de/toftof>.

[63] P. Bunker and P. Jensen, Molecular Symmetry and Spectroscopy, 2nd ed. (NRC Research Press, Ottawa, 1998), p. 752.

[64] M. J. Mumma, H. A. Weaver, and H. P. Larson, Astron. Astropyphys. 187, 419 (1987).

[65] J. Crovisier, Science 275, 1904 (1997).

[66] D. C. Lis, T. G. Phillips, P. F. Goldsmith, D. A. Neufeld, E. Herbst, C. Comito, P. Schilke, H. S. P. Müller, E. A. Bergin, M. Gerin, T. A. Bell, M. Emprechtinger, J. H. Black, G. A. Blake, F. Boulanger, E. Caux, C. Ceccarelli, J. Cernicharo, A. Coutens, N. R. Crockett, F. Daniel, E. Dartois, M. De Luca, M.-L. Dubernet, P. Encrenaz, E. Falgarone, T. R. Geballe, B. Godard, T. F. Giesen, J. R. Goicoechea, C. Gry, H. Gupta, P. Hennebelle, P. Hily-Blant, R. Ko^{3}os, J. Kre^{3}owski, C. Joblin, D. Johnstone, M. Ka´zmierczak, S. D. Lord, S. Maret, P. G. Martin, J. Martín-Pintado, G. J. Melnick, K. M. Menten, R. Monje, B. Mookerjea, P. Morris, J. A. Murphy, V. Ossenkopf, J. C. Pearson, M. Pérault, C. Persson, R. Plume, S.-L. Qin, M. Salez, S. Schlemmer, M. Schmidt, P. Sonnentrucker, J. Stutzki, D. Teyssier, N. Trappe, F. F. S. van der Tak, C. Vastel, S. Wang, H. W. Yorke, S. Yu, J. Zmuidzinas, A. Boogert, N. Erickson, A. Karpov, J. Kooi, F. W. Maiwald, R. Schieder, and P. Zaal, Astron. Astropyphys. 521, L26 (2010).

[67] M. Emprechtinger, D. C. Lis, T. Bell, T. G. Phillips, P. Schilke, C. Comito, R. Rolffs, F. van der Tak, C. Ceccarelli, H. Aarts, A. Bacmann, A. Baudry, M. Benedettini, E. A. Bergin, G. Blake, A. Boogert, S. Bottinelli, S. Cabrit,P. Caselli, A. Castets, E. Caux, J. Cernicharo, C. Codella, A. Coutens, N. Crimier, K. Demyk, C. Dominik, P. Encrenaz, E. Falgarone, A. Fuente, M. Gerin, P. Goldsmith, F. Helmich, P. Hennebelle, T. Henning, E. Herbst, P. Hily-Blant, T. Jacq, C. Kahane, M. Kama, A. Klotz, J. Kooi, W. Langer, B. Lefloch, A. Loose, S. Lord, A. Lorenzani, S. Maret, G. Melnick, D. Neufeld, B. Nisini, V. Ossenkopf, S. Pacheco, L. Pagani, B. Parise, J. Pearson, C. Risacher, M. Salez, P. Saraceno, K. Schuster, J. Stutzki,

X. Tielens, M. van der Wiel, C. Vastel, S. Viti, V. Wakelam, A. Walters, F. Wyrowski, and H. Yorke, Astron. Astropyphys. 521, L28 (2010).

[68] T. Kravchuk, M. Reznikov, P. Tichonov, N. Avidor, Y.Meir, A. Bekkerman, and G. Alexandrowicz, Science 331, 319 (2011).

[69] V. I. Tikhonov and A. A. Volkov, Science 296, 2363 (2002).

[70] S. L. Veber, E. G. Bagryanskaya, and P. L. Chapovsky, J. Exp. Theor. Phys. 102, 76 (2006).

[71] R. L. Redington and D. E. Milligan, J. Chem. Phys. 39, 1276 (1963).

[72] M. E. Fajardo, S. Tam, and M. E. DeRose, J. Mol. Struct. 695–696, 111 (2004).

[73] J. Y.-C. Chen1, Y. Li, M. Frunzi1, X. Lei, Y. Murata, R. G. Lawler, and N. J. Turro, Phil Trans R Soc A, 371 1998 (2013).

[74] S. Mamone, M. Concistrè, I. Heinmaa, M. Carravetta, I. Kuprov, G. Wall, M. Denning, X. Lei, J. Y. Chen, Y. Li, Y. Murata, N. J. Turro, M. H. Levitt, ChemPhysChem, 16;14(13):3121-30 (2013).

[75] C. Beduz et al, Proceedings of the National Academy of Sciences of the United States of America. 109(32): p. 12894-12898 (2012).

[76] P. Helminger and F. C. Delucia, Journal of Molecular Spectroscopy, 70, 263-26 (1978).

[77] L. D. Landau and E. M. Lifshitz, Quantum Mechanics: Non-relativistic Theory, Pergamon Press, Oxford, 3rd ed (1977).

[78] J. Cioslowski and A. Nanayakkara, Phys. Rev. Lett., 69, 2871(1992).

[79] S. Aoyagi, N. Hoshino, T. Akutagawa, Y. Sado, R. Kitaura, H. Shinohara, K. Sugimoto, R. Zhange and Y. Muratae, Chem. Commun., 50, 524 (2014).

[80] B. Ensing, F. Costanzo and P. L. Silvestrelli, J. Phys. Chem. A, 116, 12184−12188 (2012).

[81] D. Bucher, Chem. Phys. Lett., 534, 38 (2012).

[82] C. Ramachandran, N. Sathyamurthy, Chem. Phys. Lett., 410, 348 (2005).

[83] K. Yagi, D. Watanabe, Int. J. Quant. Chem., 109, 2080 (2009).

[84] P. T. Eubank, J. Phys. Chem., 77 (22), 2670–2671 (1973).

[85] S. Niu, M. L. Tan, and T. Ichiye, J Chem Phys., 134(13), 134501 (2011).

[86] J. D. Jackson, Classical Electrodynamics, 3rd Ed., John Wiley and Sons, p. 150 (1999).

[87] P. R. Bunker and P. Jensen, Molecular Symmetry and Spectroscopy, 2nd Ed., NRC Research Press (2012).

[88] S. Mamone, M. Concistre, E. Carignani, B. Meier, A. Krachmalnicoff, O. G. Johannessen, X. Lei, Y. Li, M. Denning, M. Carravetta, K. Goh, A. J. Horsewill, R. J. Whitby and M. H. Levitt, Journal of Chemical Physics, 140, 194306 (2014).

[89] M. Concistrè, S. Mamone, M. Denning, G. Pileio, X. Lei, Y. Li, M. Carravetta, N. J. Turro, and M. H. Levitt, Philos. Trans. R. Soc. A 371, 20120102 (2013).

[90] J. R. Owers-Bradley, A. J. Horsewill, D. T. Peat, Kelvin S. K. Goh and D. G. Gadian, Phys. Chem. Chem. Phys., 15, 10413-10417 (2013).

[91] D. T. Peat, A. J. Horsewill, W. Köckenberger, A. J. Perez Linde, D. G. Gadian and J. R. Owers-Bradley, Phys. Chem. Chem. Phys., 15, 7586-7591 (2013).

[92] J. Kellogg, I. Rabi, N. Ramsey, and J. Zacharias, Physical Review 56, 728 (1939).

[93] N. F. Ramsey, Physical Review 58, 226 (1940).

[94] M. Carravetta, O. Johannessen, and M. Levitt, Phys. Rev. Lett. 92, 153003 (2004).

[95] M. Carravetta and M. H. Levitt, J. Am. Chem. Soc. 126, 6228 (2004).

[96] M. Carravetta and M. H. Levitt, J. Chem. Phys. 122, 214505 (2005).

[97] S. Cavadini, J. Dittmer, S. Antonijevic, and G. Bodenhausen, J. Am. Chem. Soc. 127, 15744 (2005).

[98] R. Sarkar, P. R. Vasos, and G. Bodenhausen, J. Am. Chem. Soc. 129, 328 (2007).

[99] M. H. Levitt, Annu. Rev. Phys. Chem. 63, 89 (2012).

[100] W. S. Warren, E. Jenista, R. T. Branca, and X. Chen, Science 323, 1711 (2009).

[101] P. R. Vasos, A. Comment, R. Sarkar, P. Ahuja, S. Jannin, J.-P. Ansermet, J. A. Konter, P. Hautle, B. van den Brandt, and G. Bodenhausen, Proc. Natl. Acad. Sci. U.S.A. 106, 18469 (2009).

[102] S. J. Devience, R. L.Walsworth, and M. S. Rosen, NMR Biomed. 26, 1204 (2013).

[103] L. Abouaf-Marguin, A.-M. Vasserot, C. Pardanaud, and X.Michaut, Chem. Phys. Lett. 480, 82 (2009).

[104] R. Tycko, R. C. Haddon, G. Dabbagh, S. H. Glarum, D. C. Douglass, and A. M. Mujsce, J. Phys. Chem. 95, 518 (1991).

[105] R. F. Curl, J. Chem. Phys. 46, 3220 (1967).

[106] P. Cacciani, J. Cosléou, and M. Khelkhal, Phys. Rev. A 85, 012521 (2012).